A STUDY OF PHASE TRANSFORMATIONS IN NI-GE SOLID SOLUTIONS

by

Zhang He

A Dissertation
Submitted to the Faculty of Graduate Studies
in Partial Fulfillment of the Requirements
for the Degree of

Doctor of Philosophy

Metallurgical Sciences Laboratory
Department of Industrial and Mechanical Engineering
University of Manitoba
Winnipeg, Manitoba

ISBN 0-315-81722-4

A STUDY OF PHASE TRANSFORMATIONS IN NI-GE SOLID SOLUTIONS

BY

ZHANG HE

A Thesis submitted to the Faculty of Graduate Studies of the University of Manitoba in partial fulfillment of the requirements for the degree of

DOCTOR OF PHILOSOPHY

ABSTRACT

This study examines the behaviour of phase transformations in Ni-rich Ni-Ge solid solutions with Ge concentration ranging from zero to 15at%. The effect of Ge addition on the lattice parameter of Ni-Ge solid solution has been investigated by the x-ray diffraction technique. The presence of an inflection point located at about 2at%Ge in the lattice parameter vs Ge concentration curve has been observed. Below this point and in dilute solid solution region there exists a linear relationship between theses two parameters. Beyond this point and in concentrated solid solution region the curve exhibits a considerably negative deviation from the plot extrapolated from the dilute solid solutions region. The presence of tiny, plate-like Ge-rich zones coherent with the matrix in concentrated Ni-Ge solid solutions has been revealed by using both TEM and x-ray diffraction techniques. The orientation relationship between the Ge-rich zones (G) and the matrix (M) is $(100)_G \| (100)_M$ and $[010]_G \| [010]_G$. Based on a thermodynamic analysis and the consideration of the influence of e/a ratio on the stability fcc crystal structure the Ge-rich zones have been suggested to be partially ordered and possess lower specific volume which is responsible for the observed negative deviation in the lattice parameter vs Ge concentration plot. The addition of Ge to nickel lattice has been also found to progressively change the dislocation configuration from a three dimensional type to a planar slip type. This change is suggested to be related to the presence of the partially ordered Ge-rich zones. In supersaturated solid solution region the microstructural and kinetic features of Ni-14.56at%Ge alloy solution treated and then isothermally aged at 550 and 600 C have been studied by TEM and x-ray diffraction techniques. Based on experimental results, the theoretical analysis of continuous phase transformation and consideration of the influence of e/a ratio on the stability of fcc crystal structure, the precipitation of phase from the Ni-14.56at%Ge alloy aged at 550 and 600 C has been concluded to undergo a phase

transformation involving a continuous growth of composition wave and the cooperation of a spinodal type phase separation and a disorder-order reaction. A reaction path describing the mechanism of the cooperation is proposed.

Acknowledgment

I would like to thank Dr.M.C. Chaturvedi for his excellent supervision, patient guidance and constant encouragement throughout the course of my research. I would also like to thank him for initiating this interesting project and giving me the opportunity to work on it. Under his guidance, I won the prize of the best student paper in metal/materials physics at the 3rd Canadian Materials Science Conference held in 1991. I wish to express my sincere gratitude to him.

I wish to thank Dr.A.K. Jena, professor of Department of Metallurgical Engineering, IIT at Kanpur, India, for his valuable discussion and suggestions.

I am also grateful to Dr.J.R. Cahoon for his generous assistance in improving my papers and this thesis.

I would like to thank Mr.'s J. Van Dorp, D. Mardis and R. Hartle, three skillful technicians in this lab for their technical assistance.

I would like to thank Mr.N. Bell in the Geological Science Department of this University for his help with using the x-ray diffractometer and doing precise lattice parameter measurements.

The funding provided by the Natural Science and Engineering Council of Canada through grants to Dr.M.C. Chaturvedi is gratefully acknowledged. I would also like to thank the University of Manitoba for providing me with the University Graduate Fellowship.

I would like to thank my wife, Yi, for her constant encouragement and endurance which enables me to complete this work.

Finally, I also wish to express my thanks to my parents for their encouragement and support. I would like to dedicate this thesis to them.

TABLE OF CONTENTS

LIST OF FIGURE CAPTIONS

LIST OF FIGURE CAPTIONS

LIST OF FIGURE CAPTIONS

LIST OF FIGURE CAPTIONS

LIST OF FIGURE CAPTIONS

LIST OF FIGURE CAPTIONS

LIST OF FIGURE CAPTIONS

LIST OF FIGURE CAPTIONS

LIST OF TABLES

LIST OF SYMBOLS

1. T_c	Critical temperature
2. c	Average composition of an alloy
3. f	Helmholtz free energy
4. f''	$\equiv \partial^2 f / \partial c^2$
5. δ_c	Infinitesimal fluctuation in composition
6. f'	$\equiv \partial f / \partial c$
7. Δf	Difference in free energy
8. $\overline{G}$	Chemical potential
9. X_i	Atomic fraction of component i
10. a	Lattice parameter
11. Ji	Flux of component i
12. N_V	Number of atoms per unit volume
13. V	Atomic velocity under a unit chemical potential gradient
14. μ_i	Chemical potential per atom of component i
15. $\tilde{D}$	Interdiffusion coefficient
16. K	Gradient energy coefficient
17. δ	Strain
18. A	Cross-section area
19. l,m,n	Direction cosines
20.C_{ij}	Elastic stiffness constants
21. W_e	Elastic energy
22. F_T	Total free energy

LIST OF SYMBOLS

23. β	Wave number
24. λ	Wavelength ($\beta=2\pi/\lambda$)
25. $A(\beta,t)$	Amplitude of the Fourier component of wave number β at moment t
26. $R(\beta)$	Amplification factor of wave number β
27. T_s^*	Coherent spinodal temperature
28. δ''	$\partial^2 s / \partial c^2$
29. h,k,l	Miller indices of a Bragg peak
30. θ_B	Bragg angle
31. η	Long range ordering parameter
32. P_A	Probability that atoms would occupy the "right" lattice site
33. F_M	Free energy of mixing
34. v(r)	Atomic pair interaction parameter
35. $V_{ij}(r)$	Energy of an (i,j) atomic pair separated by the lattice vector $\vec{x}(r)$
36. $\xi(p)$	Concentration deviation at lattice site p
37. $\vec{x}(p)$	Lattice translation vector
38. $\vec{K}(k)$	Wave vector in reciprocal space
39. $\vec{a}_j$	Primitive translation vectors in real space
40. $\vec{a}_j^*$	Primitive translation vectors in reciprocal space
41. V(k)	Reciprocal space potential
42. $\alpha(k)$	Amplification factor of wave vector k
43. d	Interatomic spacing
44. $\bar{r}$	Average atomic size
45. T	Temperature (K)
46. σ	Interfacial energy per unit area

LIST OF SYMBOLS

47. D	Volume diffusion coefficient
48. T_m	Melting point
49. K_v	Kilovolt
50. at%	Atomic percentage
51. nm	Nanometer
52. A.A.D.	Apparent atomic diameter
53. **g**	Reciprocal vector
54. L	Camera length
55. I	Intensity of a diffraction beam
56. μ_0	Linear absorption coefficient
57. ω	Weight fraction
58. ρ	Density
59. $\overline{V}_{Ge}$	Partial molar volume of germanium
60. k	Amplitude of composition wave
61. Q	Wavelength of composition fluctuation
62. f_i	Atomic scattering factor of component i

CHAPTER 1

Introduction

Ni-base superalloys possess a set of excellent properties such as high temperature strength, good ductility, good fatigue, creep and hot-corrosion resistance etc. It is these properties that enable the material to be widely used at elevated temperatures and in aggressive environments. In order to obtain the superior properties, various alloying elements are added to the fcc nickel lattice. From a microstructural point of view the role of these alloying elements can be either a solid solution hardener, a strengthening phase former, or a surface stabilizer.

In the past few years, it has been experimentally established that the addition of germanium can harden the nickel lattice considerably and that the presence of Ni_3Ge precipitates can significantly strengthen the Ni-Ge matrix. Since Ni_3Ge, like Ni_3Al, possesses a $L1_2$ crystal structure and is stable up to 1120 °C, a study of the precipitation behaviour of Ni_3Ge and the corresponding strengthening mechanism is expected to be valuable in finding applications of Ni_3Ge precipitates as a strengthening phase in the development of Ni-base superalloys. On the other hand, since the precipitation process involves two basic processes, i.e. the clustering of solute atoms and ordering, the interaction of these two processes and the precipitation reaction path play an important role in the determination of microstructure, and hence the properties of the material. Therefore,

a study of this aspect is both theoretically and practically important. Currently, research on this aspect of superalloy development is very active and different types of the interaction and reaction paths have been proposed in various alloy systems. However, a systematic study in the Ni-Ge alloy system is lacking.

The effect of Ge addition on the variation in lattice parameter of Ni-rich Ni-Ge solid solutions has been experimentally investigated by some researchers during the past few years. A definite inflection point on the lattice parameter vs composition curve has been observed by different groups of researchers. They reported that below this point the lattice parameter increases rapidly with Ge content and beyond this point, the increase in lattice parameter with Ge content occurs at a decreasing rate, and the curve exhibits a significantly negative deviation from linearity. However, until now, the reason for the occurrence of this phenomenon has not been studied. Since distinct changes in lattice parameter might be related to the change in the distribution and/or arrangement of atoms in alloys, an understanding of this phenomenon might be valuable not only in the study of the effect of Ge addition on various properties of the solid solution but also in the study of clustering and ordering interactions. This would also elucidate the reaction path during the precipitation of Ni_3Ge from supersaturated Ni-Ge solid solutions.

In this study, a systematic investigation has been conducted in the two areas mentioned above. Eight Ni-Ge alloys with Ge concentrations ranging from 0.92 to 14.5 at% were chosen. Among these alloys, the composition of six alloys was in the single phase solid solution field and the compositions of the other two alloys were in the two phase field. Transmission electron microscopy and x-ray diffraction were the main research techniques used in this study. Microhardness was chosen as a parameter to study the influence of variation in microstructural characteristics on the mechanical properties of the

material. Thermodynamic parameters and the electron theory of phase stability have been considered in explaining the observed variation in lattice parameter of the material with composition.

CHAPTER 2

Literature Review

2.1 Definition of Continuous Phase Transformation

Christian [1] has classified the phase transformations which may occur in alloy systems into two fundamental modes, namely, (a) heterogeneous transformations (b) homogeneous transformations.

The heterogeneous transformations, which include both classical heterogeneous and homogeneous nucleation processes, generally involve the spatial partition of the system into regions which are transformed and regions which are not transformed. These two kinds of regions are separated by distinct interphase interfaces. In most cases nucleation in metallic solid solution is heterogeneous. Suitable nucleation sites are the lattice defects such as vacancies, dislocations, stacking faults and inclusions etc. The existence of these non-equilibrium lattice defects increases the free energy of the system. If the formation of a precipitate nucleus results in the destruction of a defect, some amount of free energy will be released. Therefore, the activation energy barrier for nucleation is reduced and the process becomes energetically more favorable.

In a homogeneous mode, the phase transformation occurs uniformly throughout the whole system and the compositional fluctuation and/or degree of ordering are increased progressively from initially small values to large values, and the system acquires a thermodynamically more stable state. Since the entire procedure is energetically favorable, the nucleation process is no longer necessary, and, contrary to the nucleation and growth mode, the reaction is a spontaneous process and an energy barrier does not exist. The homogeneous transformation is also called a continuous transformation since the entire system transforms via a " continuous " amplification of an initially small fluctuation in composition and / or the degree of ordering within the supersaturated solid solution [2].

From an engineering standpoint, if a microstructure with very fine and uniformly distributed second phase precipitate particles within the matrix can be obtained by means of continuous phase transformations, the properties of the material are expected to be enhanced greatly. Therefore, a study of the continuous transformation is not only of theoretical interest but also of practical importance. Since the continuous type of transformation is the major concern of this study, the following sections of the literature review will be concentrated mainly on this topic.

The concept of concentration waves plays a central role in a systematic understanding of continuous phase transformations. However, this concept was originally used for describing spinodal decomposition which is actually one type of continuous transformation involving fluctuation in composition only. Therefore, before discussing disorder-order transformations using this concept, and a more complex interplay between the progressive clustering and ordering, it is necessary to briefly overview the establishment and development of this concept in the theory of spinodal decomposition.

2.2 Classical Concept of the Composition Wave --- the Theory of Spinodal Decomposition

The study of spinodal decomposition started almost 50 years ago. In the early 1940's, it was reported that quenched and aged Cu-Ni-Fe alloys with a composition inside the miscibility gap of its phase diagram exhibited sidebands (or satellite effect around some Bragg peaks in the X-ray diffraction pattern [3,4]). Further observations on the similar alloys were made by Daniel and Lipson [5,6] who suggested that the sideband effect could be due to a modulation in composition along <100> crystal directions of the matrix. In the 1950's, attention was directed at the technological potential of these alloys for various applications [7], and a theoretical explanation of the modulation in composition was first suggested by Hillert [8,9]. Starting with a regular solution mode, he derived a flux fluctuation for one dimensional diffusion in a discrete lattice. This equation differed from the usual one by the introduction of a term that allowed for the effect of the interfacial energy on the driving force between the adjacent atomic planes that are different in composition. He solved the flux equation numerically and found that inside the spinodal it yielded a periodic variation in composition as a function of distance. It was interesting that the calculated value of the wavelength of the composition modulation was of the order of 10 nm which is of the same order as reported by Daniel and Lipson from their studies on Cu-Ni-Fe alloys [5,6].

A more flexible continuum mode was subsequently developed by Cahn [10,11]. In addition to using an interfacial energy term, Cahn also introduced a coherency strain energy term. This term is important because it gives the reason for the characteristic morphology of the spinodal decomposition in elastically anisotropic materials. Cahn was also the first to use the term " spinodal decomposition " in the published literature.

On the practical applications side, spinodal decomposition has been found to offer a means of producing a very fine modulated microstructure which exhibits high age-strengthening effect and good resistance to fatigue. A number of commercial spinodal alloys have been developed and found to be suitable for use in various applications [12].

In the 1970's, studies for developing the theory of spinodal decomposition were being actively carried out. Cahn [13] and Hillard [14] thoroughly reviewed the status of spinodal decomposition in binary alloy systems. Morral and Cahn [15,16] and de Fontaine [17] extended the theory to analyze ternary alloy systems. Furthermore, the general theoretical analysis has essentially extended the notion of continuous transformation, which originally meant spinodal transformation resulting in a composition change, to include clustering and ordering of solute atoms that always take place in an alloy system where the precipitation of an ordered phase occurs [18,19]. De Fontaine [18] suggested unified treatment to incorporate both the concept of "spinodal clustering" and "spinodal ordering".

Recently, Soffa and Laughlin [20], based on their research in the Ni-Ti system, have suggested a simple approach using free energy-composition diagrams and loci of thermodynamic instability to delineate the regions of continuous phase transformation, and describe various ways of complex interplay between the clustering and ordering reaction occurring in metallic solid solutions. This graphical thermodynamic approach has been found to be applicable to other alloy systems as well.

2.2.1. Definition of Spinodal Decomposition

The phase diagram of a binary system with a miscibility gap is shown in Fig.1. Above a critical temperature T_c, complete solid-solubility is expected. Below T_c, the system

exhibits a miscibility gap and a homogeneous single solid solution within this gap decomposes into two coherently mixed phases α' and α''. These two phases possess the same or similar crystal structure but different compositions; one is solute rich and the other is solute lean.

At any temperature lower than T_c, say T_0, the variation in free energy of an undecomposed solid solution with composition c_0 can be schematically described in the top curve of Fig.1. The points of common tangency on this curve define the compositions $c_{\alpha'}$ and $c_{\alpha''}$ of the α' and α'' phases respectively. These two phases coexist in equilibrium at temperature T_0. The locus of such points is the phase boundary. In addition, there are two inflection points on the curve, at which

$$f'' = 0 \tag{1}$$

where $f'' = (\partial^2 f / \partial c^2)_{V,T}$ and f is the Helmholtz free energy. The locus of such points satisfying Eq.1 is the spinodal and is illustrated by the dashed curve in the phase diagram. Within the two inflection points $f''<0$, however, outside the inflection points $f''>0$. The thermodynamic significance of the spinodal is that it is the boundary between the two equilibrium states. The undecomposed solid solutions between the phase boundary and the spinodal are in metastable equilibrium and those within the spinodal are in unstable equilibrium. Although the final products of decomposition are the same, i.e. α' and α'', the phase decomposition in the metastable region is via the nucleation and growth mechanism. The metastable phases resist the formation of small fluctuation in composition, but do not resist the formation of larger ones. However, phase decomposition in the unstable region is by the spinodal decomposition mechanism. The phase in unstable equilibrium does not resist the formation of either small or large fluctuations in composition.

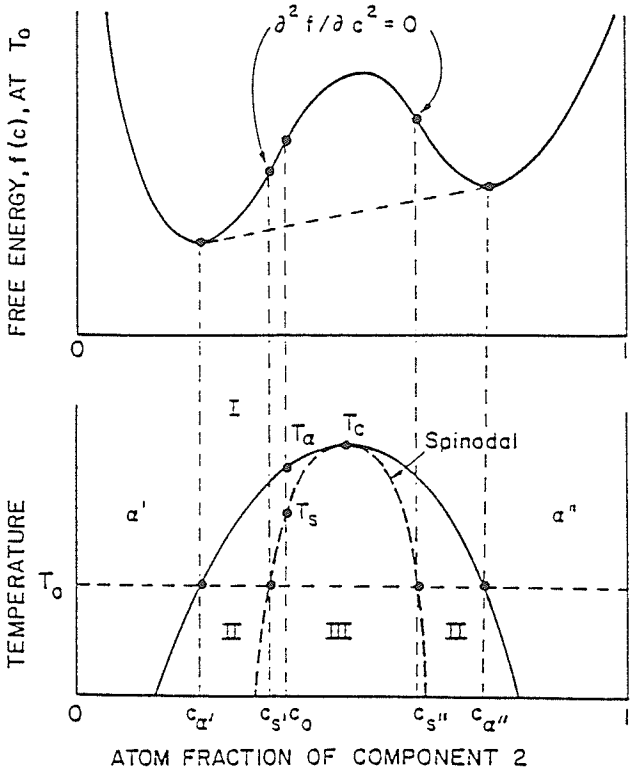

Fig.1 Helmholtz free energy curve and the resulting miscibility gap.

2.2.2. Mechanism of Spinodal Decomposition

Consider that a homogeneous binary alloy of composition c_0 decomposes into two parts: one with composition $c_0 + \delta_c$ and the other with composition $c_0 - \delta_c$, where δ_c is an infinitesimal fluctuation in composition. Before decomposition, the alloy possesses free energy $f(c_0)$. Expanding $f(c_0+\delta_c)$ and $f(c_0-\delta_c)$ in a Taylor's series about c_0 and neglecting higher order derivatives, the following expressions can be obtained,

$$f(c_0+\delta_c) = f(c_0) + f'(c_0)\,\delta_c + 1/2\, f''(c_0)\,(\delta_c)^2 + \cdots\cdots \quad (2)$$

$$f(c_0-\delta_c) = f(c_0) - f'(c_0)\,\delta_c + 1/2\, f''(c_0)\,(\delta_c)^2 + \cdots\cdots \quad (3)$$

in which primes on the f's denote derivatives with respect to composition c. The addition of Eqs.2 and 3 results in the following expression.

$$f(c_0+\delta_c) + f(c_0-\delta_c) = 2\,[f(c_0) + 1/2\, f''(c_0)\,(\delta_c)^2] \quad (4)$$

If it is assumed that the alloy decomposes into the same amount of two parts, with composition $(c_0+\delta_c)$ and $(c_0 - \delta_c)$ respectively, the difference in free energy before and after the decomposition can be expressed by

$$\Delta f = 1/2\, f''(c_0)\,(\delta_c)^2 \quad (5)$$

Since $f''(c_0)$ is smaller than zero inside the spinodal, i.e. it has a negative value, a small amount of decomposition (δ_c) will reduce the free energy of the entire system. Therefore, thermodynamically, the decomposition is a spontaneous process. In other words, there is no energy barrier for the decomposition process inside the spinodal and the

rate of decomposition is determined solely by diffusion.

After a small fluctuation in composition has already been established within the alloy, the chemical potential ($\overline{G}$) of components of the decomposed products can be determined by the well known tangent rule. The results are shown in Fig.2. It can be seen that the chemical potential within the spinodal has a lower value at a higher concentration. For example, the solute concentration at point X''_u on the free energy -composition curve is higher than the one at point X'_u, the chemical potential of solute element at point X''_u (i.e. $\overline{G}_2 (X''_u)$) is lower than the one at point X'_u (i.e. $\overline{G}_2 (X'_u)$). Similarly, $\overline{G}_1 (X''_u)$ at point X''_u is larger than $\overline{G}_1 (X'_u)$ at point X'_u. Thus, a gradient in chemical potential is established. This gradient acts as a driving force which causes components of the system to migrate from the region possessing higher chemical potential to the one possessing lower chemical potential. In the case of spinodal decomposition, the migration of solute atoms is up the concentration gradient. This solute diffusion causes the amplitude of fluctuation in composition to increase continuously and leaves a solute depleted zone around the fluctuation. This situation is schematically illustrated in region "a" of Fig.3. The outer edges of the solute depleted zone, whose composition is lower than the average composition of the material, develop a chemical potential gradient which induces solute to diffuse away from the original cluster and build up new clusters (region b). Thus, a set of small clusters periodically arranged in space are rapidly formed. Continued diffusion in an up-hill manner finally results in a structure in which the solute-rich α'' phase and the solute-depleted α' phase are periodically mixed with each other. (region c). This mechanism of phase transformation is defined as spinodal decomposition and is an up-hill diffusion controlled continuous phase transformation.

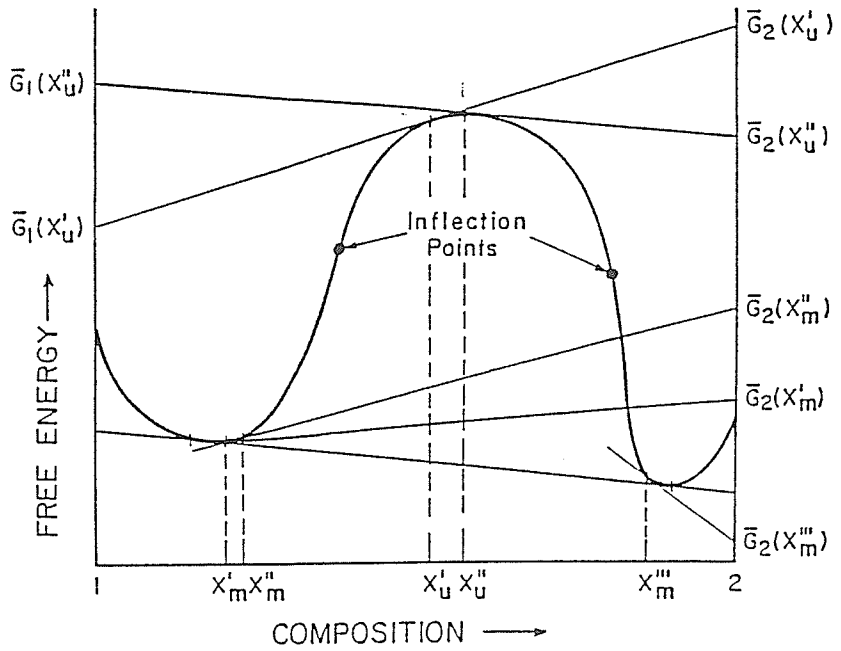

Fig.2 Change in chemical potential with composition inside and outside the inflection points.

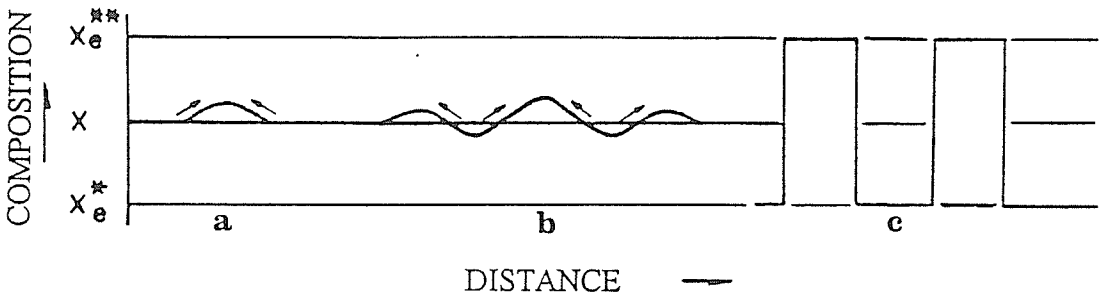

Fig.3 Growth of a small composition fluctuation within the spinodal.

2.2.3. Kinetics of Spinodal Decomposition

The kinetic theory of spinodal decomposition was developed mainly by Cahn [13]. The following section is primarily based on his work and the excellent review presented by Hilliard [14]. In this section, the classical diffusion equation will be first discussed. After that, a modified diffusion equation is proposed and the corresponding solution to this equation further developed.

A. Classical Diffusion Equation

In the discussion of the kinetics of spinodal decomposition based on the classical diffusion equation, only one dimensional diffusion is considered for simplicity. This limitation is justified because in the early stages of spinodal decomposition (which will be of primary concern) interaction between composition modulation in different crystal directions does not occur.

In a binary alloy system, the fluxes of components 1 and 2, denoted as J_1 and J_2 respectively, are proportional to the gradient in chemical potentials with respect to some fixed plane. Thus,

$$J_1 = - N_v (1-c) V_1 \left(\frac{\partial \mu_1}{\partial x} \right) \tag{6}$$

$$J_2 = - N_v c V_2 \left(\frac{\partial \mu_2}{\partial x} \right) \tag{7}$$

where N_v is the number of atoms per unit volume, c is the atomic fraction of component 2, V is the atomic velocity under a unit chemical potential gradient, μ_i (i=1, 2...) is the chemical potential of component i, and the fluxes are assumed to be along the x direction. With respect to a moving reference plane for which the total flux is zero, the flux of component 2, J, is given by

$$J = J_2 - c\,(J_1 + J_2)$$

$$= -\,N_v\, c\,(1-c)\,[V_2\,(\frac{\partial \mu_2}{\partial x}) - V_1(\frac{\partial \mu_1}{\partial x})] \qquad (8)$$

The term on the right side of Eq.(8) can be rearranged and the corresponding expression after the rearrangement can be written as follows:

$$J = -N_v\, c(1-c)\,\{[(1-c)\,V_2 + c\,V_1] \times$$

$$[\,(\frac{\partial \mu_2}{\partial x}) - (\frac{\partial \mu_1}{\partial x})] + (V_2 - V_1)[c(\frac{\partial \mu_2}{\partial x}) + (1-c)\,(\frac{\partial \mu_1}{\partial x})]\} \qquad (9)$$

Due to the following Gibbs - Duhem relationship,

$$(1-c)\,\partial\mu_1 + c\,\partial\mu_2 = 0 \qquad (10)$$

the last term in Eq.9 is zero and Eq.9 reduces to

$$J = -N_v\, c\,(1-c)\,[(1-c)\,V_2 + c\,V_1]\,[(\frac{\partial \mu_2}{\partial x}) - (\frac{\partial \mu_1}{\partial x})] \qquad (11)$$

If M is defined by the following expression,

$$M=c\,(1-c)\,[(1-c)\,V_2 + c\,V_1] \tag{12}$$

Eq.11 can be simplified to the following:

$$J = -N_v\, M\, [(\frac{\partial \mu_2}{\partial x}) - (\frac{\partial \mu_1}{\partial x})] \tag{13}$$

Since μ_1 and μ_2 are the chemical potentials per atom, while f is the free energy per unit volume, then

$$N_v\, c\, \mu_2 + N_v\, (1-c)\, \mu_1 = f \tag{14}$$

The variation in free energy, f, with composition c can be obtained by differentiating Eq.14 with respect to composition c resulting in the following expression:

$$N_v\, (\mu_2 - \mu_1) = df / dc \tag{15}$$

By differentiating Eq.15 with respect to x and substituting in Eq.13 the following expression for J is obtained:

$$J = - M\, (\, d / dx)\, (df / dc)$$

or

$$J=-M\, (d^2f/dc^2)\, (dc/dx). \tag{16}$$

Assuming that M and d^2f/dc^2, (i.e.f") are independent of diffusion distance x, and differentiating Eq.16 with respect to x, the following expression can be obtained

$$\partial J/\partial x = -M\, f''\, (\partial^2 c/\partial x^2). \quad (17)$$

Since

$$\partial c/\partial t = -\, 1/N_v\, (\partial J/\partial x) \quad (18)$$

where the purpose of introducing N_v is to keep the units on both sides of the equation consistent. By combining Eq.17 and 18, the following expression can be derived:

$$\partial c/\partial t = (M/N_v)\, f''\, (\partial^2 c/\partial x^2). \quad (19)$$

By comparing Eq.19 with the following statement of Fick's second Law of diffusion

$$\partial c/\partial t = \tilde{D}\, (\partial^2 c/\partial x^2) \quad (20)$$

where $\tilde{D}$ is the interdiffusion coefficient, the following relationship between $\tilde{D}$ and f'' can be obtained by

$$\tilde{D} = f''\, M/N_v \quad (21)$$

In Eq.21, the sign of $\tilde{D}$, (whether positive or negative) is governed only by the nature of f'' since M and N_v possess positive value. Within the spinodal, $f'' < 0$ and therefore $\tilde{D}$ is negative. The physical significance of $\tilde{D} < 0$ is that the diffusion occurs in an up-hill manner, i.e. the solute atoms migrate from a lower concentration region to a higher concentration region.

B. Modification of the Classical Diffusion Equation

The variation in composition between the maximum and minimum of the composition fluctuations induced by spinodal decomposition is comparable to a diffuse interface between the two phases. An excess of free energy associated with such an interface can be expected. Thermodynamically, this "interfacial energy" is positive and will decrease the driving force which is available for the diffusion of atoms participating in the phase transformation. It can be assumed that the shorter the composition modulation wavelength, the greater the composition gradient and, hence, the higher the "interfacial" energy. Therefore, in this case, the amount of the decrease in driving force can no longer be neglected. However, in deriving the classical diffusion equation, the driving force was assumed to be composition dependent. Therefore, in the case of spinodal decomposition, a term related to the interfacial energy should be introduced to modify the classical diffusion equation.

a. Consideration of Interfacial Energy

In order to determine the interfacial energy term quantitatively, Cahn [10] utilized a treatment which assumed that the free energy of a nonhomogeneous system could be expressed by the following multivariable Taylor's expansion:

$$f(y,z,\cdots\cdots) = \left(\partial f/\partial y\right).y + 1/2\left(\partial^2 f/\partial y^2\right) y + \cdots\cdots\cdots\cdots$$
$$+ \left(\partial f/\partial z\right) z + 1/2\left(\partial^2 f/\partial z\right) z + \cdots\cdots\cdots$$
$$+\left(\partial^2 f/\partial y \partial z\right) y\, z + \cdots\cdots\cdots\cdots \qquad (22)$$

Here the variables, y, z .....are the spatial composition derivatives (dc /dx, d^2c / dx^2, etc.). The free energy of a small volume element containing a one-dimensional composition fluctuation can be expressed (neglecting third and high-order terms) as follows:

$$f = f(c) + L(dc/dx) + K_1(d^2c/dx^2) + K_2)(dc/dx)^2, \quad (23)$$

where

$$L = \partial f / \partial (dc/dx)$$

$$K_1 = \partial f / \partial (d^2c/dx^2)$$

$$K_2 = (1/2)\,\partial^2 f / \partial (\partial c/dx)^2$$

(evaluated at zero gradients) and f(c) is the free energy that a volume element of composition c would have if it were homogeneous.

The total free energy of a system with a cross-section A containing a one dimensional fluctuation in composition can then be obtained by integrating Eq.23. By proper treatment, the corresponding expression can be written as follows:

$$F_T = A \int [f(c) + K(dc/dx)^2]\, dx, \quad (24)$$

where $K = K_2 - (dK_1 / dc)$ and is termed the "gradient-energy coefficient".

To determine the expression for the potential corresponding to the system which

possesses a free energy expressed by Eq.24, the following requirements should be satisfied. First, the obtained expression of the potential must reduce to the classical one, df / dc, when the gradient-energy coefficient K is set equal to zero. Second, at equilibrium, the potential should be constant throughout the system. Cahn has solved the problem and defined a term α which possesses the property of the potential. The corresponding expression for α is given by,

$$\alpha = df / dc - 2K (d^2c / dx^2) = \text{constant} \tag{25}$$

Substituting α for (df / dc) in Eq.16, the modified flux equation can be expressed as follows:

$$J = -M (d /dx [(df /dc) - 2K(d^2c / dx^2)] \tag{26}$$

Performing the differentiation with respect to x and assuming K to be a constant, the result can be expressed by

$$J = - M [f''(dc / dx) - 2K (d^3c / dx^3)] \tag{27}$$

Similarly, if the atomic sizes of components making up a binary solid solution are different, the formation of a composition fluctuation will introduce a coherency strain. Since the coherency strain energy is positive, it will decrease the driving force for diffusion as well. Therefore, the classical diffusion equation should also be modified based upon the above consideration.

b. Consideration of Coherency Strain Energy

The elastic strain energy of a cubic crystal can be estimated by calculating the work required to deform a slice of the material so that it can be added coherently to an existing slab of unit cross-sectional area (Fig.4). Assuming that the lattice spacing in the plane of the slab is a_0 and that of the undeformed slice is "a", if the slice is to be coherent after being joined to the slab it must be subjected to a strain of δ, which is given by the following:

$$\delta = (a - a_0) / a_0 \tag{28}$$

The total elastic energy of a slab of cross-section area A is then given by

$$W_E = A \int Y \delta^2 \, dx \tag{29}$$

where,

$$Y = (1/2)\,(c_{11} + 2c_{12}) \times \{3 - (c_{11} + 2c_{12}) / [c_{11} + 2\,(2\,c_{44} - c_{11} + c_{12})\,(l^2m^2 + m^2n^2 + l^2n^2)]\} \tag{30}$$

In this expression the c's are the elastic stiffness constants and l, m, n are the direction cosine of the direction of the composition modulation. For comparison purposes, the elastic stiffness constants of some metals with a cubic crystal structure are given in Table 1 [21].

If a_0 is the lattice parameter of the unstrained region with an average composition c_0, a Taylor's expansion of the lattice parameter, a, about c_0 yields

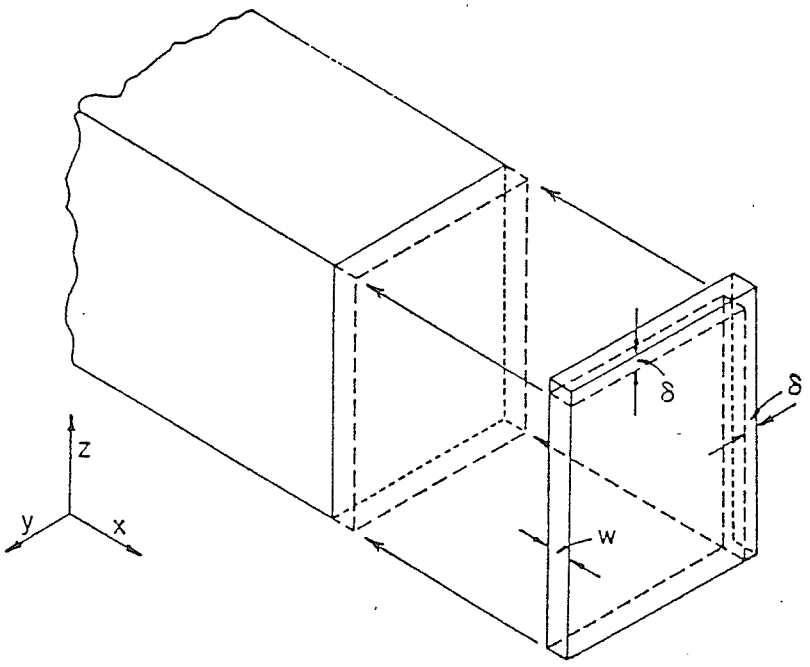

Fig.4 A slice of material that has to be subjected to strain in Z and Y directions if it is to be coherent with a section in ZY plane.

Table 1. Elastic stiffness constants and anisotropic factors for fcc metals [21]

Element	Elastic stiffness constant			Anisotropy factor (A) $A=2C_{44}/(C_{11}-C_{12})$
	C_{11}	C_{12}	C_{44}	
Al	10.70	6.08	2.83	1.23
Cu	16.84	12.14	7.55	3.21
Ag	12.40	9.37	4.61	3.04
Au	19.23	16.31	4.20	2.87
Ni	24.36	14.94	11.96	2.54

$$a = a_0 [1+\eta(c-c_0 \quad) +.....] \tag{31}$$

If,

$$\eta = (1/a_0) (da / dc) = d (\ln a) / dc \tag{32}$$

then Eq.31 becomes

$$a = a_0 [1 + \eta(c - c_0) +\cdots\cdots\cdots] \tag{33}$$

Neglecting higher order terms in Eq.33, the following relationship for δ can be obtained

$$\delta = (a - a_0) / a_0 = \eta (c- c_0) \tag{34}$$

By substituting this in Eq.29, the following expression for the total elastic energy of the slab of cross-section area A can be obtained,

$$W_E = A \int \eta^2 Y (c - c_0)^2 dx \tag{35}$$

This indicates that the strain energy depends only on the amplitude of the composition modulation and is independent of the wavelength and W_E is proportional to Y.

From Table 1 it is seen that for most common metals with cubic crystal structure

$$2 c_{44} - c_{11} + c_{12} > 0 \tag{36}$$

Therefore, from Eqs. 29 and 30 the value of Y and, hence, the elastic energy, will be a minimum for those directions for which the value of ($l^2m^2 + l^2n^2 + m^2n^2$) is a minimum. When the direction of composition modulation is parallel to <100>, $Y_{<100>}$ becomes minimum,

$$Y_{<100>} = c_{11} + c_{12} - 2\,(c^2_{12} / c_{11}) \tag{37}$$

As will be shown later, the growth rate of the composition modulation will be maximum in a direction that minimizes Y. These directions therefore determine the morphology of the decomposed cubic solid solutions. The total free energy of the solid solution, now includes both interfacial energy and elastic strain energy which are induced by composition modulation. This total free energy of the solid solution with compoition modulation in it is given by

$$F_T = A \int [\, f(c)+\eta^2 Y\,(c-c_0)^2+K\,(dc / dx)^2\,]\, dx, \tag{38}$$

and the diffusion equation is given by

$$\partial c / \partial t = (M / N_v)[\, (f''+2\eta^2 Y)\,(d^2c / dx^2) - 2K(d^4c / dx^4)] \tag{39}$$

C. Solution of the Modified Diffusion Equation

If terms M and N in Eq.39 are assumed to be independent of c, the equation can be solved by a Fourier transformation method. Let $A(\beta)$ be the amplitude of a Fourier component of wavenumber β ($\beta = 2\pi / \lambda$, where λ is wavelength of the composition modulation) then the spatial composition variation can be expressed by the Fourier

integral

$$c\text{-}c_0 = \int A(\beta) \exp(i\beta x)\, d\beta \tag{40}$$

According to the inverse relationship the coefficient A (β) in Eq.40 can be expressed as follows:

$$A(\beta) = (1 / 2\pi) \int (c\text{-}c_0) \exp(-i\beta x)\, dx \tag{41}$$

By differentiating Eq.40 with respect to time t, the following equation is obtained

$$\partial c / \partial t = \int [dA(\beta)/dt] \exp(i\beta x) d\beta \tag{42}$$

By noting that

$$d^n c/dx^n = \int (i\beta)^n A(\beta) \exp(i\beta x)\, d\beta \tag{43}$$

Eq.39 can be rewritten as follows:

$$\partial c / \partial t = (M/N_V) [(f''+2\eta Y) \int (i\beta)^2 A(\beta) \exp(i\beta x)\, d\beta - 2K \int (i\beta)^4 A(\beta) \exp(i\beta x)\, d\beta] \tag{44}$$

On equating corresponding coefficients of Eq.42 and 44, the following equation is obtained

$$d\,A(\beta)/dt = -(M/N_v)[f'' + 2\eta^2 Y + 2K\beta^2]\,\beta^2\,A(\beta) \qquad (45)$$

Eq.45 is an ordinary differential equation. The solution of this equation is then given by,

$$A(\beta,t) = A(\beta,0)\exp[R(\beta)t] \qquad (46)$$

in which $A(\beta,0)$ is the initial amplitude of the Fourier component of wavenumber β and $R(\beta)$ is called an amplification factor, which is defined by,

$$R(\beta) = -(M/N_v)[f'' + 2\eta^2 Y + 2K\beta^2]\,\beta^2 \qquad (47)$$

In Eq.(47), the term $2\eta^2 Y$ is due to the elastic strains and $2K\beta^2$ term involves the gradient energy which becomes important when β increases, i.e. when the wavelength λ decreases. If decomposition can be suppressed completely during quenching from the supersaturated state into the spinodal, the initial amplitude of the composition modulation wave $A(\beta,0)$ will be the amplitude due to thermal fluctuation that is in equilibrium at the quenching temperature T_q. This is given by [22],

$$\langle A^2(\beta)\rangle = [\,K T_q / V_T (f'' + 2\eta^2 Y + 2K\beta^2)], \qquad (48)$$

where V_T is the volume of the specimen. Usually, during quenching some degree of decomposition may occur and the amplitude $A(\beta,0)$ will be the value at the end of quenching.

2.2.4. Characteristics of Early Stages of Spinodal Decomposition

In deriving and solving the linear diffusion equation it was assumed that the parameters K, η, Y, M, and f'' are independent of composition. Actually, these assumptions are only valid when the amplitude of composition fluctuation is small. Therefore, the analytical solution of the diffusion equation and its corresponding physical meaning are only valid during the early stages of decomposition.

It is seen from Eq.(47) that at any particular temperature and composition within the spinodal there exists a critical wavenumber β_c (and accordingly a wavelength, $\lambda_c = 2\pi / \beta_c$) which satisfies the following relationship:

$$f'' + 2\eta^2 Y + 2K\beta_c^2 = 0 \qquad (49)$$

and for which $R(\beta) = 0$. Other Fourier components for which $\beta < \beta_c$ will grow but for those for which $\beta > \beta_c$ will decay. The variation of amplification factor $R(\beta)$ with wavenumber β is shown by the solid curve in Fig.5. The physical meaning of this curve is:

(1) On the small wavenumber side, $R(\beta)$ increases with an increase in β because of the decrease in diffusion distance. In this region the classical diffusion equation (dashed curve in Fig.5) is a satisfactory approximation.

(2) On the large wavenumber side, $R(\beta)$ decreases rapidly with an increase in β. This is because when β is large the composition gradient becomes the dominant factor

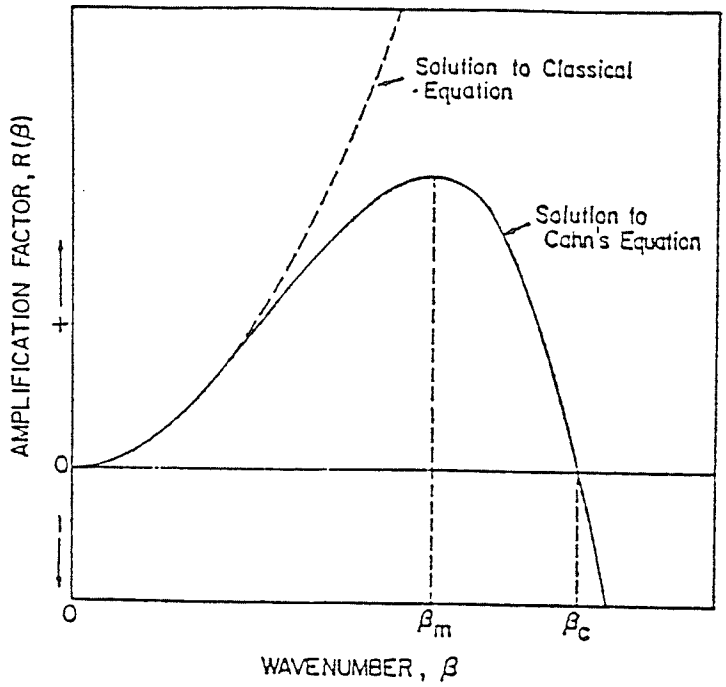

Fig.5 Dependence of the amplification factor on wavenumber β.

in influencing the free energy of the system and the driving force for the transformation decreases rapidly. Eventually, $R(\beta)$ becomes negative at a critical value of $\beta = \beta_c$. and it reaches a maximum value at $\beta = \beta_m$ when β_m is equal to $1/\sqrt{2}(\beta_c)$.

Since the wavenumber β and the wavelength λ have the relationship $\beta=2\pi/\lambda$, the variation in the amplification factor R can be also expressed as a function of wavelength λ and can be shown as in Fig.6

The locus of $\beta_c = 0$ is defined as the coherent spinodal distinguished from the chemical spinodal which is defined by Eq.1. From Eq.(49) the locus of a coherent spinodal is therefore given by

$$f'' + 2\eta^2 Y = 0 \tag{50}$$

Since Y is a function of direction in anisotropic crystalline materials, it follows that the coherent spinodal temperature will also vary with the direction of the composition fluctuation. This temperature will be a maximum for those directions that minimize $2\eta^2$ Y. As mentioned earlier, those directions are usually along <100> in cubic crystalline materials.

According to Cahn's calculation, the maximum value of amplification factor $R(\beta_m)$ corresponding to the maximum value of β_m can be expressed by,

$$R(\beta_m)=(2KM/N_V)\beta^4{}_m, \tag{51}$$

β_m is temperature dependent and can be expressed by,

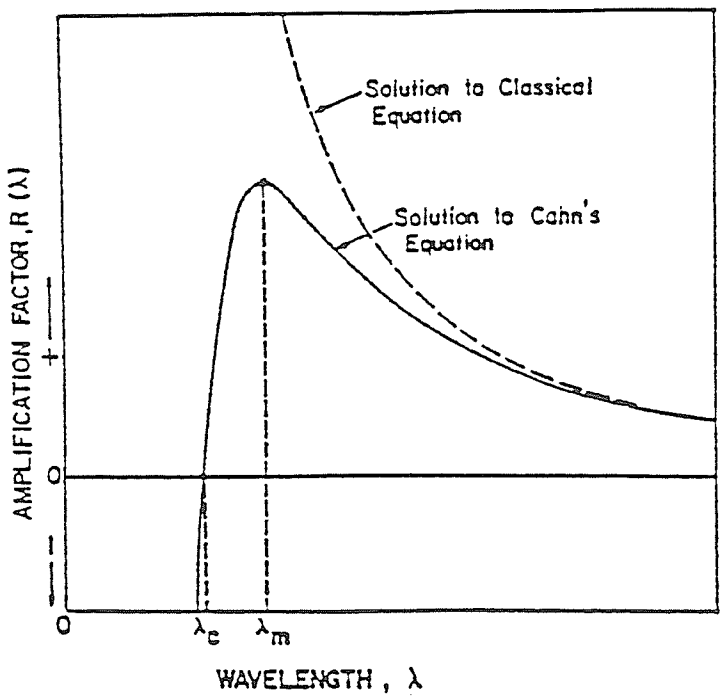

Fig.6. Variation in amplification factor with wavelength λ.

$$\beta_m^2 \approx (T - T_s^*) s'' / 4 K \qquad (52)$$

where, T is the isothermal ageing temperature, and T_s^* is the coherent spinodal temperature of the system, $T \leq T_s^*$. $S'' = (\partial^2 s / \partial c^2)$ where s is the entropy per unit volume and $S'' \leq 0$. By combining Eq.51 and 52, it is seen that when T is equal to T_s^*, $R(\beta_m)$ reduces to zero. That is to say no decomposition will occur at the coherent spinodal temperature, i.e. T_s^*. As T decreases, the difference between T and T_s^* increases. β_m increases and accordingly λ_m decreases. The amplification factor $R(\beta_m)$ also increases. However, at lower ageing temperature, due to a decrease in atomic mobility, i.e. a lower value of m in Eq.51, the increase in $R(\beta_m)$ will eventually be offset. Therefore, the $R(\beta_m)$ can reach its highest value at intermediate ageing temperatures.

The physical meaning of the solution of the linear diffusion equation, which is only valid at the early stages of the decomposition, can be summarized as follows:

1. There will be one wavelength, λ_m, of the initial Fourier spectrum that will have a maximum growth rate and any Fourier component with a wavelength less than the critical value λ_c (where $\lambda_c = \lambda_m / \sqrt{2}$) will decay.

2. λ_m (and therefore λ_c) decreases with: (a) decreasing temperature, (b) decreasing values of K, and (c) a shift in the average composition C_0 towards the center of the spinodal.

3. In cubic materials, preferential growth will occur along those directions that minimize the coherency strain energy (usually <100>).

4. The rate of decomposition is zero at the temperature of coherent spinodal and passes through a maximum with decreasing temperature.

2.3 Experimental Investigation of The Early Stage of Spinodal Decomposition

The development of the theory of spinodal decomposition provides a fundamental basis for an understanding of the evolution of quasi-periodic composition modulations or concentration waves during the decomposition of supersaturated solid solution. However, early in the 1940's, the notion of a "wave-like" clustering or periodic redistribution of solute atoms during ageing had already been suggested by Daniel and Lipson [5,6]. The concept was used to explain the appearance of a so called "side-bands" or "satellites" around main diffraction peaks in x-ray diffraction patterns during the precipitation process in Cu-Ni-Fe alloys. The intensity of the sidebands in x-ray diffraction patterns is due to the contribution by the fluctuation in lattice spacing as well as in atomic scattering factor which are induced by the composition modulation. Due to the reciprocal relationship between the real space (lattice space) and the reciprocal space (diffraction space), the intensity of the sidebands may be considered to arise due to the contribution by these crystal planes with interplanar spacing equal to the wavelength of the composition modulation. The wavelength of the composition modulation (λ) can be estimated from the x-ray diffraction data using the following well known Daniel-Lipson formula [5,6]

$$\lambda = h\, a_0 \tan \theta_B / (\Delta\theta)\,(h^2 + k^2 + l^2) \qquad (53)$$

where h, k, l are the Miller indices of a Bragg peak, θ_B is the Bragg angle, a_0 is the average lattice parameter of the material, $\Delta\theta$ is the angular separation of the side-bands from the Bragg peak and λ is the wavelength of the composition modulation. Usually, all measurements are made on (200) profile since this reflection gives the best combination of side band resolution (large $\Delta\theta$) and intensity.

Similarly, the TEM electron diffraction patterns observed from a spinodal alloy also show matrix diffraction spots flanked by satellites. The satellites usually align themselves along the <100> directions, if the crystal structure of the matrix is cubic and exhibits elastic anisotropic behaviour.

The morphology of the products of spinodal decomposition depends upon many factors. Among these factors, elastic anisotropy is the most important one. In an elastically anisotropic crystal the composition modulations form preferentially along elastically soft directions in order to reduce the elastic strain energy, and finally minimize the total free energy of the system. Since cubic crystals are elastically soft along <100> directions, the microstructure may be the result of superposition of three sets of composition modulations whose wave fronts are parallel to the three sets of {100} planes. In the early stages of spinodal decomposition periodic striations due to strain field contrast are usually observed in transmission electron microscope images. These striations usually arrange themselves along <100> directions. It should be noted that although spinodal decomposition gives rise to a modulated microstructure in many alloy systems, such modulated microstructure may sometimes be also formed by nucleation and growth type of transformation reactions [23]. Therefore, the occurrence

of modulated microstructure is only a necessary, but not a sufficient, condition for the transformation classified as a spinodal decomposition.

Other morphological feature that characterizes spinodal alloys is the absence of preferential precipitation at lattice imperfections such as grain boundaries and dislocations etc. This is because the activation energy for spinodal decomposition is less then kT [24], where k is the Boltzmann's constant, T is the isothermal ageing temperature.

Another important criterion for a transformation to be classified as spinodal decomposition arises by the kinetics of the reaction. Cahn's theory of spinodal decomposition predicts that there is a composition modulation wave, with a wave length λ_m, which has the maximum amplification factor $R(\lambda)$ and will be in a dominant position to grow as compared to the other waves. As ageing progress and the amplitude of wave increases, the preferential growth of this wave keeps the wavelength constant over short ageing periods. Such a characteristic constant wavelength has been detected in several spinodal alloys [25,26,27]. However, in some other alloy systems which were reported to decompose via spinodal mechanism, such short periods of constancy of λ could not be detected. It is probably because the period during which the value of λ remains constant is so short that it has already passed during quenching from the solution treatment temperature.

By far, the most common and successful techniques for the study of spinodal decomposition are x-ray diffraction and transmission electron microscopy. Besides these, neutron diffraction, field ion microscopy (FIM), atom probe field ion microscopy (APFIM), high resolution electron microscopy (HRTEM) and various physical property measurement techniques have been also used for comparison

purposes with the results obtained by TEM and x-ray diffraction studies.

The occurrence of spinodal decomposition has been reported in many alloy systems. The crystal structure of the spinodal alloys is not only fcc, such as Au-Ni, Ni-Ti, Co-Ti, Co-Fe-Ti, Ni-Al, Cu-Ni-Cr, Cu-Ti, Cu-Ni-Sn, Ni-Mo,etc. but is also bcc such as Nb-Zr, Fe-Mo, Fe-Cr, Fe-Cr-Mo etc. Among these alloy systems, Cu-Ni-Cr system has been studied most extensively by many researchers using various kinds of techniques. X-ray and TEM techniques were applied by Kreye and Pech [28], Wu and Thomas [29] and Chou et al [30]. The entire decomposition process of the material was found to involve only a fluctuation in composition, i.e. phase separation. Wu, Sinclair and Thomas [31] successfully used the lattice imaging technique and optical microanalysis to characterize the modulated structure or "wave-like" modulation in composition that occurred during the early stages of spinodal decomposition. The Au-Ni alloy system is another example where the entire decomposition process involves only the composition fluctuation process [32]. However, in many other alloy systems, the precipitation process may combine both the phase separation, i.e. continuous clustering, and ordering arrangement of solute and solvent atoms. Therefore, the actual reaction path of the continuous phase transformation becomes more complex, when the second phase is an ordered phase and involves an order-disorder phase transformation.

2.4 Some Basic Concepts Relating to First-Order Order-Disorder Transformation [20]

Fig.7 is a typical phase diagram configuration associated with a first order order-

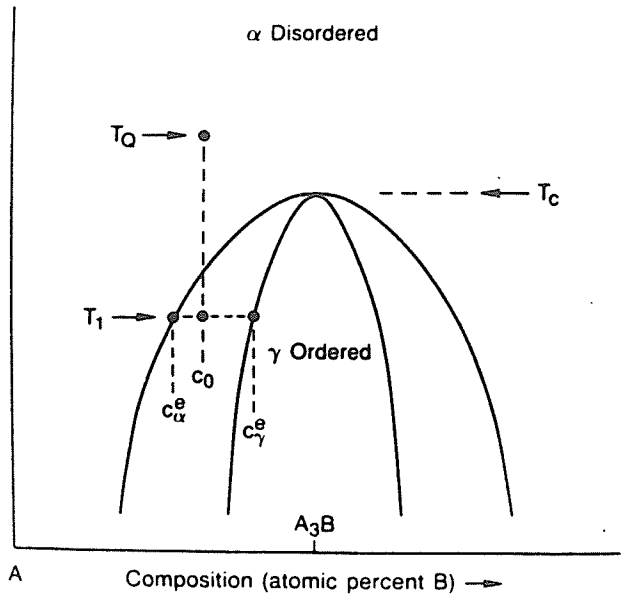

Fig.7 Phase diagram of a binary alloy system associated with first order-disorder transformation.

disorder phase transformation. When the transformation temperature (T) is lower than the critical temperature T_c, the alloy with stoichiometric composition A_3B possesses an ordered structure. However, when the temperature is higher than T_c, the A and B type atoms are randomly distributed in the lattice and the alloy is in a disordered state.

The degree of order in the crystal can be defined by a long-range ordering (LRO) parameter η, which is given by

$$\eta = (P_A - X_A) / (1 - X_A) \tag{54}$$

where X_A is the molar concentration of component A in the alloy and P_A is the probability that the A atoms would occupy the "right" lattice site. When the alloy is fully ordered, all A atoms occupy the "right" lattice site, $P_A=1$ and $\eta=1$. When the alloy is partially ordered or short range ordered (SRO), $X_A < P_A < 1$ and $0 < \eta < 1$. When the alloy is in a disordered state, $P_A=X_A$ and hence, $\eta=0$.

Fig.8 is a schematic diagram which shows the characteristic variation in η with temperature for an A_3B type of an ordered phase. At the temperature $T=T_c$, there is a thermodynamic equilibrium between the ordered state A ($\eta \neq 0$) and disordered state A'($\eta \neq 0$). This equilibrium can be depicted by using the Landau plot of the free energy (G) as a function of long range ordering parameter η in Fig.9a (curve 1). When the temperature $T_c < T < T^+_i$ (curve 2 in Fig.9a), thermodynamically, the disordered state is more stable than the ordered state, i.e. ($G(\eta=0) < G(\eta=\eta')$). However, an energy barrier ($\Delta G = G (\eta_{max}) - G (\eta')$) exists for the order $\rightarrow$ disorder transformation. Therefore, the alloy is in a metastable state and the disordering must occur by a heterogeneous transformation involving nucleation and growth of the disordered phase within the metastable ordered phase. In Fig.8, the dotted curve from A to B indicates

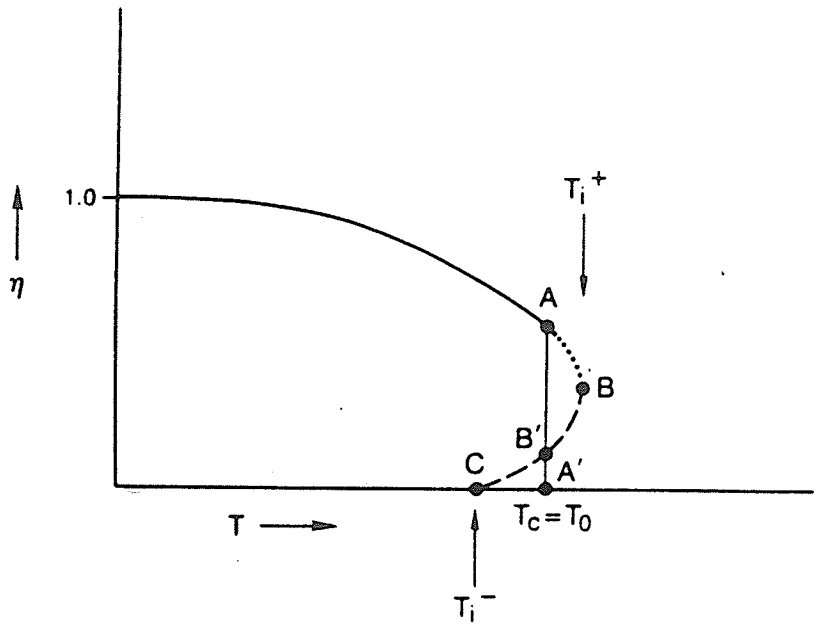

Fig.8 Variation in the long range ordering (LRO) parameter (η) with temperature for an order-disorder transformation.

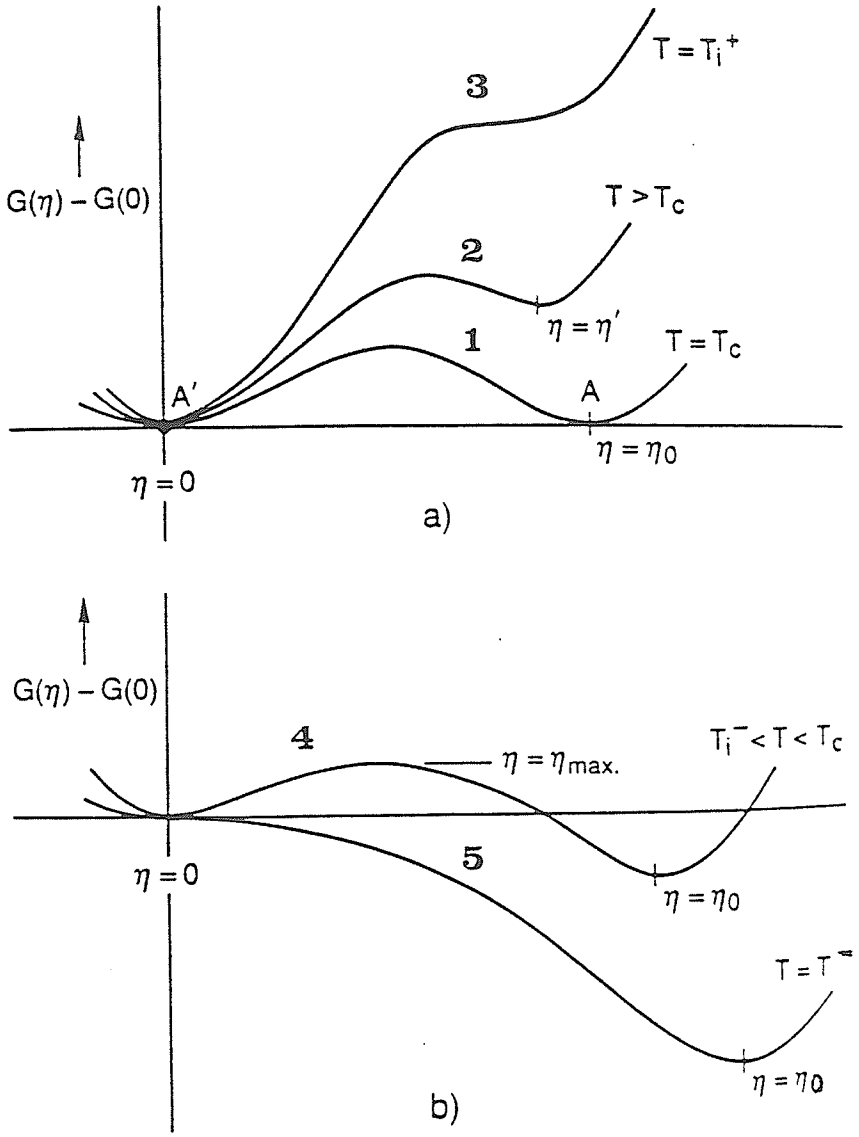

Fig.9. Free energy curves showing the variation in G(η)-G(0) with temperature and ordering parameter. G(η) is the free energy of the ordered phase in the ordered state (η) and G(0) is the free energy of the disordered state.

this metastable regime within which $0 < \eta' < \eta_0$. At or above the temperature T^+_i, the energy barrier reduces to zero (Fig.9a, curve 3), and the state of the superheated ordered phase is unstable with respect to disordering. This causes a spontaneous transition to occur and an originally ordered phase transforms into a disordered phase homogeneously (or continuously).

Similarly, on cooling, the disordered state is unstable with respect to the ordered state (Fig.9b). In the transition temperature regime $T^-_i < T < T_c$, an energy barrier exists (Fig.9b, curve 4), and the undercooled disordered phase ($\eta = 0$) can only transform into an ordered phase via nucleation and growth mechanism. This regime is predicted by a dashed B'C curve in Fig.8. At the temperature T^-_i or lower, the barrier vanishes and the free energy monotonically decreases from G (η=0) to G ($\eta=\eta'_0$). The disordered state is unstable with respect to ordered one and will homogeneously or continuously transform involving the spontaneous amplification of the specific ordering throughout the whole system without a nucleation step.

This discussion can be generalized and extended to off-stoichiometric compositions [33]. Fig.10 shows an order-disorder phase diagram superposed by the ordering (T^-_i) and disordering (T^+_i) instability loci as well as the locus T_0 which delineate the temperature at which the ordered and disordered phases are at an equilibrium state.

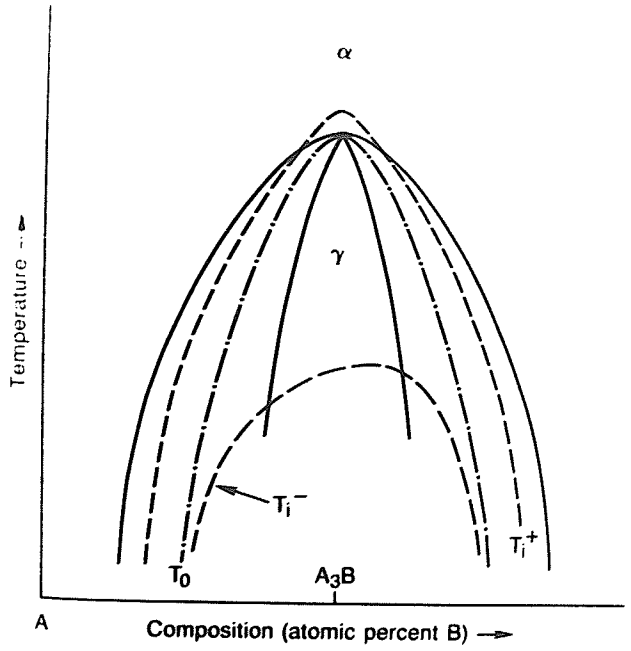

Fig. 4. Schematic order/disorder phase diagram with super-

Fig.10 A binary phase diagram in which an order-disorder transformation occurs.

2.5 Development of the Concept of Composition Wave in Interpreting the Interplay of Clustering and Ordering reactions

It was Hillert [9] and Cahn [10] who first suggested using the concept of concentration waves to describe the phase separation process in metallic solid solutions during spinodal decomposition. This concept has been proved to play an important role in understanding the process of continuous fluctuation in composition that occurs in spinodal alloys. The concept was further developed and generalized by de Fountaine, Cook and Hilliard [17, 34,35] using a discrete lattice approach. This approach has proved to be not only suitable for describing spinodal decomposition which is treated as a long wavelength limit in this approach but also suitable for describing both first and second order continuous ordering transitions which are treated as a short wavelength limits. Moreover, it also provides a basis for understanding more complex reaction process involving both clustering and ordering processes which usually occur along with the evolution of an ordered phase from a supersaturated solution, such as the continuous phase transformation of γ' in most Ni-base superalloys. Therefore, it seems appropriate to provide a brief overview of "the discrete lattice" approach when it is used to characterize fluctuation of diffusional instability in solids. The literature mainly follows the approach suggested by de Fontaine [18], since it provides a rather straightforward method for understanding the complex interplay of clustering and ordering process that often occurred in age-hardening alloys.

In de Fontaine's approach, the Helmhotz free energy of a binary A-B alloy with an average atomic composition c_{av} can be expressed by

$$F = F_A + F_B + F_M \tag{55}$$

where F_A and F_B are the free energies of pure A and B crystals including vibration entropy and F_M is the configuration free energy of mixing which can be expressed by the following:

$$F_M = Nv_0q_0 + \frac{1}{2}\sum_{p\neq p'} v(p'-p)\xi(p)\xi(p') + \\ + \tau\sum_{p}\{c(p)\ln c(p) + [1-c(p)]\ln[1-c(p)]\} \tag{56}$$

In Eq.56, N is the number of unit cells which form the crystal lattice of the alloy and $\xi(p)$ is the concentration deviation from the average composition c_{av} at lattice site p and is expressed by,

$$\xi(p) = c(p) - c_{av} \tag{57}$$

and v(r) is the atomic pair interaction parameter which is given by,

$$v(r) = \frac{1}{2}[v_{AA}(r) + v_{BB}(r) - 2v_{AB}(r)] \tag{58}$$

where $v_{ij}(r)$ is the energy of an (i,j) atomic pair separated by the lattice vector $\vec{X}(r)$ linking lattice sites p to p'. The following notation has also been introduced for brevity:

$$q_0 = c_Ac_B = c_{av}(1 - c_{av}) \tag{59}$$

$$v_0 = -\sum_{r} v(r) \tag{60}$$

$$\tau = kT \tag{61}$$

where k is Boltzmann's constant and T the absolute temperature.

For the case of a continuous phase transformation, the free energy has no singularity at finite temperatures and can thus be expanded in a Taylor's series about the homogeneous state $c(p) = c_{av}$. It has been established that an expansion to the fourth order does not change the essential features of the model [18] and the result of the expansion can be given by,

$$F_M \approx N f_0 + \frac{1}{2} \sum_{p,p'} f_0'' (p'-p)\, \xi(p)\xi(p') + \frac{1}{3!} f_0''' \sum_{p} \xi^3(p) + \frac{1}{4!} f_0'''' \sum_{p} \xi^4(p) \tag{62}$$

where

$$f_0 = v_0\, c_A c_B + \tau\, (c_A \ln c_A + c_B \ln c_B) \tag{63}$$

$$f_0''\, (r \neq 0) = 2v(r) \tag{64}$$

$$f_0''(0) = \tau / q_0 \tag{65}$$

$$f_0''' = -\tau\, (c_A^2 - c_B^2) / q_0^2 \tag{66}$$

$$f_0'''' = 2\tau\, (c_A^3 + c_B^3) / q_0^3 \tag{67}$$

It can be seen that the zeroth order term in Eq.62, i.e. Nf_0 is just the free energy expression of the regular solution model, and that the second order term in Eq.62 is the only one which depends on local concentration.

Due to the occurrence of clustering and ordering, extra diffraction effects would appear. For example, due to the occurrence of spinodal decomposition, sidebands would appear around the main diffraction peak. The position of the sub-peak has a reciprocal relationship with the wavelength of the composition wave. And the intensity of the sidebands would be proportional to the amplitude of the wave. Similarly, when ordering occurs, superlattice peaks would appear at some fixed reciprocal lattice sites. Therefore, these diffuse scattering effects can be more conveniently understood when the wavelength and the amplitude of the concentration wave are expressed in terms of a reciprocal space rather than real space. On this Basis, the Fourier transform technique is introduced. Accordingly, the Fourier transforms of the concentration deviation from the average composition, $\xi(p)$, is then expressed by,

$$x(k) = 1/N \sum_{p} \xi(p) \exp[-i \vec{k}(k) \vec{x}(p)] \tag{68}$$

The lattice translation vector $\vec{x}(p)$ in the real space and the wave factor $\vec{k}(k)$ in the reciprocal space can be expressed by,

$$\vec{x}(p) = p_1 \vec{a}_1 + p_2 \vec{a}_2 + p_3 \vec{a}_3 \tag{69}$$

$$\vec{k}(k) = 2\pi (h_1 \vec{a}_1^{\,*} + h_2 \vec{a}_2^{\,*} + h_3 \vec{a}_3^{\,*}) \tag{70}$$

$\vec{a}_j$ and $\vec{a}_j^{\,*}$ are the primitive translation vectors in the real space and reciprocal space, respectively.

Similarly, by replacing the concentration deviation $\xi(p)$ in Eq.56 by its Fourier transforms x(k), given in Eq.68, the excess free energy of the solid solution can also be expressed in reciprocal space. As pointed by de Fontaine in the case of small amplitude perturbations such as those occurring during the initial stages of spinodal decomposition and at the very beginning of ordering, the expression for the excess free energy can be simplified significantly:

$$\Delta F \equiv F_M - F_0 \approx \frac{N}{2} \sum_{k} F''(k) \, |x(k)|^2 \tag{71}$$

The coefficient F"(k) in Eq.71 is expressed by

$$F''(k) = 2V(k) + \tau / q_0 \tag{72}$$

where V(k) is termed the reciprocal space potential which is the Fourier transform of the effective pair interaction potential V(r).This is expressed by,

$$V(r) = \frac{1}{2} [V_{AA}(r) + V_{BB}(r) - 2V_{AB}(r)] \tag{73}$$

where $V_{ij}(r)$ denotes the bonding energy of i and j atomic pair.

From Eq.71, it is seen that the excess free energy of a solid solution, which has started to deviate from its originally disordered state, is related to the energy alternation of various concentration waves localized at each reciprocal lattice site k. The contribution of each particular wave to the total excess free energy is determined by the sign of its coefficient, F"(k) (i.e. positive or negative), and the amount of the contribution is proportional to the square of the Fourier transform of the amplitude of the composition

fluctuation. A larger amplitude of concentration wave with a negative coefficient leads to decrease in free energy and therefore contributes to the driving force for the phase transformation. The kinetics of amplification, x(k,t) of specific concentration waves can be expressed by the following expression:

$$x(k,t) = x(k,0) \exp[\alpha(k)t] \tag{74}$$

Here x(k,0) is the amplitude of original concentration wave, and $\alpha(k)$ is termed as the amplification factor and is expressed by the following:

$$\alpha(k) = - M \beta(k) F''(k) \tag{75}$$

In this expression M is an atomic mobility parameter and $\beta(k)$ is a geometrical factor which depends on the disposition of nearest neighbors and the coordination number. Since both M and $\beta(k)$ are positive, continuous amplification of x(k,t) may occur only when F"(k) is negative and the reaction would occur spontaneously. When the wave factor $\vec{k}$ is small (i.e. the long wavelength), $\alpha(k)$ reduces to Cahn's amplification factor describing spinodal decomposition. Thus this approach actually contains Cahn's continum theory. When $\vec{k}$ is large (i.e. the short wavelength), rapidly amplified short wavelengths will induce continuous ordering. The expression in Eq.71 also predicts the possibility that there may exist different types of cooperative growth of the short and the long wavelengths. Cooperation of these two types of fluctuations may result in a greater amount of decrease in free energy. This would provide a stronger driving force which would lead to a more energetically favorable reaction path.

Based upon the concept of composition wave and the results of various

experimental investigations conducted on a series of binary and trinary alloy systems involving the continuous phase transformation of ordered intermetallic compounds, Laughlin and Soffa have proposed a graphical thermodynamical approach to elucidate various possible reaction paths involving the interplay of clustering and ordering processes in Ni-Ti system [2]. This approach provides a basis for understanding various complex processes and has proved to be useful in analyzing a number of other alloy systems. Therefore, this approach is briefly reviewed in the next section.

2.6 Graphical Thermodynamic Approach to Clustering and Ordering

The free energy of an ordered alloy depends not only on its composition, c, but also on its structural parameter [36]. The latter can be expressed by a long range ordering parameter, η. In this case, the free energy can be considered as a three dimensional surface, defined on the composition (c) - structural parameter (η) coordinate plane (Fig.11). However, the free energy curve associated with a disordered solid solution is only a function of composition and is a two-dimensional curve.

In Fig.12, the free energy curve of a disordered solid solution is assumed to exhibit a concave upwards trend at all compositions. The ordered free energy curve illustrated in the same figure represents the free energy of a series of homogeneous ordered solid solutions with optimum order parameter. This curve is actually a projection of a locus on the 3-D f-c-η surface. It can be considered that between a totally disordered state and an ordered state, there exists a series of nonequilibrium free energy states from SRO to

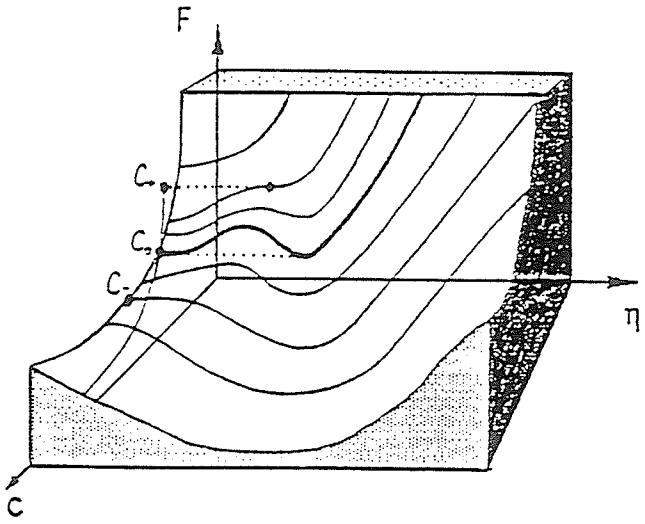

Fig.11 Schematic diagram illustrating variation in free energy as a function of both composition and long range parameter.

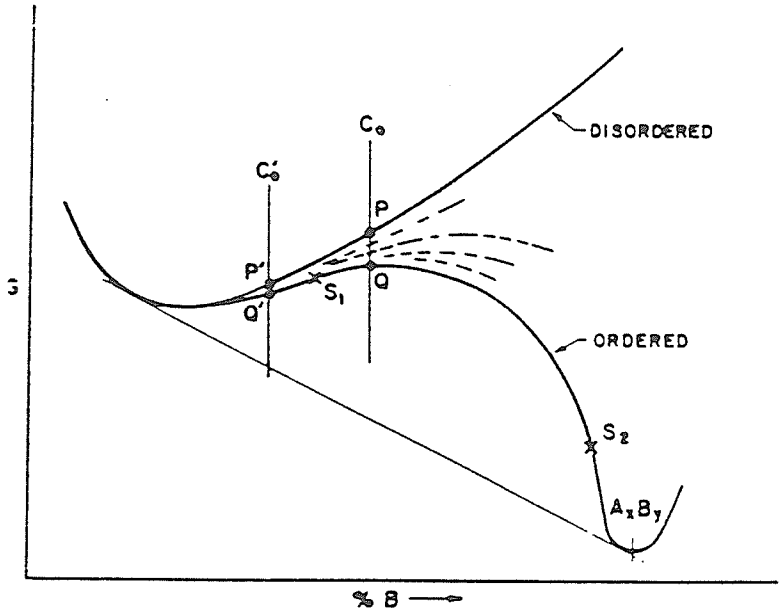

Fig.12 Hypothetical free energy-composition diagram for homogeneous disordered and ordered solutions.

imperfect LRO between the disordered and the lowest ordered curve. For this f - c regime, spinodal decomposition can only occur if the supersaturated solid solution orders first. A disordered solid solution of composition c_0 is metastable with respect to the equilibrium state of ordered A_xB_y precipitates and a disordered solid solution with composition c_1 However, the solid solution can lower its free energy from P to Q by a process of progressive ordering. This partially ordered state (point Q) is then unstable with respect to phase separation and the system can undergo a spinodal reaction involving continuous clustering and ordering leading to a metastable or stable two-phase mixture. In this case, the spinodal decomposition is entirely contingent on prior ordering. This situation is termed a conditional spinodal decomposition which was first proposed by Allen and Cahn [37]. On the other hand, the composition c_0', which is outside of the inflection point s_1, is also metastable with respect to precipitation of the ordered A_xB_y phase. It can lower its free energy from P' to Q' by ordering, even though the ordered state is still metastable with respect to the formation of the A_xB_y phase. The precipitation process will be accomplished via a nucleation and growth mechanism.

The interplay of clustering and ordering processes may occur via other reaction paths. In Fig.13, the free energy of a disordered solid solution shows a concave downwards shape and has inflections (S_1, S_2). A disordered solid solution of composition γ_0 is unstable with respect to phase separation and spontaneous unmixing of two phases will occur leading to a mixture of solute-enriched and solute-depleted regions. When the composition in the solute-enriched region exceeds the composition point O, the state of the solution is unstable with respect to the precipitation of the A_xB_y phase and ordering reaction occurs spontaneously. A continuous phase separation involving clustering and the ordering can then proceed. Eventually, a mixture of the equilibrium disordered solution and A_xB_y phase is generated by the common tangent construction. In this case, clustering

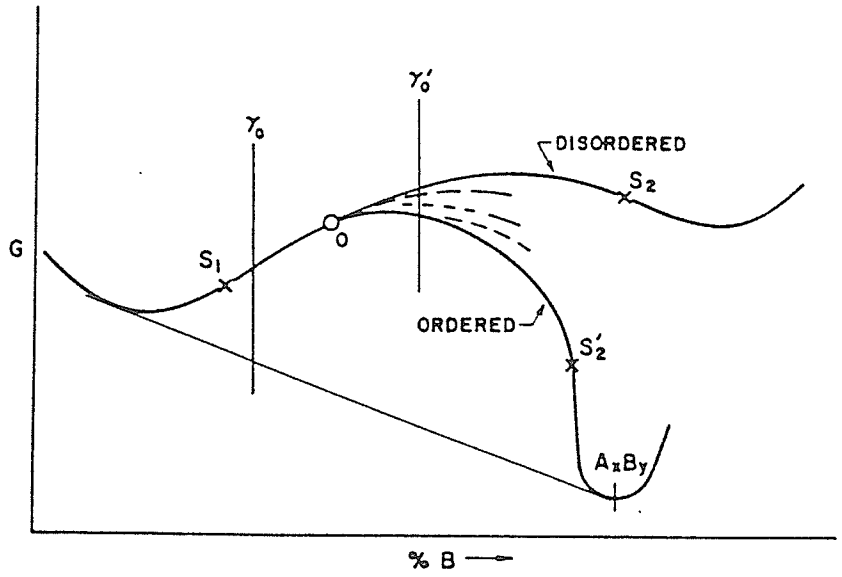

Fig.13 Hypothetical free energy-composition diagram for homogeneous disordered and ordered solutions.

precedes the ordering reaction and the whole system then progresses towards equilibrium via cooperative clustering and ordering. At composition point γ_0', the alloy is unstable with respect to clustering and ordering; i.e. long and short wavelength of composition fluctuations. It is likely that short range atomic exchange occurs rapidly to produce ordering, relaxing the free energy along the f-c-η surface towards the ordered curve. Simultaneously, a spinodal reaction leading to a continuous unmixing or phase separation can occur. This is in contrast to the previous case (c_0) in which the the supersaturated state is unstable initially only with respect to long wavelength compositional fluctuations.

The above discussion based on thermodynamic considerations elucidates various possible reaction paths related to the interplay of clustering and ordering processes. This approach is very straight forward and easy to understand. However, the approach using a decrease in free energy as a driving force to explain the reaction path can not predict what will happen in an unknown alloy system. This is because the thermodynamic calculation of free energy as a function of composition and the structure parameter is usually very difficult. Therefore, this approach is suitable to explain the interplay of clustering and ordering processes only after the characteristics of each process have been revealed.

2.7 Continuous Phase Transformation Involving the Interplay of Clustering and Ordering in Ni-base binary Alloy Systems

Ni-base superalloys are widely used in a variety of applications at elevated temperatures ranging from 650-1100 °C and in aggressive environments such as the combustion products of fuel and air, high temperature catalytic reactors etc. [38]. To

function satisfactorily in such a severe environment, these alloys must possess the properties such as outstanding high temperature strength, good creep and fatigue resistance, good ductility and impact resistance, and adequate resistance to hot corrosion [39].

From a microstructural point of view, the unique set of mechanical properties of these alloys is obtained from a fcc austenitic matrix which is solid-solution strengthened to some degree by the addition of various alloying elements and further strengthened very significantly by various kinds of precipitates. Among these precipitates, coherent Ni_3X type ordered intermetallic compounds are technologically most important.

2.7.1 Stability of the Intermetallic Compounds with Ni_3X Structure

Many Ni_3X type binary intermetallic compounds containing about 75 atomic percent Ni possess an ordered crystal structure, where Ni and X atoms, occupy fixed positions in a unit cell. In these compounds, element X has a certain degree of solid solubility in nickel. Fig.14 shows the occurrence of Ni_3X type intermetallic compounds in various Ni-X alloy systems [40]. The alloying elements X are arranged according to their position in the Periodic Table. Each rectangular space allotted to an element in this table contains the symbol of the element and its melting point at the top. The shaded area and the associated number represent the maximum solubility (in at%) of the element in nickel. The letter OR at the bottom of the rectangular space indicates that the compound is formed by an ordering reaction from the solid solution. A cross indicates

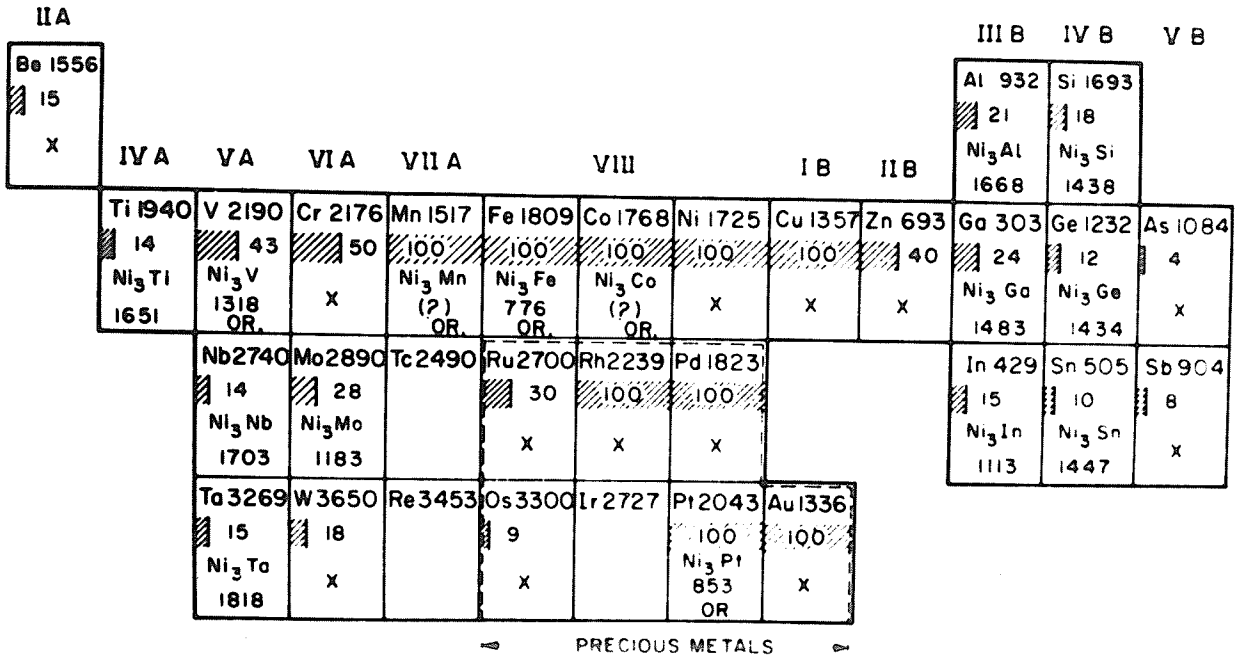

Fig.14 Occurrence of Ni_3X type intermetallics arranged according to their positions in the Periodic table.

an absence of Ni_3X phase.

It is seen in Fig.14 that there are many elements that form Ni_3X type intermetallic compounds. The compounds in the systems containing Mn, Fe, Co, and Pt are formed at relatively low temperature via an ordering reaction. Any high temperature strength related to the existence of ordered precipitates in these system is therefore unlikely. However, other elements such as Al, Ti, V, Mo, Ta, Ge etc. form Ni_3X type compounds which are stable up to relatively high temperatures. The solubility of these elements in nickel decreases rapidly with a decrease in temperature. Hence, these alloys are likely to be age hardenable and suitable for high temperature applications.

2.7.2 Crystal Structure of γ'

Although the Ni_3X type intermetallic compounds possess an identical atomic fraction of Ni, their crystal structures are widely different from each other as well as from the fcc crystal structure of the nickel matrix. The type of crystal structure as well as the lattice parameter of various Ni_3X type intermetallic compounds are listed in Table 1 [40]. Amongst these compounds Ni_3Al, Ni_3Ge, Ni_3Ga, Ni_3Si have an ordered $L1_2$ crystal structure shown in Fig.15a. These compounds are designated as γ' phase, with Ni atoms at the center of the faces (0, 1/2, 1/2) and X atoms at the cube corners (0, 0, 0). (X indicates Al, or Ga, or Ge, or Si atoms respectively).

The arrangement of atoms in $L1_2$ crystal structure is identical to that of A1 (fcc) crystal structure (Fig.15b), if ordering of the former is ignored. The stacking sequence in the close packed (111) planes of A1 and $L1_2$ is the same, e.g. A-B-C-A-B-C.

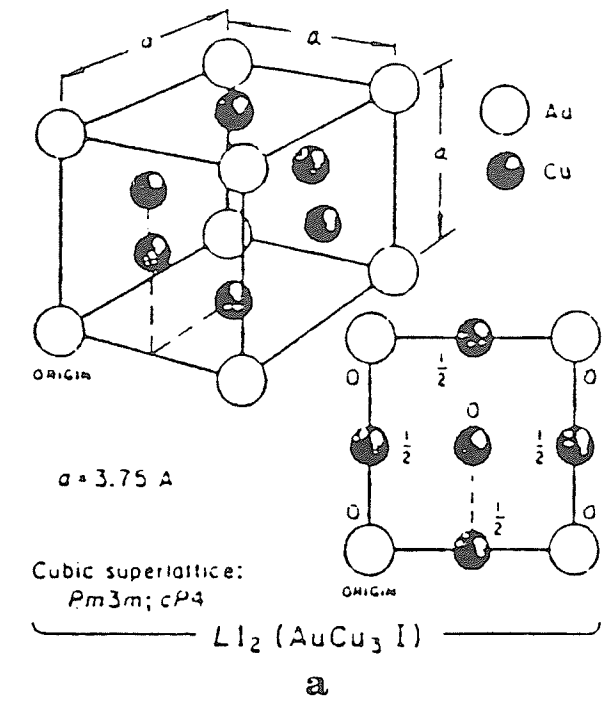

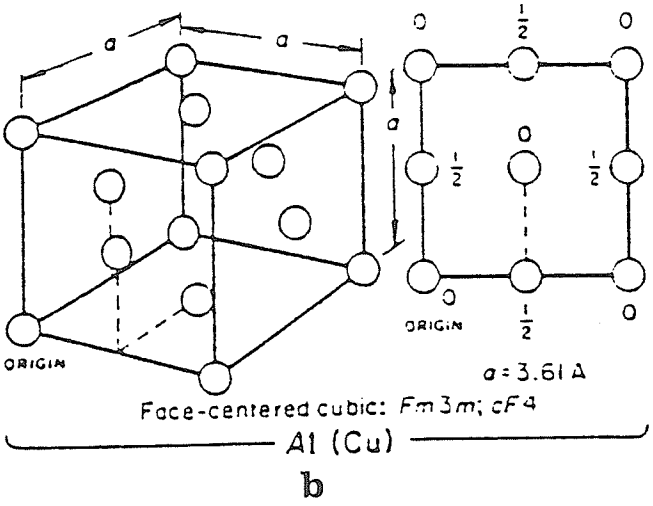

Fig.15 Crystal structure of (a) ordered $L1_2$ and (b) A1 (fcc).

Fig.16. shows the atomic arrangement in a (111) plane of $L1_2$ structure. Alternate positions in every other row parallel to the [110] directions are occupied by the solute atoms which form a triangular network. The ordered (111) planes are stacked so as to avoid solute-solute contacts. The atomic arrangement in the (001) planes in Ni is similar to the (001) planes of the $L1_2$ unit cell as well. The close similarity of atomic arrangement between $L1_2$ and A1 structure is likely to result in the formation of a coherent interface between the matrix and the precipitates with the interfacial energy expected to be low.

2.7.3 Coherency Between γ' and the Ni-Matrix [40]

The coherency between the matrix and the precipitates may induce elastic strain around the second phases that will hinder dislocation motion and lead to appreciable strengthening of the matrix. The misfit parameter δ between two coherently connected phases may be defined as $| d_p - d_m | / d_m$, where d represents the interatomic spacing along the matching direction in the matching plane at the precipitate-matrix interface, where p and m represent precipitate and matrix respectively. Usually, the d spacing along the [110] direction of the (111) plane in Ni and γ' are chosen for the calculation of misfit. These misfit values are also listed in Table 2. The magnitude of δ between Ni-and γ' phases is generally observed to be small, and therefore the coherency strain caused directly by the misfit is very small. The close similarity in atomic arrangement between $L1_2$ and A1 crystal structures is likely to give rise to the formation of low interfacial energy.

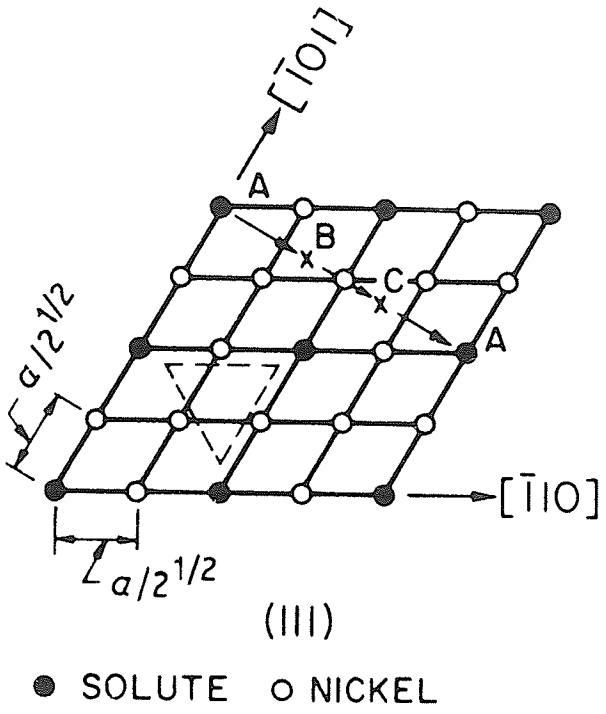

Fig.16 Atomic arrangement on (111) plane of $L1_2$ crystal structure.

Table 2. Structural characteristics of some Ni_3X type intermetallic compounds

Element X in Ni_3X	Upper temperature of stability of the compound (°C)	Crystal structure	Lattice parameter (nm)	Misfit $(d_p-d_{Ni})/d_{Ni} \times 100$ (%)
Al	1941	$L1_2$ (γ')	0.3567	1.2
Ti	1924	DO_{22} (η)	a=5.1010 c=8.3067	2.4
V	1591	DO_{22} (γ'')	a=3.5424 c=7.1731	0.5, 1.2
Nb	1976	Cu_3Ti type (β)	a=0.511 b=0.425 c=0.454	2.5, 4.6
Mo	1456	Cu_3Ti type (β)	a=0.506 b=0.422 c=0.445	1.6, 2.7
Ta	1866	Cu_3Ti type (β)	a=0.511 b=0.425 c=0.454	2.6, 4.9
Ta	2091	DO_{22} (γ'')	a=0.363 c=0.746	2.9, 4.4
Ga	1756	$L1_2$ (γ')	0.3582	1.7
Si	1586	$L1_2$ (γ')	0.3504	-0.6
Ge	1707	$L1_2$ (γ')	0.3566	1.2

2.7.4 Coarsening Resistance of γ'

The microstructure of a precipitation-hardened alloy system consists of different size of precipitates distributed in the matrix. To reduce the total interfacial area between the matrix and precipitates and hence to reduce the free energy of the system, the larger precipitates in these system have a tendency to grow at the expense of the smaller ones. This is a diffusion-controlled coarsening process and when this occurs, the average particle size, $\bar{r}$, is related to the time, t, by the following relation [41]

$$\bar{r}^{3} = (8V^{2} / 9RT) (\sigma c_{e} D) t \qquad (79)$$

Here V is the molar volume of the precipitate,σ is the interfacial energy per unit area between the precipitate and the matrix, c_e is the solubility of solute in the matrix and D is the volume diffusion coefficient.

It follows from this equation that a lower interfacial energy (σ) results in a lower coarsening rate. Due to a similarity in crystal structure and atomic arrangement the interfacial energy between A1 and $L1_2$ structures is generally low and the coarsening rate of the precipitate is therefore expected to be low.

Relatively small coherency strain along with low interfacial energy associated with coherent $L1_2$ precipitates result in a uniform distribution of precipitates with a high resistance to coarsening. These characteristics, therefore, bring about a stable microstructure and an appreciable strengthening effect. In commercial nickel-base alloys, γ'-Ni_3Al is often the main hardening phase. The γ' is an equilibrium second phase in both binary Ni-Al and ternary Ni-Cr-Al system and a metastable phase in the

Ni-Ti and Ni-Cr-Ti systems. These systems are the base for "superalloys" which owe their superior properties in part due to the close crystallographic matching of the γ' phase and the fcc matrix. The difference between the lattice parameters of the two phases is generally very small (≤ 0.25 %, depending on the composition) and the resulting small coherency strain and interfacial energy ($\gamma \approx 10$ -20 mJ / cm^2) confer a very low coarsening rate on precipitate particles. Therefore, the alloy overages extremely slowly even at 0.7 T_m [42].

2.7.5 Continuous Phase Transformation of γ' in Ni-Ti and Ni-Al Systems

The study of both Ni-Al and Ni-Ti alloy systems is of great technological importance since Al and Ti are the primary γ' formers, and γ' precipitates play a major role in the high temperature and high strength performance of Ni-base superalloys.

The process involving the precipitation of γ' in Ni-Al and Ni-Ti alloy systems has been suggested to be a typical example of continuous phase transformation. The precipitation of γ' generally involves two basic processes, viz., (a) clustering of solute atoms (phase separation) (b) ordering arrangement of solute and solvent atoms. The interplay of clustering and ordering has been suggested to control the entire precipitation process of a coherent, stable or metastable $L1_2$ phase within a normally fcc nickel matrix. This interplay has been also proposed to play an important role in determining the size, shape and distribution of γ' precipitates within the matrix, and hence it significantly influences the properties of the alloy.

A. Nickel-Aluminum System

The phase diagram of the Ni-Al binary system is shown in Fig.17a [43]. The intermetallic compound Ni_3Al-γ' has an $L1_2$ crystal structure. Based on the study of the phase transformation mechanism in this system, Gentry and Fine [44], Corey, Rosenblum and Greene [45] suggested that spinodal decomposition was involved in the formation of the ordered Ni_3Al-γ' precipitates. Hill and Ralph [46] performed a combined TEM and APFIM study of a Ni-14.1at%Al alloy aged at 625 °C. On the basis of the results of concentration profile analysis, they concluded that the formation of Ni_3Al phase involved a continuous phase separation (spinodal decomposition process) in conjunction with an ordering reaction. However, Ardell, Nicholson [23] reported that in alloys with a lower degree of supersaturation (lower solute concentration and/or aged at higher temperatures), a non-randomly aligned arrangement of γ' particles can also evolve from an initially random array (formed via nucleation and growth mechanism) through stress-affected diffusion during coarsening. Thus, in order to identify whether an alloy undergoes spinodal decomposition or not, investigations of the very early stages of decomposition are important. Only if the composition modulation persists from the very initial stages of ageing, can the mechanism of composition modulation be classified as a spinodal one.The results of Hill and Ralph [46] and Ardell et al [23] suggest that the actual decomposition path is very sensitive to the original state of the alloy, i.e. the degree of supersaturation which is determined by the composition and actual quenching rate.

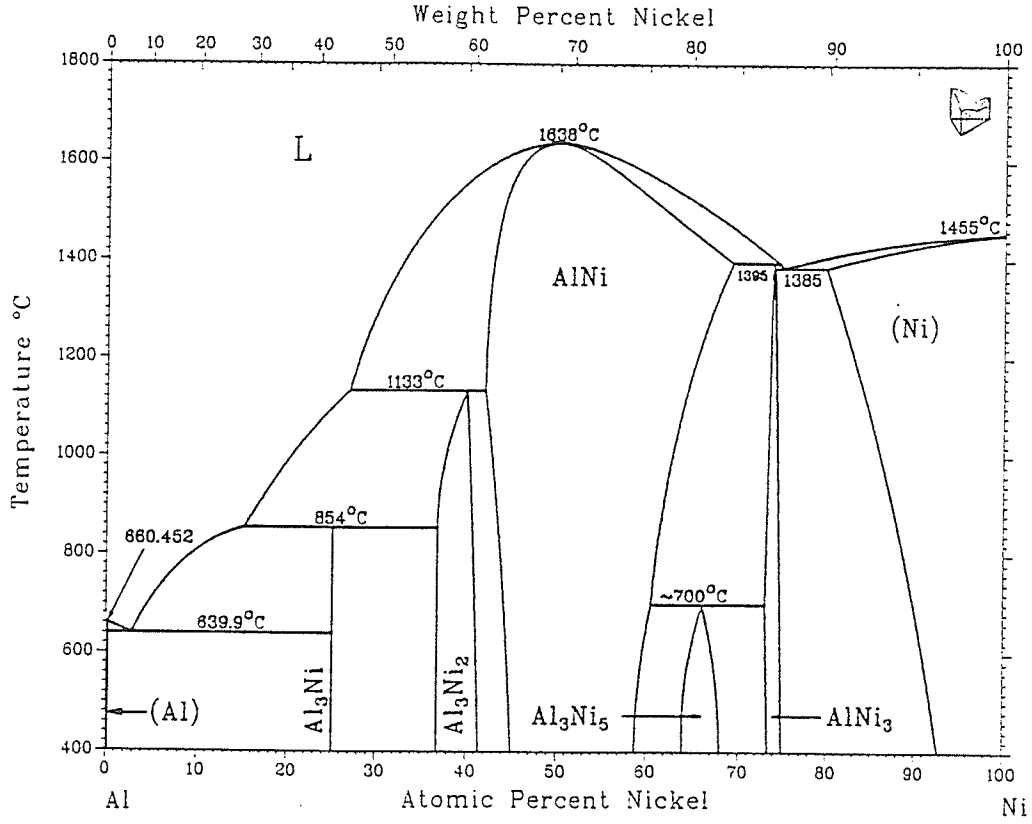

Fig.17a Binary phase diagram of Ni-Al system.

B. Ni-Ti System

Fig.17b shows a schematic Ni-rich section of the Ni-Ti phase diagram [20]. The equilibrium Ni_3Ti (η) phase is hexagonal but at high supersaturation a metastable γ' (Ni_3Ti with $L1_2$ crystal structure) phase precedes the formation of the equilibrium η phase in alloys containing a Ti concentration higher than 10 at%. Various experimental approaches have been applied to elucidate the decomposition mechanism involving clustering and ordering. These approaches include magnetic measurements [47], TEM and X-ray diffraction [48,49], high resolution electron microscopy (HRTEM) [50], small angle neutron scattering (SANS) [51] and APFIM [52]. A detailed and careful analysis of the data suggests that the formation of the metastable γ' phase generally occurs through a simultaneous composition modulation and atomic ordering and that this coupled continuous clustering and ordering transformation is preceded by continuous ordering of the matrix.

The common feature of these two alloy system is that the formation of the ordered γ' particles usually involves clustering and ordering reactions. These two reactions are not mutually exclusive processes in undercooled or supersaturated solid solution, but often proceed concomitantly and cooperatively during the decomposition of an alloy quenched from the single phase region. The transformation path is very sensitive to the original state of the alloy; e.g. composition, degree of supersaturation, quenching rate and ageing temperature, etc.

Like Ni_3Al-γ', the intermetallic compound Ni_3Ge-γ' also possesses an $L1_2$ crystal structure. From Table 2 it is seen that Ni_3Ge-γ' is very stable. It's upper temperature of stability is 1434 K, (i.e. 1161 °C). The lattice misfit between Ni_3Ge-γ' and the Ni

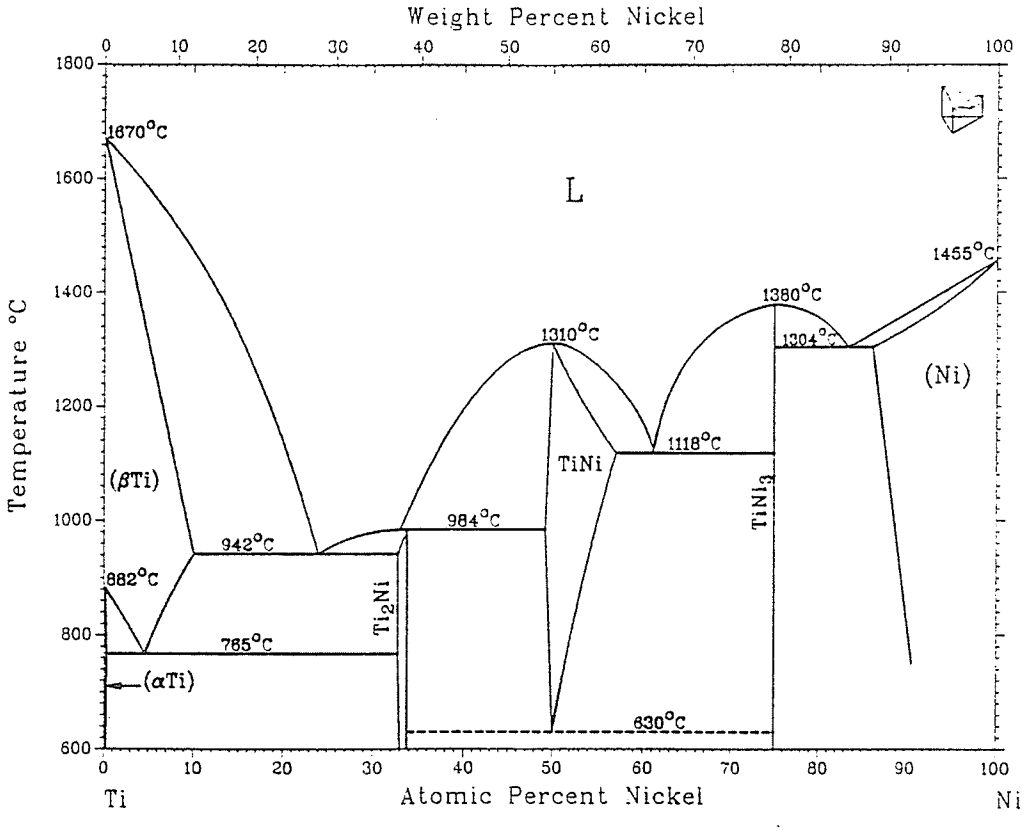

Fig.17b Binary phase diagram of Ni-Ti system.

matrix is 1.2% which is relatively low. Therefore, as indicated earlier, small interfacial and strain energy between Ni_3Ge-γ' and Ni-α matrix can be expected. According to these characteristics of Ni_3Ge-γ', it is probable that Ni_3Ge-γ' can also be a stable second phase capable of strengthening the Ni matrix. In addition, if the precipitation of Ni_3Ge-γ' can also follow a continuous phase transformation mechanism, like Ni_3Al and Ni_3Ti, and give rise to a uniform distribution of Ni_3Ge-γ' precipitates within the matrix, the strengthening will be more effective and of more practical significance. Furthermore, if the precipitation of Ni_3Ge-γ' from supersaturated Ni solid solutions also involves the clustering of Ge solute atoms, and an ordering reaction between Ni and Ge atoms, a study of this precipitation process will also be helpful for complete understanding of the interplay of these two reactions. Therefore, in the following sections, prior major experimental results conducted on the Ni-Ge system related to the precipitation process of Ni_3Ge-γ' are reviewed and discussed. Based upon this analysis, the scope of this study is defined and presented.

2.8 The Results of Previous Investigations Conducted on Ni-Ge System

Former investigations conducted on the Ni-Ge alloy system are limited and little data have been accumulated. In this section some characteristics of the Ni-Ge phase diagram at the Ni-rich end are discussed first, followed by the results of the physical metallurgical investigations carried out so far.

2.8.1 Ni-Ge phase Diagram

The solubility of germanium in nickel is reported to be appreciable. Dayer and Feschotte investigated the variation in solubility of germanium in nickel with temperature by electron microprobe analysis and established the phase boundary between α and $\alpha + \beta$ phase field in the Ni-Ge phase diagram which is illustrated in Fig.18 [53]. At room temperature, the solubility of germanium in nickel is about 12.0at% and reaches a maximum value of 16.0at% at 1124°C. Jena and Chaturvedi [54] measured the lattice parameters of Ni_3Ge saturated Ni-Ge solid solution at different temperatures. They used these data and the lattice parameters of the Ni-Ge solid solution to calculate the composition of the saturated solid solutions. Their thermodynamic analysis showed that the results were internally consistent and agreed with the result of Dayer and Feschotte [53]. Fig.18 shows that solubility of Ni_3Ge in Ni decreases rapidly with a decrease in temperature. Therefore, an appreciable amount of equilibrium Ni_3Ge is expected to precipitate when alloys with a composition in the two-phase region are isothermally aged at intermediate temperatures and the Ni matrix is likely to be effectively strengthened by the Ni_3Ge precipitates.

In addition, as stated earlier, the intermetallic compound Ni_3Ge is similar in many respects to Ni_3Al. Both Ni_3Ge and Ni_3Al have an ordered $L1_2$ crystal structure. One of the most striking features of these ordered intermetallic compounds is that there is an anomalous rise in flow stress with an increase in temperature, as shown in Fig.19 [56]. The peak value of flow stress of Ni_3Ge is about twice as much as that of Ni_3Al, but the peak position with respect to temperature in both the compounds is almost the same. From this point of view, the nickel matrix is likely to be strengthened more effectively at high temperatures by Ni_3Ge precipitates than by Ni_3Al precipitates.

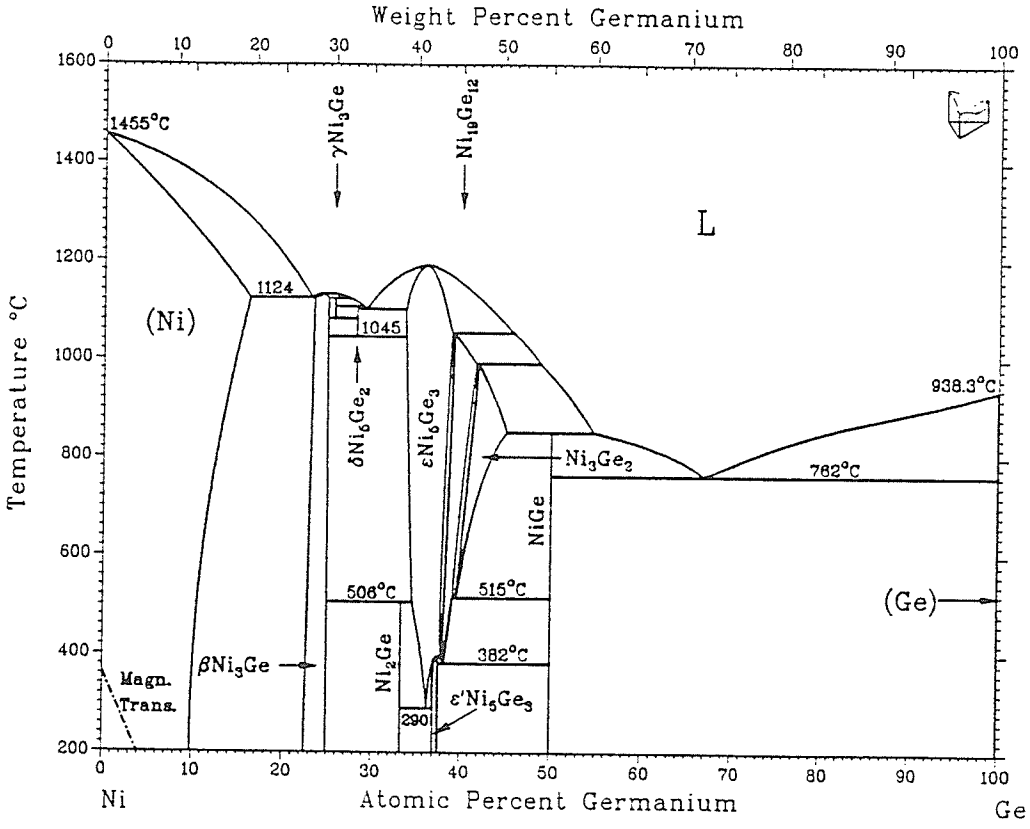

Fig.18 Phase diagram of Ni-Ge binary system.

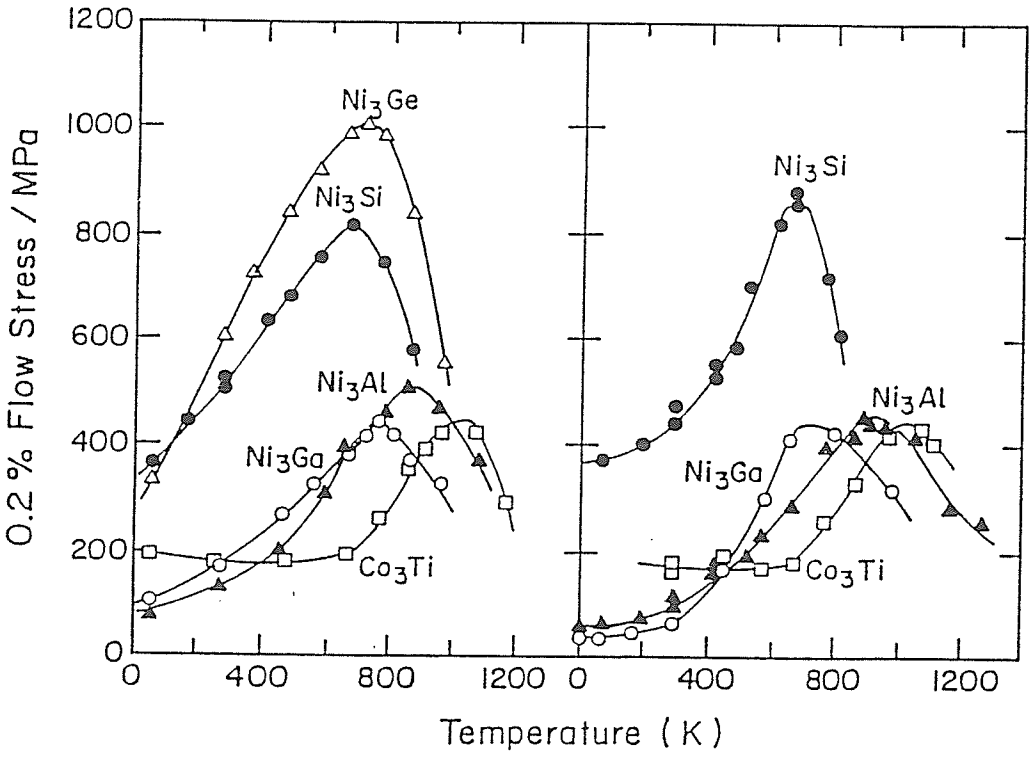

Fig.19 Variation in flow stress of some Ni_3X type intermetallics with temperature.

2.8.2 Important Physical Properties of Germanium and Nickel

Pure germanium possesses an A4, i.e. cubic diamond, crystal structure (Fig.20a). Each atom is surrounded by four nearest neighbors, positioned at the corners of a regular tetrahedron (Fig 20b) giving the structure a coordination number of 4. Its lattice parameter is 0.5657 nm.

The lattice parameter and the nearest neighbour distance of nickel and germanium are listed in Table 3. It is seen that the atomic size of nickel is larger than that of germanium and the difference in atomic diameter ($\delta = (d_{Ni} - d_{Ge}) / d_{Ni}$) is about 1.72%. This value lies within the favorable size zone ($\delta<15\%$) for alloying elements to have a large solid solubility in nickel (Fig.21). It appears that the Hume-Rothery size-factor principle [58] is to account for the fact that germanium has an appreciable solid solubility in the primary Ni-α terminal solid solution. Other physical properties of Ni and Ge which are related to the research presented in this dissertation are listed in table 4 and table 5, respectively.

2.8.3 Variation in Lattice Parameter and Microhardness with Germanium Concentration

Jena and Chaturvedi [60] have investigated the hardening effect of germanium and reported that the strengthening effect on the Ni lattice due to germanium addition is appreciable (Fig.22). In the single phase field, the microhardness of the nickel-germanium solid solution increases rapidly. However, at higher germanium

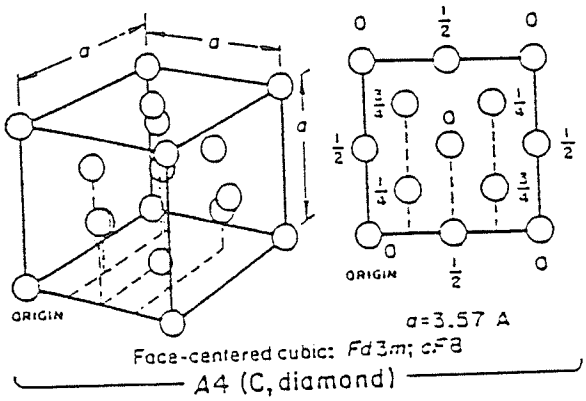

a

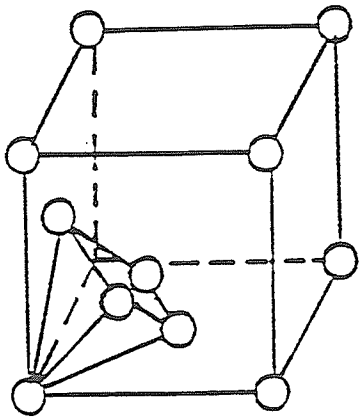

b

Fig.20 (a) Crystal structure of Germanium and (b) schematic diagram of atomic arrangement in a Ge unit cell.

TABLE 3. Lattice parameter and nearest interatomic distance of Ni and Ge [57]

Atomic No.	Element	Crystal structure	Lattice parameter (nm)	Nearest interatomic distance (nm)
28	Ni	fcc	0.3524	0.2492
32	Ge	cubic diamond	0.5650	0.2449

TABLE 4. Some Physical Properties of Ni [59]

atomic number	28
atomic weight	58.72
density (g/cm^3)	8.92
melting point (°C)	1455
crystal structure	fcc
lattice constant (nm)	0.3524
valence	2 or 3
outer-electron configuration	$3d^8 4s^2$
atomic radious (nm)	0.124
CRSS (psi)	407~1040
tensile strength (psi) (annealed)	46,000
yield strength (psi) (annealed)	8,500
elongation (%) (annealed)	30

TABLE 5. Some Physical Properties of Germanium [59]

atomic number	32
atomic weight	72.595
density (g/cm^3)	5.32
melting point (°C)	937
crystal structure	A4 (cubic diamond)
lattice constant (nm)	0.566
valence	4
outer-electron configuration	$4s^2 4p^2$
closest distance of atoms (metallic) (nm)	0.245

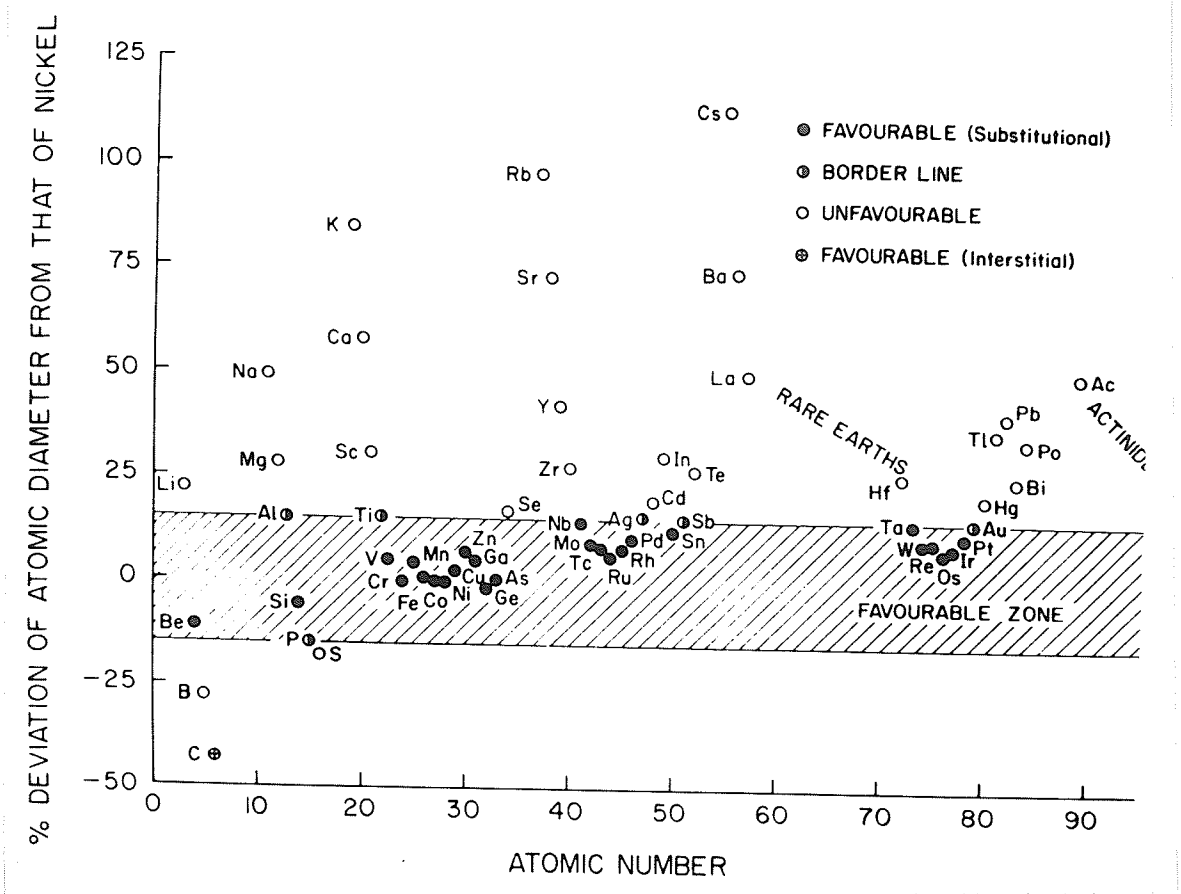

Fig.21 Favorable size zone for larger solubility in Ni.

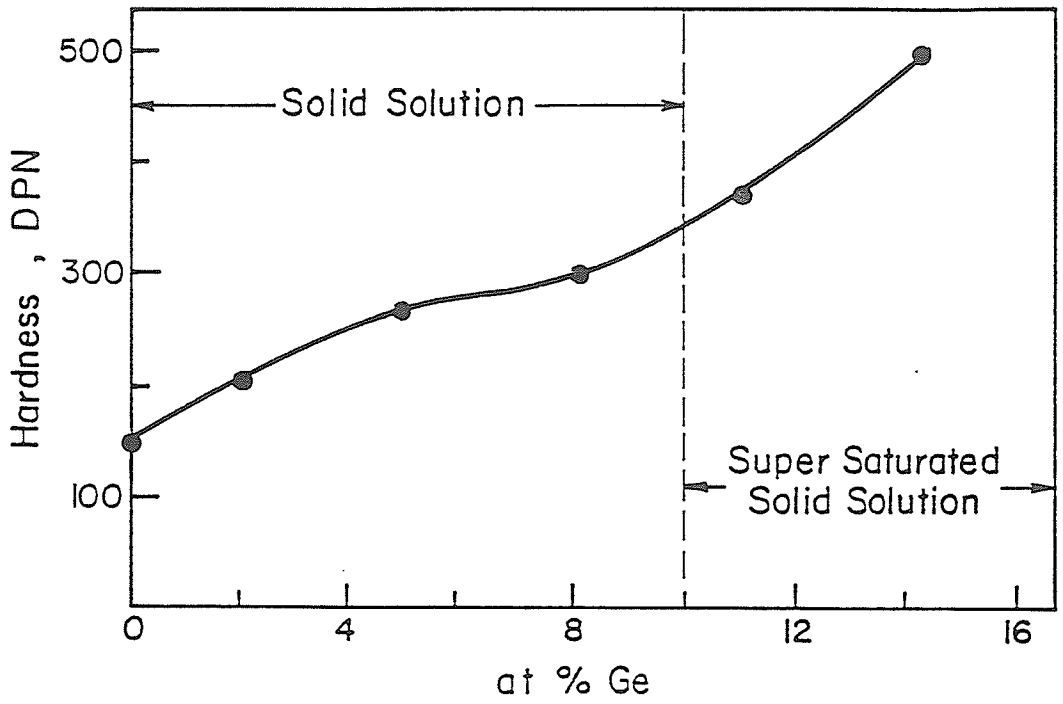

Fig.22 Variation in microhardness with composition in Ni-Ge alloys.

concentration the rate of increases in hardness decreases. In the two phase region, the strengthening effect is very appreciable. For example, they observed that the as quenched hardness of Ni-15 at%Ge alloy in as-quenched condition is about 500 VHN, which is a three-fold increase as compared to the hardness of pure nickel. They also examined the variation in lattice parameters with Ge concentration of the material (Fig.23) and found that the composition dependence of microhardness is almost exactly the same as that of the lattice parameter. This is reflected in the plot of variation in hardness against the variation in lattice parameter of Ni-Ge solid solutions which is observed to be linear (Fig.24) [60].

Grant and Pelloux [61] have investigated the strengthening effect of a number of solute atoms in nickel. They have found the increase in proof stress to be a linear function of the change in lattice parameter for all the solute atoms. Since the lattice parameter of solid solution provides information about the distribution of solute atoms in the matrix, and the lattice parameter data of the Ni-Ge solid solution shows a direct relationship with its mechanical properties, precise measurement of the lattice parameter is considered to be of great importance. However, in the Ni-Ge system, the experimental results of the study of the effect of Ge concentration on lattice parameters obtained by various investigators are not only not consistent with each other, but some of them differ significantly from each other as well (Fig.25). Pearson and Thompson [62] reported that the lattice parameter increases with germanium concentration at first with a decreasing rate and later on with an increasing rate. The general shape of the curve is very close to the one reported by Jena and Chaturvedi [60]. According to Lecocq [63], the lattice parameter increases at first with an increasing rate and later with a decreasing rate. Klement [64] on the other hand, reported the existence of a linear relationship between the lattice parameter and Ge concentration. In addition, values of the lattice parameter of Ni-Ge solid solutions reported by various investigators also

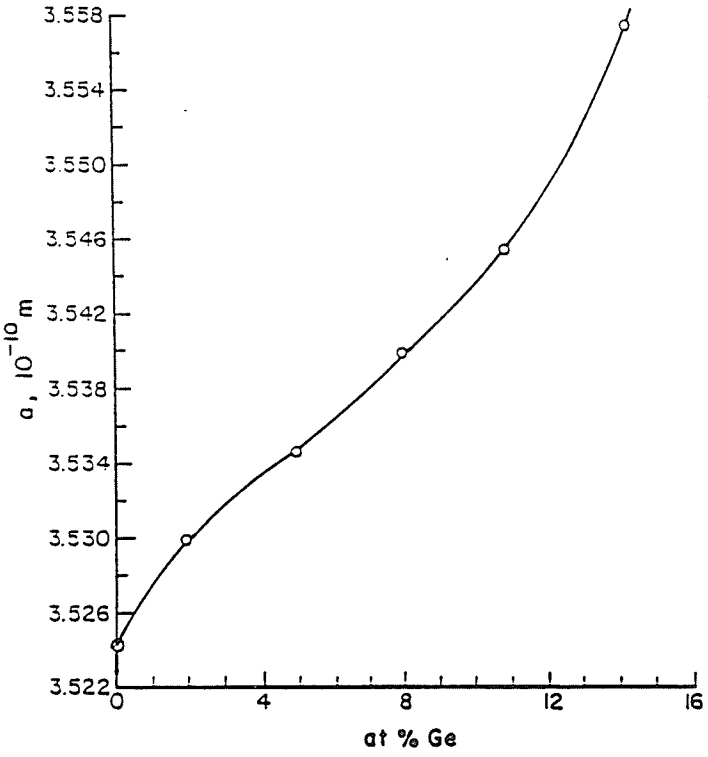

Fig.23 Variation in lattice parameter with composition in Ni-Ge alloys.

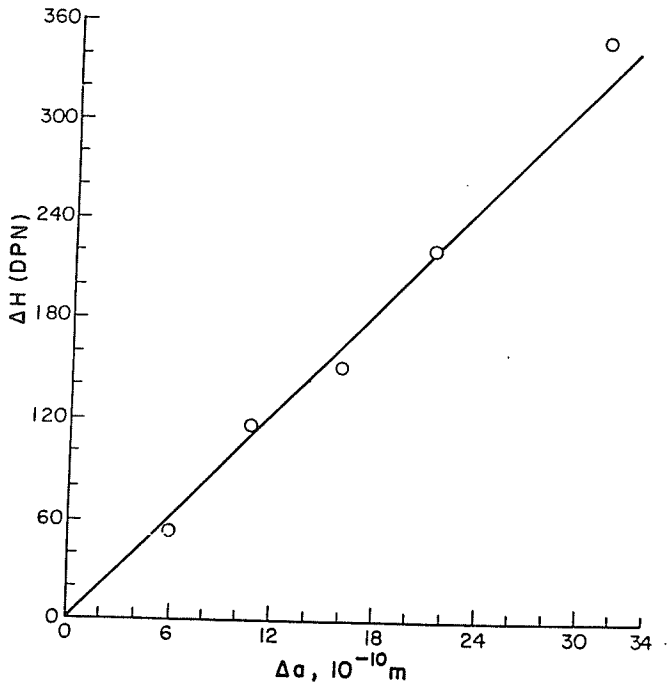

Fig.24 Variation in microhardness as a function of variation in lattice parameter.

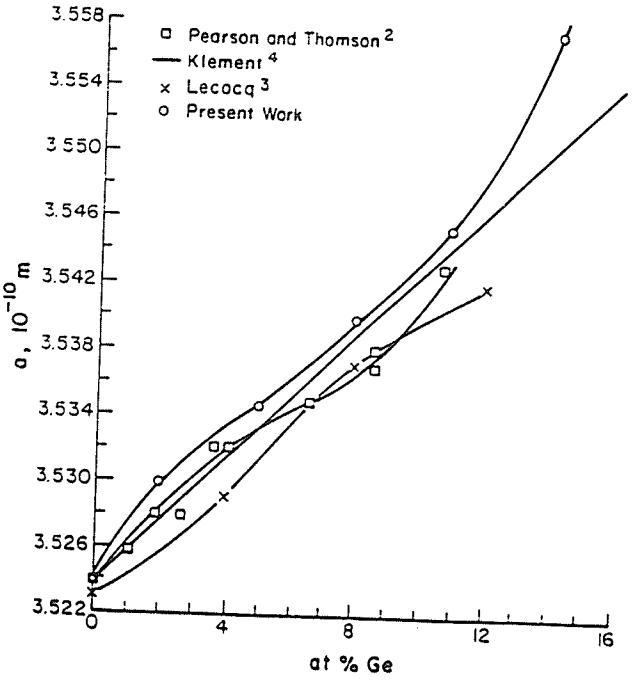

Fig.25 Variation in lattice parameter with composition investigated by different researchers.

differ from each other. Thus, it seems it is necessary to re-examine the influence of Ge content on the lattice parameter of Ni-Ge solid solutions.

2.8.4. Precipitation Behaviour of Ni_3Ge-γ' from Supersaturated α Solid Solutions [65]

The precipitation behaviour of Ni_3Ge from supersaturated Ni-α solid solutions has also been investigated by Jena and Chaturvedi [65]. An alloy containing 14.23 at%Ge was aged at several temperatures for various lengths of time and the lattice parameter was measured. It is reported that the lattice parameter of the solid solution decreases with increase in ageing time and gradually approaches a constant value (Fig.26). The higher the ageing temperature, the larger the constant value of the lattice parameter. These values are the lattice parameters of the saturated Ni-Ge solid solutions that are in equilibrium with Ni_3Ge phase. The lattice parameter of Ni_3Ge precipitates that formed at various ageing temperatures is independent of ageing temperature and time, measuring 0.35702 nm. Jena and Chaturvedi also suggested that there does not seem to be any metastable phase precipitating prior to the formation of equilibrium Ni_3Ge phase[65].

It is known that the slope at any point on the lattice parameter vs ageing time curve reflects the precipitation rate at that particular moment. If variation in the precipitation rate which occurs at the very beginning of the decomposition of the solid solution (da / dt, when $t \rightarrow 0$) is plotted against the ageing temperature (Fig.27), it is seen that at the highest ageing temperature the precipitation rate of Ni_3Ge is the lowest. Since the precipitation of Ni_3Ge is believed to be a diffusion controlled process, the

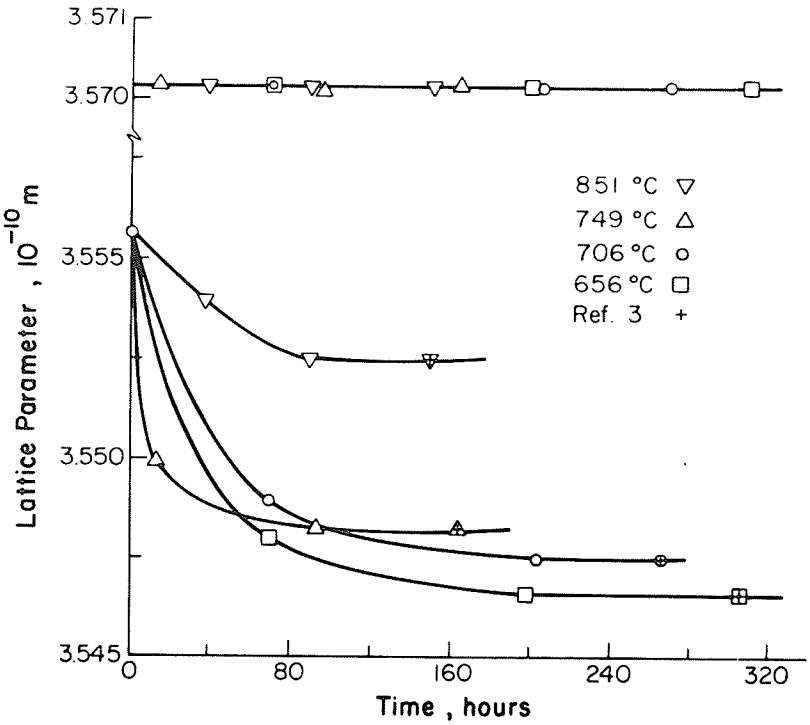

Fig.26 Effect of ageing temperature and time on the lattice parameter of Ni-14.23 at % Ge alloy.

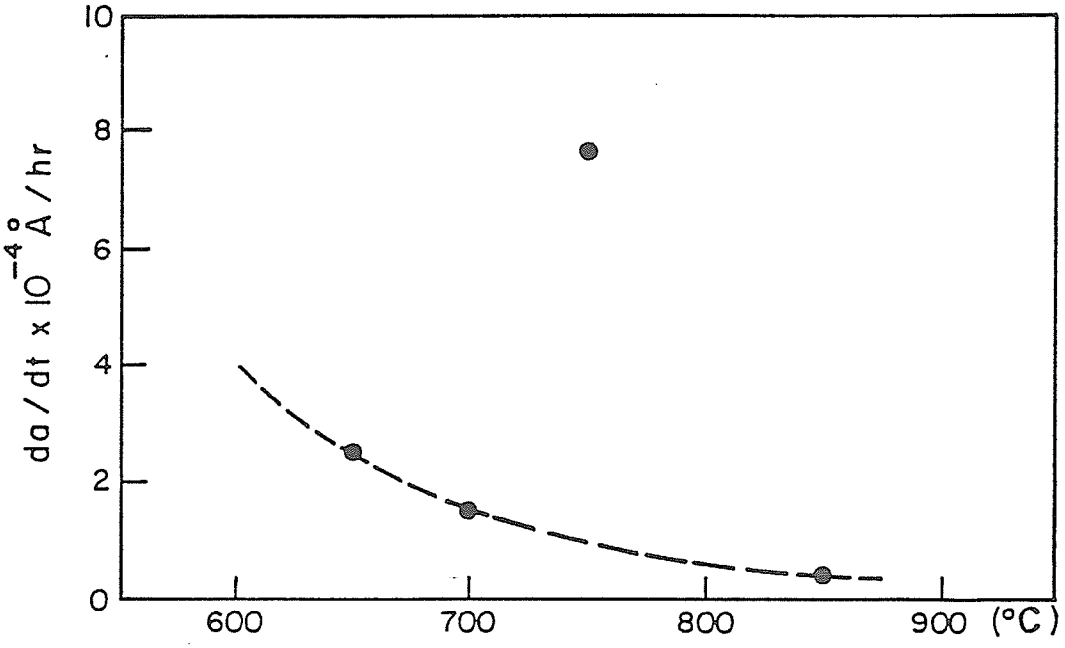

Fig.27 Variation in decomposition rate, da/dt, at the very beginning as a function of ageing temperature.

higher the ageing temperature the higher should be the rate of decomposition of the supersaturated solid solution. If the experimental results are correct, it seems possible that the decomposition mechanism may be different when the material is aged at different temperatures. At high temperatures, it seems there is an incubation period for the nucleation to occur and thus the precipitation rate at the beginning may be lower and the corresponding mechanism for the phase transformation may be nucleation and growth. However, at lower ageing temperatures, the lattice parameter of the Ni-Ge solid solution drops immediately and significantly, even at the very beginning of the precipitation process. This precipitation behaviour is similar to the one when a material undergoes spinodal decomposition. Since there is no energy barrier to this type of decomposition, the lattice parameters of the material, which are structure sensitive are often found to change immediately. However, the decomposition rate of a Ni-14.23at%Ge sample aged at 749 °C seems to be abnormal because at that temperature the precipitation rate is the highest of all the specimens aged in the temperature range of 650 to 850.°C. Although it was not reported, this phenomenon may be due to a slower quenching rate from the solution treatment temperature. Therefore, after quenching, the incubation period for the precipitation is already over and a certain amount of the second phase particles has precipitated. Thus, in order to investigate the early stages of transformation, which are important to identify the corresponding transformation mechanism, an appropriate use of properly controlled quenching rates is important and the cooling rates should be fast enough to suppress any possible decomposition during ageing.

When an alloy with a nominal composition of 16.69 at%Ge was solution treated and water quenched, a small percentage of insoluble particles of nickel saturated Ni_3Ge was observed[65]. Its composition was measured to be 22.5 at%Ge and the corresponding lattice parameter was measured to be 0.35702 nm. The shape of these

particles was found to be cubic [65].

The effect of ageing time on the hardness of a series of Ni-Ge alloys which were aged at 650 °C is shown in Fig.28 [65]. The general features of these curves are:

(1) The hardness increases very rapidly during the early stages of ageing.

(2) The hardness reaches a maximum value and becomes insensitive to the ageing time.

(3) The strengthening effect of Ni_3Ge is appreciable.

If the hardness values of the as-quenched alloys, shown in Fig.28, are plotted against the composition of the material, as shown in Fig 28, the hardness values show a significant increase when the Ge concentration is greater than 14at% (Fig.29). It seems that solution hardening by Ge atoms alone can not account for this sudden increase and it is, therefore likely that the early stage of Ni_3Ge precipitation contributes to the increase in hardness as well.

The studies carried out so far have not explained the mechanism of formation of Ni_3Ge precipitates in Ni-Ge alloys, especially when the degree of Ge supersaturation is high; e.g. when the Ge concentration is high and the material is aged at lower temperatures. It is likely that in these situations a continuous phase transformation may occur. The corresponding composition region is probably from 13 to 16 at%Ge, and the ageing temperature is likely to be in the range of 500-650 °C. When the Ge concentration is lower than 13at% the degree of Ge saturation in Ni is low and when, thermodynamically, the energy barrier for the transformation is high, Ni_3Ge may

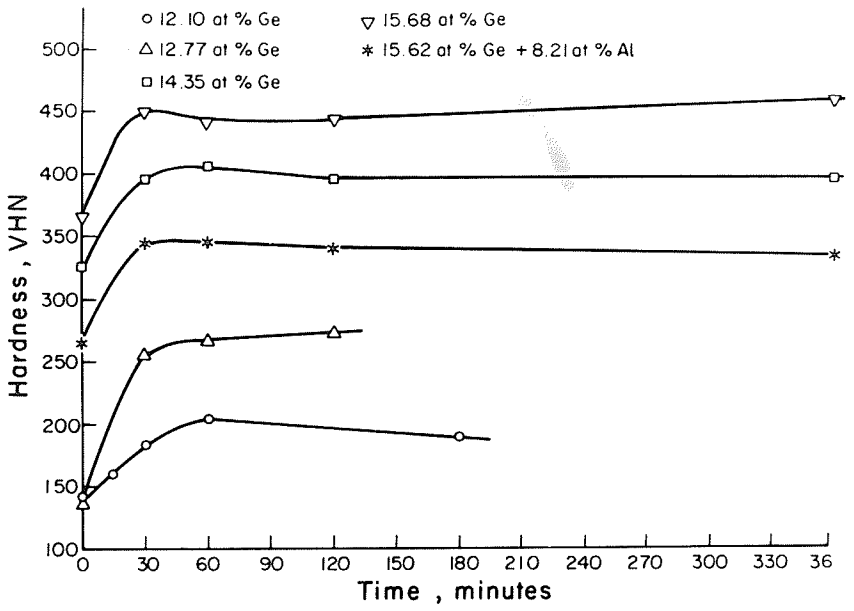

Fig.28 Effect of ageing time on hardness of Ni-Ge alloys at 650°C.

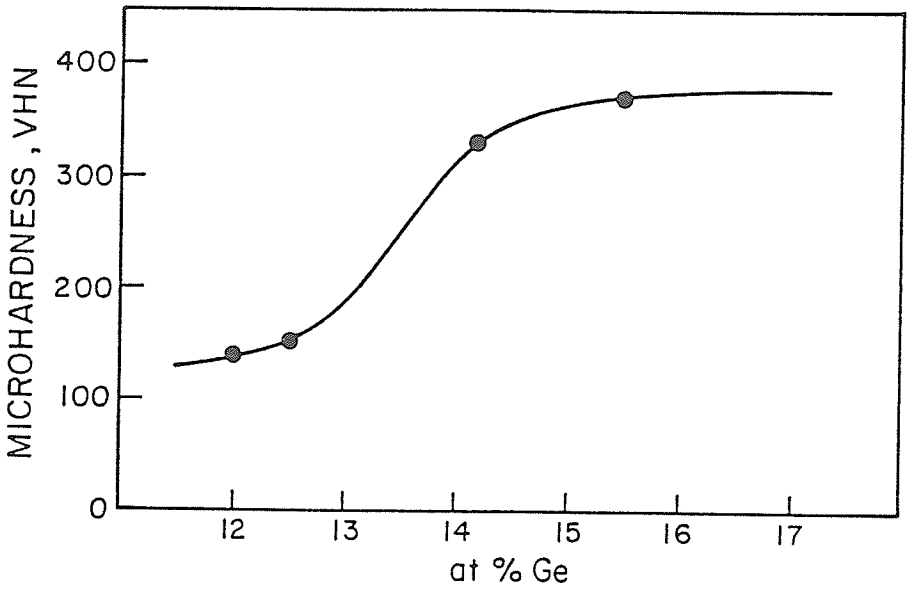

Fig.29 Variation in microhardness with composition.

precipitate at some energically favorable sites like crystal defects. In this case, conventional nucleation and growth may become the controlling mechanism for the precipitates of Ni_3Ge, which is not the major thrust of the present research. When the Ge concentration is higher than 16at%, there already exists a certain amount of insoluble Ni_3Ge particles even in the as-quenched alloys. The precipitation behaviour of these alloys is also not the major emphasis of this research. The major thrust of the present study is described next.

2.9 Scope of This Study

It is recognized from the review of the research carried out so far on Ni-Ge alloys that the precipitation rate of Ni_3Ge, even at the very beginning of the transformation, is relatively high. This implies that the energy barrier for the process is likely to be low. It is also recognized from the analysis of the published results that the phase diagrams at the Ni-rich terminal of Ni-Ge, Ni-Al and Ni-Ti binary alloys are very similar to each other. For example, (1) each system possesses Ni_3X (X = Al or Ti or Ge) type intermetallic compound with a $L1_2$ type crystal structure which is stable up to relatively high temperatures, (2) the crystal structures of the fcc matrix and $L1_2$ type Ni_3X compounds are similar, and the lattice parameter mismatch between the two is relatively small. The latter implies that a small coherency strain as well as a low interfacial energy are expected to be associated with precipitates when these intermetallic compounds precipitate from supersaturated nickel matrix. In Ni-Al and Ni-Ti alloy systems, a great deal of data has been accumulated suggesting that at high supersaturations spinodal decomposition and ordering occur together (or one occurs first and then they cooperate with each other). Therefore, it seems possible that a spinodal decomposition, in conjunction with a first order type order-disorder phase

transformation, occurs in the Ni-Ge alloy system during quenching from the solution treatment temperature and during the early stages of ageing that follow. It is likely that this is responsible for the rapid increase in hardness that has been observed in water quenched Ni-Ge alloys when the composition is in the two phase field [65]. It has also been shown, both experimentally and theoretically, that clustering and ordering processes often proceed continuously and cooperatively during the decomposition of an alloy quenched from the single phase region into the two phase region [2, 66-69]. This has been particularly elucidated in alloys such as Fe-Al binary alloys, where the order-disorder transformation [A2→B2] is of the second or higher order [66]. However, the interplay of clustering and ordering processes, especially in the A1→ $L1_2$ type phase transformation, is generally not well understood. Thus, a study conducted on the Ni-Ge system is likely to reveal some valuable information about these two processes.

Jena and Chaturvedi [65] have described the general features of the precipitate process of Ni_3Ge occurring in supersaturated Ni-Ge solid solutions. However, the evolution of precipitates, especially during the early stages, is still not clear and the corresponding transformation mechanism remains unknown. Moreover, a complete understanding of the precipitation behaviour of Ni_3Ge may be of technological benefit in finding practical applications of Ni_3Ge as an age-hardening agent for the development of high temperature and high strength materials. Therefore, an investigation needs to be conducted on the ageing behaviour of supersaturated Ni-Ge alloys.

To carry out an investigation of the various modes of decomposition of Ni-Ge solid solutions and the formation of Ni_3Ge precipitates, several metallurgical parameters have to be selected. The first of these is the composition of the Ni-Ge

alloys. In order to study the effect of Ge concentration on the decomposition behaviour of Ni-Ge solid solutions, alloys in the range of 0-15at% Ge were selected. The second problem is to select an appropriate approach to obtain a fast enough cooling rate from the single phase region. This includes the selection of a suitable furnace, appropriate sample thickness, and an effective way to determine if the early stages of Ni_3Ge precipitation are suppressed in the as-quenched sample. After that, a appropriate isothermal ageing temperature region would have to be determined. If the temperature is too high, the solute saturation of the alloy is low and Ni_3Ge may precipitate by a nucleation and growth mechanism which is not the major thrust of the present study. Based on preliminary experiments, it was found that (1) the fastest cooling rate from the single phase region is obtained by using a vertical furnace and quenching the samples in iced brine, and (2) the optimum temperature for isothermal transformation of Ni-Ge solid solutions is in the 500-600 °C range. X-ray diffraction and TEM techniques were mainly used to observe and record microstructural changes in samples of Ni-Ge alloys heat treated in a number of ways. The variation in microhardness of the aged alloy samples with aging time was also determined.

The literature review indicates that although Ni_3Ge shows a promise as an age-hardening agent for high temperature and high strength applications, the studies conducted on the Ni-Ge system are actually very limited. Some observations are even confusing. For example, in dilute Ni-Ge solid solutions, the atomic size of germanium is observed to be smaller than that of nickel (Table 3 and 4). Based on these data, their atomic size difference is found to be within the favorable size zone for germanium atoms to be in solid solutions in nickel. Therefore, the appreciable solid solubility of germanium observed in nickel seems to be reasonable. However, the lattice parameters of the Ni-Ge solutions show an increase with germanium concentration indicating that

the addition of germanium actually expands the nickel lattice. Therefore, the atomic size of germanium appears to be not only larger than that given in Table 5, but also larger than that of nickel. This is consistent with the observed increase in hardness with an increase in germanium concentration. However, the observed increase in hardness is far greater than what is normally observed by solid solution hardening. Therefore, in this research, the lattice parameter of a few dilute Ni-Ge solid solutions with different Ge concentrations in the range of 0-16at% have been re-examined and, by using the Vegard's law, the apparent atomic size (A.D.D.) of germanium in nickel has been determined.

Some researchers have reported that the lattice parameter of the Ni-Ge solid solution with Ge concentration ranging from 2 to 10at% shows an increase at a decreasing rate with an increase in Ge concentration; i.e. the lattice parameter vs. composition curve exhibits a significant negative deviation. A similar phenomenon was observed by Massalski [70] in his studies conducted upon Cu, Ag and Au alloyed with the elements of the B-subgroup of the Periodic Table. He suggested that when an intermediate phase exists in an alloy system there often exists a large electro-chemical interaction between the solute and the solvent atoms in the alloys of this system and the variation in the lattice parameter with composition often exhibits a downward trend [70]. If this is also true for the concentrated Ni-Ge solid solutions and Ge atoms do prefer to have more Ni atoms as their nearest neighbors, a certain degree of short range ordering (SRO) may exist in the solid solutions which would cause the lattice parameter of the material to increase at a decreasing rate. A diffuse scattering effect may also occur accordingly in these alloys. It is also recognized from the results reported by some researchers recently that the dislocation configuration in slightly deformed alloys with a certain degree of SRO is different from that observed in alloys where the solute atoms are randomly distributed [71,72]. The former alloys usually exhibit a planer distribution

of dislocations and the latter ones have a three dimensionally distributed dislocation substructure[71,72]. Therefore, the occurrence of short range ordering in various Ni-Ge alloys has been also studied by x-ray diffraction and TEM techniques.

CHAPTER 3

Experimental Procedures

3.1 Alloy Preparation

This study was conducted on Ni-Ge alloys containing up to 15at%Ge. Alloys with nominal compositions of 1, 2, 4, 6, 8, 10, 12 and 14at%Ge were prepared by a two stage melting process. First, a master alloy was prepared by induction melting 99.99% pure Ni and 99.999% pure Ge in the ratio of 2.5:1. The melt was then cast in a copper mold in an inert atmosphere of flowing argon. The resulting cylindrical ingot was sealed in an argon filled quartz tube and homogenized at 1100 °C for 7 days. After the homogeneity of the master alloy was confirmed by an optical microscopic examination, the chemical composition of the alloy was determined by wet chemical analysis by Arrow Laboratory Inc. (Kansas, USA). The required Ni-Ge alloys were then prepared by induction melting an appropriate amount of the master alloy and 99.99% pure Ni. These alloys were also cast in a copper mold in an atmosphere of flowing argon. These ingots were sealed in argon filled quartz tubes separately and homogenized at 1100 °C for one week. Subsequently these materials were examined by optical microscope for homogeneity and their chemical compositions were determined by wet chemical analysis. The chemical composition of the alloys studied is given in Table 6.

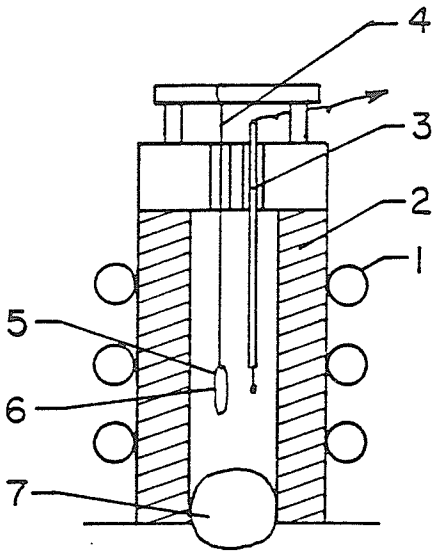

Fig.30 Schematic diagram illustrating sample arrangement inside a vertical furnace, (1) heating coil (2) vertical furnace (3) thermocouple (4) metal wire (5) quartz tube and (6) sample.

TABLE 6. Chemical Composition of the Ni-Ge Alloys

No.	1	2	3	4	5	6	7	8
at% Ge	0.92	1.87	2.04	4.87	7.82	9.75	11.98	14.56

3.2 Quenching and Ageing Procedure

2.0 mm thick samples were cut from the homogenized ingots with Ge concentrations less than 9.75at%. However, to avoid any possibility of early Ni_3Ge precipitation during quenching from the solution treatment temperature, 1.0 mm thick samples were cut from the alloys with compositions above 9.75at%Ge. The quenching and ageing procedures were carried out in a vertical furnace which is schematically illustrated in Fig.30. For solution treatment and quenching, samples were sealed separately in argon filled quartz tubes. These tubes were suspended individually inside the middle of the furnace by a piece of wire. The samples were solution treated at 1100 °C for another 20 minutes. After the solution heat treatment was completed, these tubes were rapidly dropped into iced brine by cutting the end of the wire outside the furnace. Then the tubes were broken immediately under the coolant. During ageing, samples were directly exposed to the heat in the furnace. However, flowing argon was supplied by introducing a glass tube into the furnace to protect the samples from oxidization. A thermocouple was inserted into the furnace and placed near the samples to monitor the heat treatment temperature. In this way, the temperature around the samples was controlled to within ±5°C.

3.3 Optical Microscopy

To examine the microstructural homogeneity of the master alloy as well as of the alloys prepared for this study, optical microscopic examination was used. The specimens were mounted and mechanically polished to 1 micron. They were then etched in a solution of nitric acid, glacial acetic acid and water in the ratio of 2:1:1 by volume. The microstructure of these samples were then observed using a Nikon metallographic microscope with magnifications ranging from 50x to 400x.

.3.4 X-Ray Diffraction

Powder samples were used to determine the lattice parameters of various alloys using X-ray diffraction technique. The powder was made from the bulk materials by filing. In order to obtain sharp x-ray diffraction peaks and get the measurement of the Bragg angle value accurately, this filed powder was further screened to obtain 325 mesh size particles. To remove the strains introduced by filing, the screened powder was annealed at 1100 °C for ten minutes. Before annealing, the powder samples were sealed separately in argon filled quartz tube in order to avoid possible oxidation during heat treatment.

The precise values of the lattice parameter of the powder samples were determined by a Philips Pw1710 powder diffractometer using Cu-K_α radiation and a Ni filter. The samples were scanned from a 2θ value of 10 ° to 140 ° and the scanning speed of the diffractometer was 6 °/min. Silicon powder was used as an internal standard. The standardization of 2θ data of these powder samples and determination of precise lattice parameter values were conducted by a computerized least-square method.

Strain relieved bulk samples with various Ge concentrations were used to study the intensity profile of X-ray diffraction peaks. In this technique the samples were scanned with an arc of 3° on each side of the 200 diffraction peaks. The corresponding scanning speed was 0.125°/min. All measurements were carried out at 21±2°C.

3.5 Microhardness Test

To determine the variation in hardness of the alloys with Ge concentration or

ageing time hardness of various samples was measured on a Vickers microhardness testing machine. A 50 g load was used and each reported value is an average of 20 measurements.

3.6 Transmission Electron Microscopy

To determine the effect of Ge addition on microstructural features of Ni-Ge solid solutions, transmission electron microscope (TEM) was used. Samples for TEM observation were prepared by mechanically polishing the material to 0.12 mm thickness using 240-600 grit abrasive paper. Discs of 3 mm diameter were obtained using a spark cutting machine. These 3 mm discs were then ultrasonically cleaned using an acetone bath. They were then electro-polished in a double jet polisher using a solution of 10% perchloric acid and 90% acetic acid. The working voltage ranged from about 45 to 55 v. The electro-polishing was carried out at room temperature. The thin foil samples were further polished for 15 minutes using an ion-milling machine to remove any surface oxidation. The working voltage and current for this process were 6 kv and 100 mA respectively. Thin foils were observed in a JEOL 2000FX TEM operated at 200 kv.

Due to the presence of microtwins in the dilute Ni-Ge solutions and Ge-rich zones in the concentrated solutions, as well as Ni_3Ge precipitates in the aged alloys, both bright field and central dark field techniques were used to confirm the existence of these microstructural features. The weak beam technique using g/3g technique was also employed to examine the existence of any separation of a unit dislocation. The trace analysis technique was used to analyze the shape and orientation of the Ge-rich zones present in the concentrated solid solutions.

During the electron diffraction study, satellite spots around the (200) and (400) electron diffraction spots were observed and recorded on the photographic films. However, since the spacing between the satellites and the main diffraction spots were very small, the satellite spots could not be identified individually in the printed electron diffraction patterns and the (200) and the (400) diffraction spots only exhibited a somewhat elongated shape along the [100] direction of the matrix. Therefore, the photographic plates containing the electron diffraction pattern on them were further examined by a transmission optical microscope. The satellites could be identified clearly due to the enlargement of the space between the satellites and the main diffraction spots. The optical microscopic image of the diffraction spot was then photographed directly from the optical microscope. These negative films were further enlarged and pictures were printed. By using this method, satellite effects due to the existence of spinodal decomposition within the alloy was not only observed in the TEM, but was also clearly recorded.

CHAPTER 4

Experimental Results and Analysis

This study was carried out by x-ray diffraction and TEM techniques to determine the nature of distribution of Ge solute atoms in Ni-Ge solid solutions and its influence on the microstructure of the material. The mechanism of formation of the Ni_3Ge phase precipitating from supersaturated Ni-Ge solid solution was also studied.

4.1 Variation in Lattice Parameters of the Ni-Ge Solid Solutions with Composition

1.0 mm thick samples of all the alloys were given a final solution heat treatment at 1100 °C and quenched in iced brine as described in Chapter 3. The x-ray diffractometer studies of those samples suggested them to have a single phase fcc structure. The lattice parameter of the solution treated specimens was measured by computerized x-ray powder analysis. The measured values of lattice parameters of these alloys are listed in Table 7. The measurement errors were always found to be within $\pm 1.0 \times 10^{-6}$ nm. It is seen that the addition of germanium in nickel expands the nickel lattice considerably. Fig.31 illustrates the variation in the lattice parameter of the alloys with Ge concentration. For comparison,

TABLE 7. Measured values of lattice parameter of Ni-rich Ni-Ge solid solutions

Composition, at%Ge	Lattice parameter, nm
0.00	0.3524
0.92	0.3527
1.87	0.3529
2.04	0.3530
4.87	0.3534
7.82	0.3540
9.75	0.3544
14.98	0.3548
14.56	0.3561

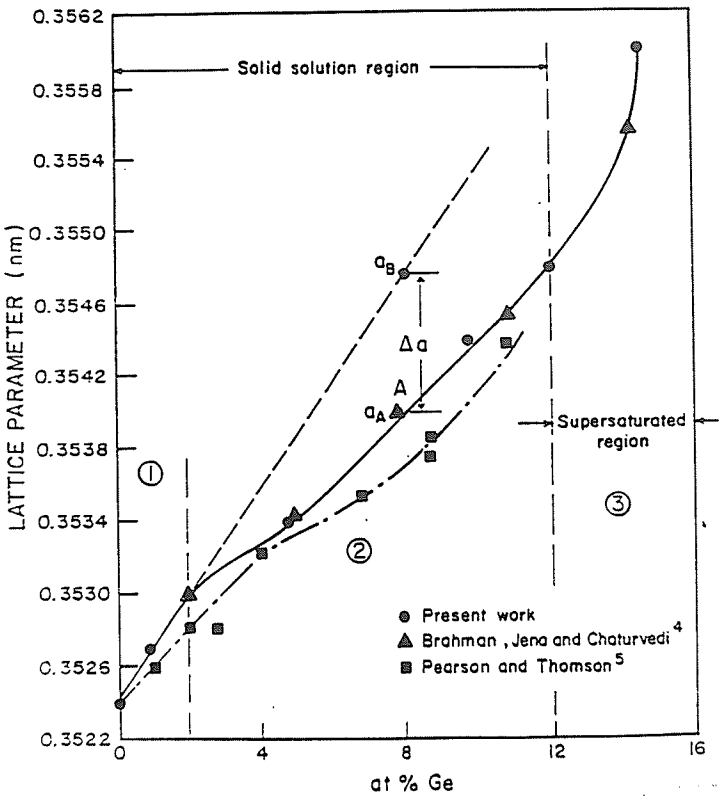

Fig.31 Variation in lattice parameter of Ni-Ge solid solution with Ge concentration.

the experimental results reported by Brahman, Jena and Chaturvedi [60] are also illustrated in Fig.31. These two sets of data are seen to be in excellent agreement. The results of the experimental data reported by Pearson et al.[62] are also included in Fig.31. The values of lattice parameter reported by them are found to be smaller than the values observed in this study. The lower values can probably be attributed to the following two reasons noted by Pearson et al [73]: (a) the presence of impurities in nickel which caused the measured value of lattice parameter of nickel to be lower than the normal value [74] and may also be responsible for the lower values of lattice parameter of Ni-rich Ni-Ge solid solutions reported by them, (b) some uncertain factors which were reported to have reduced the reproducibility of the results. However, all three sets of data shown in Fig.31 suggest an unusual variation in lattice parameter of the Ni-Ge solutions with Ge concentration which is described below.

On the basis of the nature of the lattice parameter vs composition curve, the curve can be divided into three regions as illustrated in Fig.31. In region 1, i.e. in the dilute solid solution region, with Ge concentration ranging from zero to about 2at%, a linear relationship between lattice parameter and Ge concentration is observed. In this region the addition of germanium to nickel is found to induce a considerable amount of expansion of the nickel lattice. In region 2, i.e. in the concentrated solid solutions, with Ge concentration ranging from 2at% to about 12at%, the values of lattice parameter exhibit a significant negative deviation from the linear plot as extrapolated from the dilute solid solution region. For example, at point A of the curve the lattice parameter difference (Δa) between the measured value, a_A, and the corresponding value in the extrapolated linear plot, a_B, is about 0.00075 nm. The difference is appreciable. The negative deviation is also seen to be composition dependent and increases with an increase in Ge concentration. A deviation from linearity has also been reported in the Ni-Sn and Ni-Si systems [75]. It should be noted that all these three solute elements, i.e. Si, Ge and Sn belong to the same group in the

Periodic Table of elements. In region 3, with composition ranging from 12 to 15at%, the alloys in the as-quenched condition are supersaturated solid solutions. The increase in lattice parameter with composition is appreciable and the rate of increase in lattice parameter increases with Ge concentration.

4.2 Calculation of the Apparent Atomic Diameter (A.A.D.) Value of Ge in the Dilute Solid Solution

Following the method suggested by Axon and Hume-Rothery [76], the apparent atomic diameter (A.A.D.) of germanium in nickel, d_{Ge}, can be calculated by using the following formula

$$d_{Ge} = [\, a - a_0 (1 - X_{Ge}) \,] \,/\, (\sqrt{2}\ X_{Ge}) \qquad (80)$$

where a is the lattice parameter of a dilute Ni-Ge solid solution with germanium concentration X_{Ge} (atomic percentage), and a_0 is the lattice parameter of pure nickel. The expression given in Eq.(80) is obtained by assuming that the solid solution obeys Vegard's Law. This implies that in the dilute solid solutions the atomic diameter of solvent atoms possesses the same value as the one in its pure unit cell and the lattice parameter of solid solution increases linearly with solute concentration. The values of lattice parameter of Ni-0.92at%Ge, Ni-1.87at%Ge and Ni-2.04at%Ge dilute solutions have been determined and given in Table 8, and the atomic diameter of Ni, whose coordination number is 12, is 0.2492 nm [57]. From these data the A.A.D. value of Ge in these dilute solutions can be calculated according to Eq.80. The results of the calculation are listed in Table 8. It is seen that the A.A.D. values of Ge in these three solid solutions are very close to each other and

TABLE 8. A.A.D value of Ge Ni-Ge dilute solid solutions

X_{Ge} (%)	a (nm)	A.A.D (nm)	Average of A.A.D (nm)	a_0 (nm) [86]
0.92	0.3527	0.273	0.272	0.3524
1.87	0.3530	0.271		
2.04	0.3507	0.271		

the average A.A.D. value of Ge in the dilute Ni-Ge solid solutions is 0.272 nm. However, the atomic diameter of Ge on the basis of closest distance of approach in the diamond cubic structure of Ge with coordination number of 4 is listed to be 0.2450 nm [57]. That is, the A..A.D. value of Ge in dilute Ni-Ge solid solutions is observed to increase by 11 percent.

Goldschmidt [77] studied the effect of co-ordination number of different crystal structures on the atomic diameter based on the closest distance of approach in the corresponding crystal lattice. He proposed that the atomic distance of elements whose coordination number (C.N.) is less than 12, can be expressed in terms of a crystal structure with a C.N. being equal to 12. To achieve this he found that the value of the atomic diameter should be multiplied by the following factors for various crystals whose C.N. is less than 12.

C.N. 8 (bcc)	×1.03
C.N. 6 (thomb)	×1.04
C.N. 4 (diamond)	×1.12

Goldschmidt's prediction has been supported by many experimental results and is generally accepted. It also seems to be supported by the present results obtained on dilute Ni-Ge solid solutions. The crystal structure of pure germanium is diamond cubic with a co-ordination number 4 and the average atomic diameter of germanium in nickel is calculated to be 11% more than that reported for Ge in diamond cubic structure. This is very close to the value suggested by the Goldschmidt's correction factor.

For comparison, the average atomic diameter of germanium in Au, Ag, Cu, Al, Ni

dilute solid solutions is listed in Table 9. It is seen that when germanium dissolves in these solid solutions with a fcc crystal structure, the A.A.D. values of Ge in all of them are larger than the atomic diameter of Ge in its pure diamond cubic crystal structure. Therefore, Goldschmidt's rule is generally obeyed. Furthermore, although the chemical valencies of Au, Ag, Cu, Al and Ni are known to be different from each other, there is no distinguishable difference in the A.A.D. values of germanium in these dilute solid solutions. This implies that in the dilute solid solutions, there seems to be no distinct electro-chemical interaction between germanium atoms and the solvent atoms. The linear relationship between lattice parameter and Ge concentration in the dilute solid solution region suggests that the lattice expansion effect of Ge addition to the solid solution is additive. This also suggests that there does not seem to exist any electro-chemical interaction between Ni-Ge and Ge-Ge atomic pairs. Therefore, in the case of dilute solid solutions each germanium atom can be treated as individual rigid balls distributed randomly within the lattice of the matrix with the expansion of the Ni lattice only due to the larger size of Ge atoms.

4.3 Consideration of A.A.D. Values of Ge in the Concentrated Solid Solutions

In concentrated Ni-Ge solid solutions, with concentrations ranging from 2-10 at% Ge, the lattice parameter increases with Ge concentration but at a decreasing rate. The lattice parameter - composition curve shows a downward shape and exhibits a negative deviation from the behaviour predicated by Vegard's Law (the dashed straight line in Fig.31). Usually, distinct changes in lattice parameter are expected to be related to some changes in the distribution and/or arrangement of atoms in the alloy. For example, a study [78] of the

TABLE 9. A.A.D. value of germanium atom in some fcc dilute solid solutions

solvent atoms	Au	Ag	Cu	Al	Ni
A.A.D. value (nm)	0.293	0.290	0.278	0.296	0.278

lattice spacing of transition metal alloys as a function of solute concentration reveals that there are many inflections in the lattice parameter - solute concentration curves with corresponding inflections in the magnetic properties. The magnetic properties of metals and alloys are known to depend on the electronic arrangement which is greatly influenced by the arrangement of atoms and the corresponding inter-atomic spacing in the crystal structure. Therefore, it is desirable to estimate the variation in atomic diameter of germanium in Ni-Ge solid solutions with Ge concentration and determine the reasons for the observed changes.

Fig.32a is a schematic diagram of a unit cell of pure nickel. The lattice parameter of Ni is a=0.35238 nm and its atomic diameter is 0.249 nm. The unit cell of the $L1_2$ ordered Ni_3Ge intermetallic compound, whose lattice parameter is a = 0.35702 nm, is shown in Fig.32b. In this unit cell, Ge atoms occupy corner sites and the Ni atoms are on the center site of each (100) plane. If it is assumed that the size of Ni atoms remains unchanged, the atomic diameter of Ge can be estimated as follows,

$$d_{Ge} = \sqrt{2}\, a - d_{Ni} = 0.256 \quad (\text{nm}) \tag{81}$$

However, in dilute Ni-Ge solutions, the A.A.D. value of Ge is found to be 0.278 nm. Therefore, it seems that when germanium atoms distribute randomly in the nickel lattice, and when there is no distinct electro-chemical interaction between Ni and Ge atoms, the size of germanium atoms is larger than that in the ordered Ni_3Ge crystal structure in which a strong interaction between Ni and Ge atoms is expected to exist. The high temperature stability of Ni_3Ge is an evidence of the strong bonding between Ni and Ge atoms in the $L1_2$ crystal structure. In concentrated Ni-Ge solid solutions, as the atomic percentage of Ge is small, it is reasonable to assume that the atomic diameter of Ni is

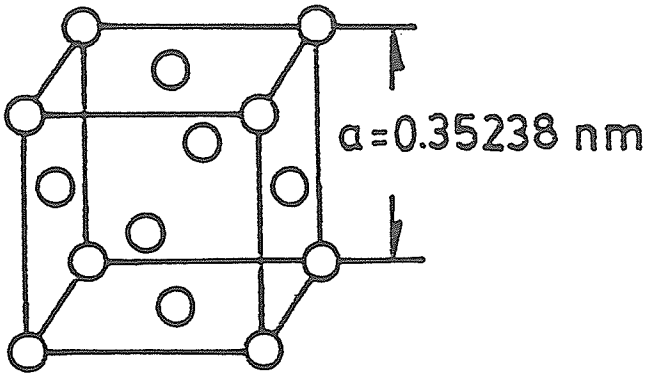

a

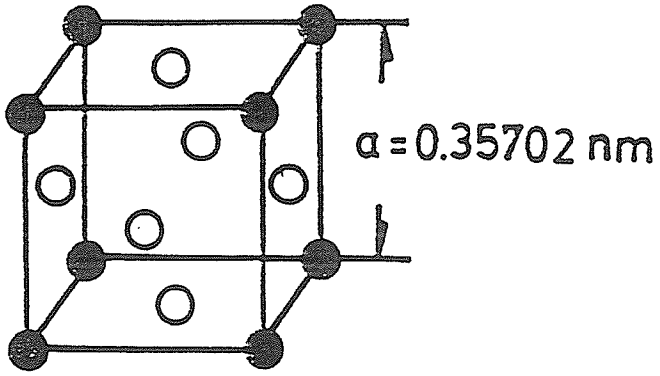

b

Fig.32 Schematic unit cell of (a) pure nickel and (b) Ni_3Ge.

composition independent. Therefore, the average atomic diameter of the average atoms in the Ni-Ge solid solution lattice, d_{av}, can be expressed by

$$d_{av} = x_{Ge}\, d_{Ge} + (1 - X_{Ge})\, d_{Ni} = a / \sqrt{2} \qquad (82)$$

where a is the lattice parameter of the solid solution with Ge concentration X_{Ge}. The meaning of this formula is that at any lattice site the probability of finding a Ge atom is the Ge concentration, X_{Ge}, and the average atomic size is the result of the contribution of both Ge and Ni atoms. The portion of the contribution is proportional to the probability of finding a Ge or a Ni atom at the lattice site, which is the composition of the alloy. Therefore, the atomic diameter of Ge in the solid solution can be expressed by

$$d_{Ge} = [\frac{a}{\sqrt{2}} - (1-X_{Ge})\, d_{Ni}] / X_{Ge} \qquad (83)$$

Since the values of the lattice parameter of the alloys, a, with different Ge concentrations are known, and listed in Table 7, the values of d_{Ge} can be obtained by simply substituting the corresponding a and X_{Ge} values into Eq.(83). The results of the calculation are listed in Table 10. For comparison, the A.A.D. value of Ge in Ni-saturated Ni_3Ge, i.e. Ni-22.5at%Ge alloy, is also listed in this table.

From Table 10 , it is seen that the A.A.D. values of Ge, i.e. d_{Ge}, in concentrated Ni-Ge solutions decreases with an increase in Ge concentration. These values are observed to progressively approach towards a value of 0.256 nm, which is the atomic diameter of Ge in the ordered Ni-saturated Ni_3Ge crystal structure. It seems that the atomic size of germanium in the solid solutions is significantly influenced by its surrounding environment in the solid solutions. In dilute Ni-Ge solutions, Ge atoms are randomly distributed in a

TABLE 10. Estimated values of atomic diameter of Ge in various Ni-Ge alloys

x_{Ge} (at%)	1.87	4.87	7.82	9.75	23.5
a(nm)	0.35295	0.35336	0.35397	0.35436	0.35720
d_{Ge} (nm)	0.280	0.267	0.266	0.265	0.256

totally disordered Ni lattice. Since, as discussed previously, there exists no distinguishable electro-chemical interaction between Ni and Ge atoms, there is expected to be a larger distance between a Ni and Ge pair. As the atomic diameter of Ni is assumed to be constant, it is reasonable that the A.A.D. of the Ge atom exhibits a larger value. However, when Ge atoms are regularly arranged in a totally ordered Ni_3Ge unit cell, each Ge atom is regularly surrounded by 12 Ni neighbors. As the interaction between Ni and Ge atoms is strong, a shorter atomic distance is expected to result. Therefore, the A.A.D. value of Ge atom, in this case, is smaller. Between these two extremes, the A..A.D. values of Ge in the concentrated solutions exhibit a transition from a larger value to a smaller value and the transition is a function of Ge concentration. It seems possible that, in concentrated Ni-Ge solid solutions Ge atoms or part of Ge atoms may stay in somewhat ordered regions. In other words, a certain degree of ordering may exist in the concentrated solid solutions. Since the Ge concentration in the solutions is still low, long range ordering is unlikely to exist. Instead, only short range ordering or a localized ordered state is likely to be present. However, more experimental evidence is required to verify this suggestion.

4.4 Variation in Microhardness of the Ni-Ge Solid Solutions with Composition

The variation in microhardness of the solid solutions in as-quenched condition is a function of germanium concentration. This is shown in Fig.33. The hardness variation shows a similar tendency to the one observed for the lattice parameter with Ge concentration. Based on the nature of the curve, it can also be divided into three regions. In the dilute nickel solid solution regime the hardness exhibits a rapid and appreciable increase

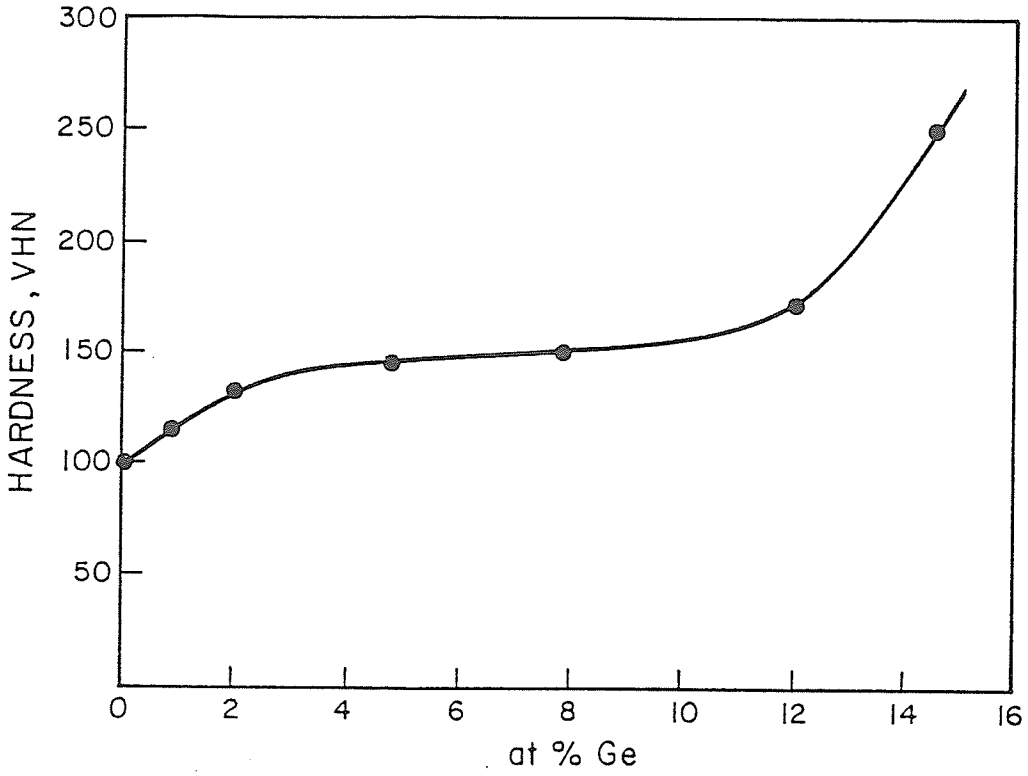

Fig.33 Variation in microhardness of the alloys with Ge concentration.

with increase in Ge concentration and the increase in hardness exhibits a linear relationship with Ge concentration. One atomic percent of germanium addition causes the hardness to increase by about 12%. However, in the concentrated Ni-Ge solid solution, the rate of the increase in hardness shows a decreasing trend. In the supersaturated solid solution regime, the hardness increases very rapidly again and the strengthening effect is very appreciable. For example, in the as-quenched condition the hardness of the Ni-14.56 at%Ge alloy is 250 VHN.

Usually, the hardness of an alloy reflects the capability of a material to resist plastic deformation. From a micromechanistic viewpoint, hardness reflects the resistance to the movement of dislocations due to their interaction with different types of obstacles. In the current microhardness test, the employed load is small and in order to avoid any grain boundary effect each measurement was conducted carefully so as to position the indentor fully within crystal grains. Therefore, the microhardness values obtained from the tests reflect the deformation behaviour of each indented crystal grain. Therefore, the observed variation in the value of microhardness with Ge concentration indicates that the deformation behaviour of Ni-Ge solid solutions in the as-quenched condition is also composition dependent. The analysis of the variation in lattice parameter with Ge concentration suggests that the distribution of germanium atoms in the dilute nickel solid solution is random. In the concentrated nickel solid solutions, however, it is suggested that a certain degree of short range ordering exists. It seems possible that the type of Ge distribution greatly influences the deformation behaviour of the material. It also seems possible that different types of deformation mechanisms may exist in the different composition regions. In the dilute solid solutions, since germanium atoms are randomly distributed they are likely to act as individual entities. Therefore, the observed strengthening effect may be related to the interaction of dislocations with these randomly distributed single obstacles. In accordance

with the calculation based on linear elasticity theory, the maximum interaction force between an edge dislocation and a solute atom is proportional to the term δ, which is the relative change in the lattice parameter of the matrix for the solute atom concentration X_B. The value of δ is given by $\delta = d(\ln a) / dX_B$ [79]. It is possible that the fast increase in hardness observed in the dilute nickel solid solutions is due to the large A.A.D. value of germanium which would cause an appreciable distortion of the nickel lattice and hence strengthen the matrix. In the concentrated Ni-Ge alloys, the solid solutions may be partially ordered. A portion of Ge atoms will still stay in the nickel lattice as individual entities while another portion may arrange themselves with more nickel solvents as their nearest neighbors and exhibit a certain degree of ordering. Therefore, the deformation behaviour of the alloys is likely to be governed by these two factors. In the supersaturated Ni-Ge solid solution region, the rapid and very large increase in hardness, and the deformation behaviour may be related to the effect of some early stages of decomposition of these unstable solid solutions, especially if this involves spinodal decomposition which progresses very rapidly. Therefore, the influence of the Ge addition on the deformation behaviour of the Ni-Ge solid solutions was studied by examining the dislocation substructure of slightly deformed specimens by thin film transmission electron microscopy.

4.5 TEM Observations of the Microstructural Features in Alloys 2% Deformed

4.5.1. Microstructural Features in Dilute Solid Solutions 2% Deformed

2.0 mm thick strips of the solution treated alloys with different Ge concentrations were deformed 2% by cold rolling. The microstructural features of Ni-0.92at%Ge and Ni-1.87at%Ge alloys 2% deformed were observed to be very similar and the substructure of both the alloys shows a network of three dimensional dislocations. Fig. 34 is a thin film micrograph, obtained by using weak beam technique, showing a typical dislocation substructure in Ni-1.87at%Ge alloy. In area A dislocations arrange themselves in a three dimensional array, whereas in area B only sparsely distributed dislocations are observed. The characteristics of dislocation distribution in different metals and alloys have been studied by many researchers. It has been found that the dislocation distribution in fcc materials after a low and medium degree of plastic deformation can be significantly different in different materials. Usually, dislocations in pure metals and dilute solid solutions show three dimensional arrangement, while in alloys with a low stacking fault energy (SFE) or with certain degree of short range ordering (SRO), the dislocation structure is more planar in nature. On the basis of the characteristics of dislocation configuration, the former category is termed as a wavy slip material and the latter is termed as a planar slip material [72]. Pure nickel, whose dislocation structure was studied by Karnthaler and Fisher [80], has been suggested to be a wavy slip material. In the present study, dilute Ni-Ge solid solutions after 2% deformation were observed to possess a three dimensional network of dislocations (e.g. Fig.34), which is similar to that observed in pure nickel. Therefore, it is concluded that dilute Ni-Ge solid solutions belong to the wavy slip material group.

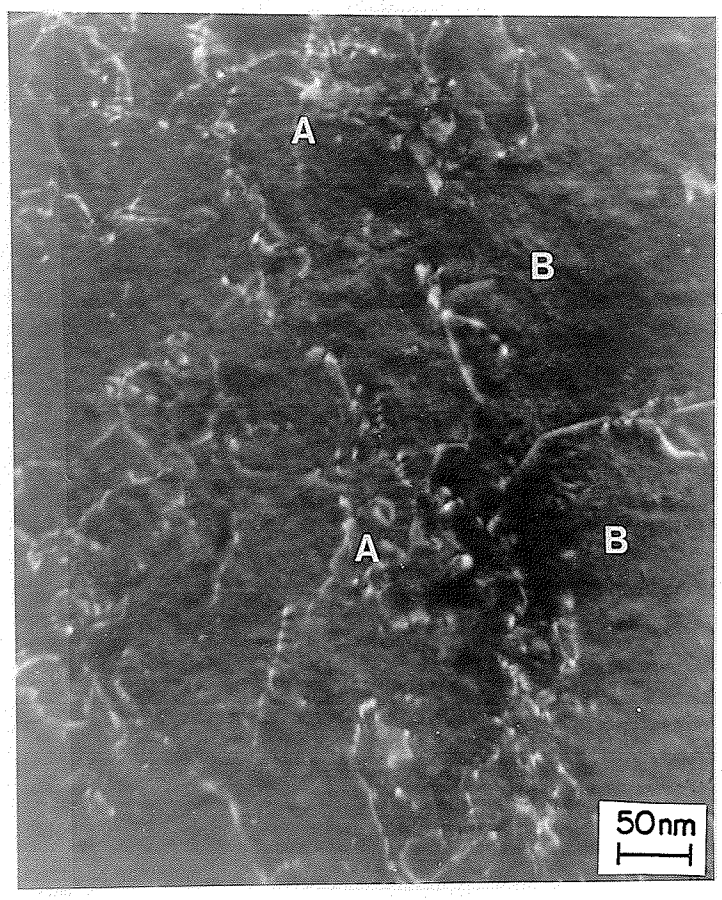

Fig.34 Three-dimensional dislocation configuration in a Ni-2at%Ge alloy 2% deformed.

Fig.35 Dislocations and microplates in a thin foil of the Ni-2at%Ge alloy 2% deformed.

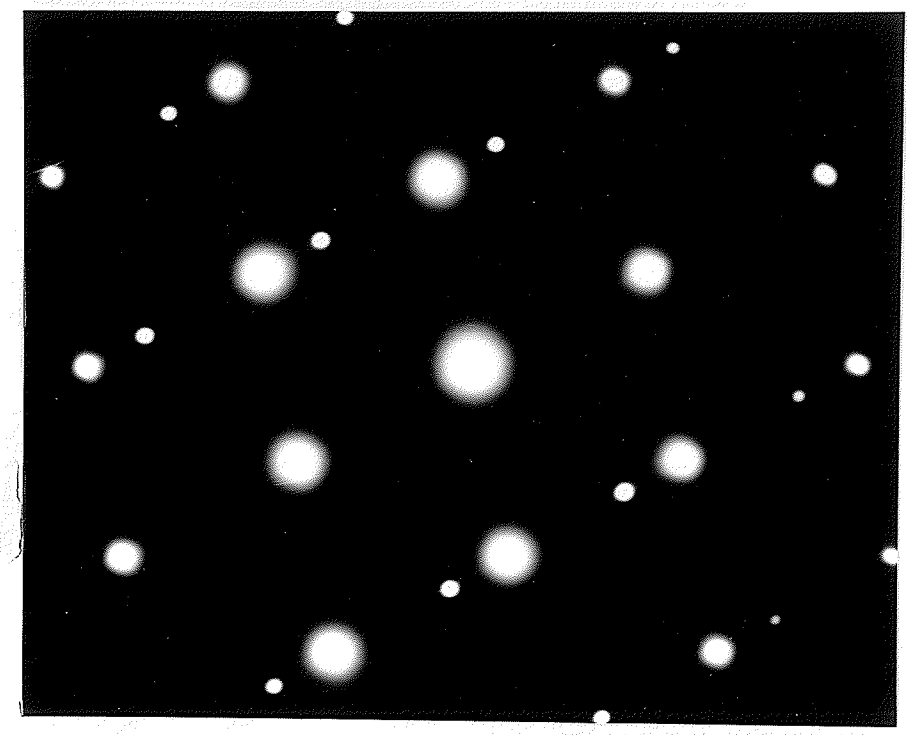

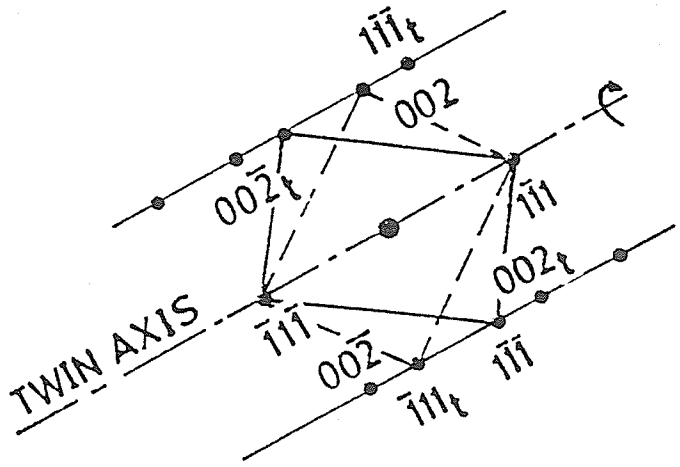

Fig.36 (a) SADP taken from the microplates in Fig.35 (B=[110]) and (b) indexed pattern of (a).

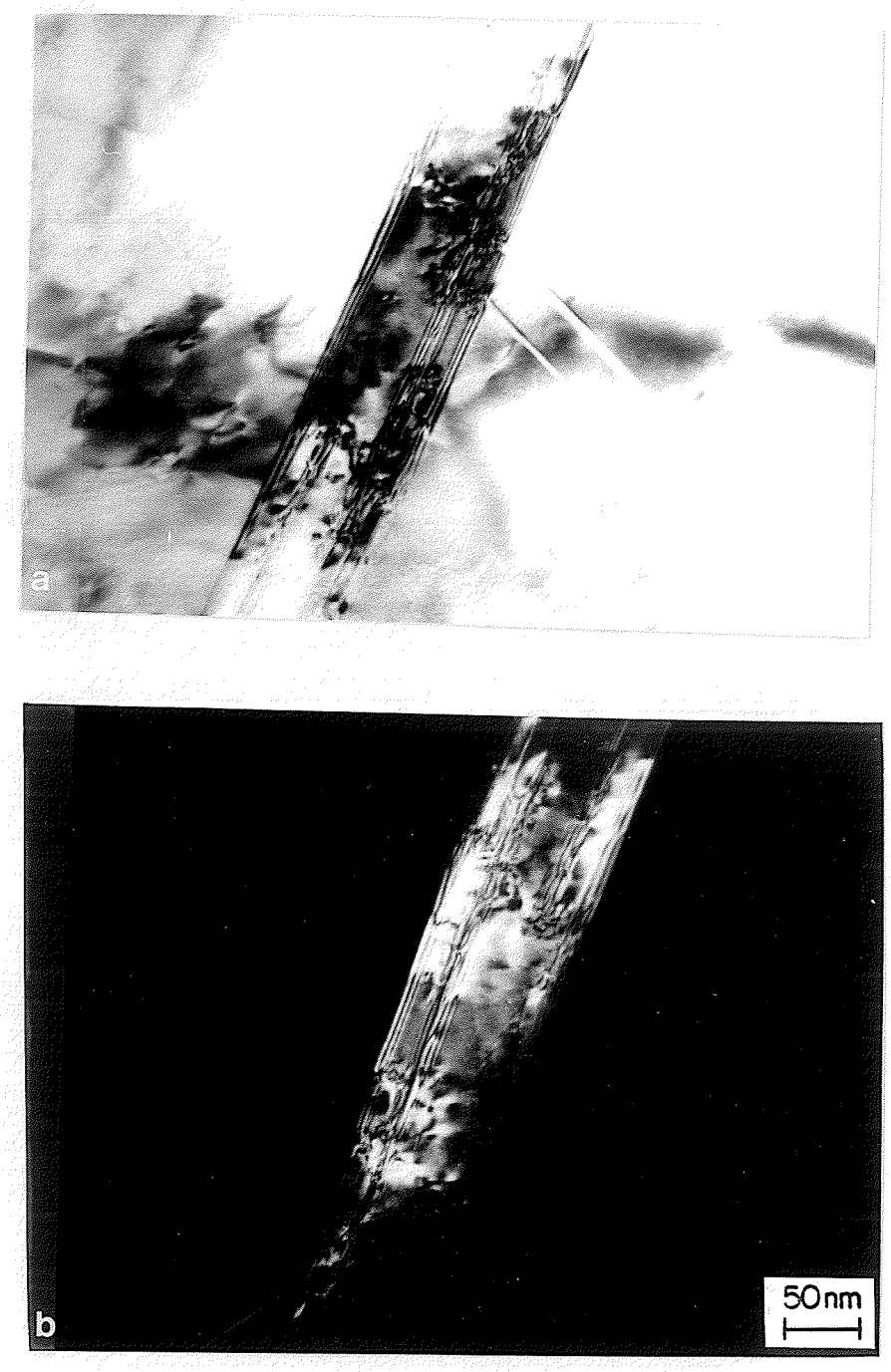

Fig.37 (a) BF and (b) CDF images of microtwins in a specimen of the Ni-2at%Ge alloy 2% deformed.

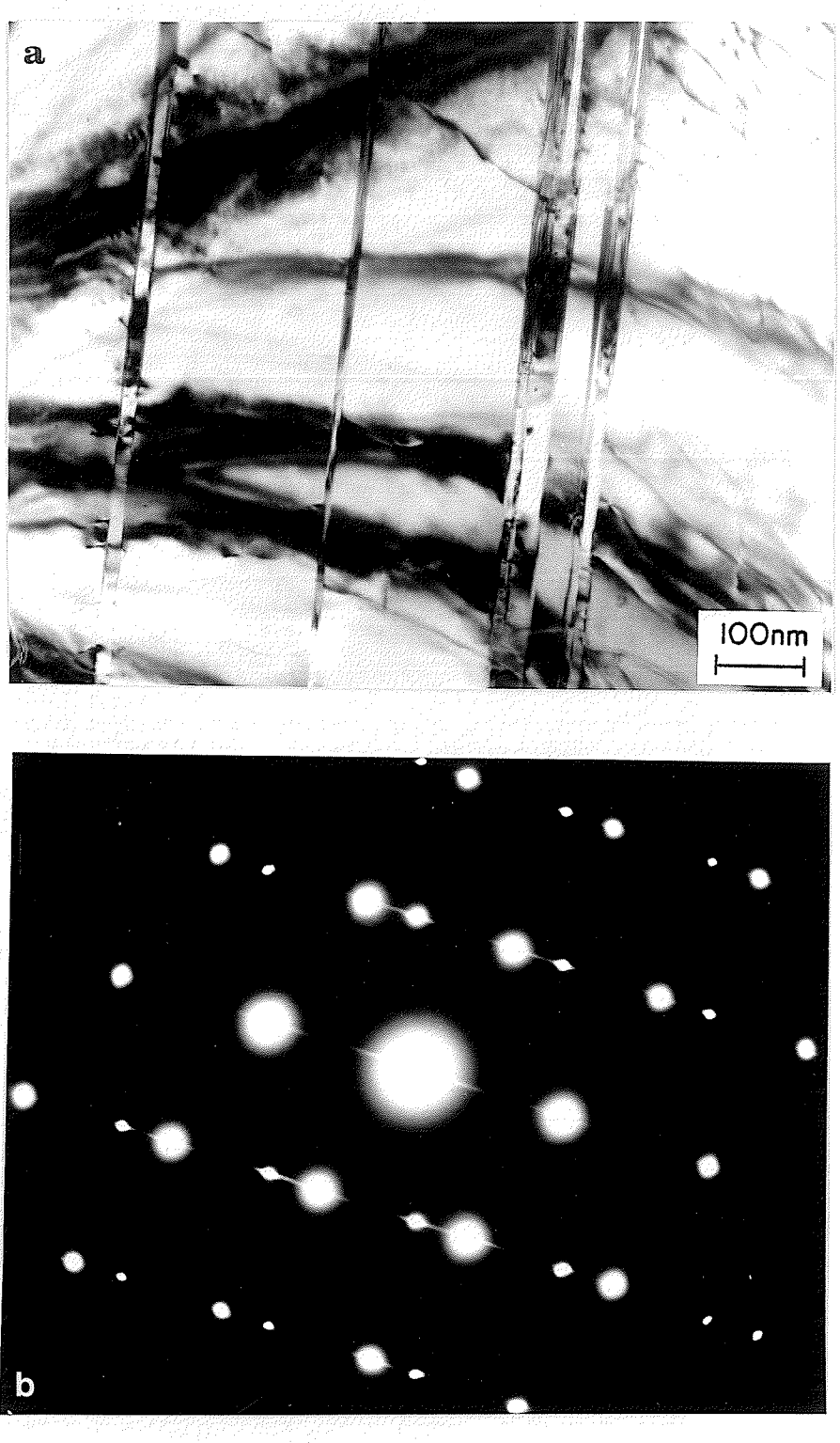

Fig.38 (a) BF image of a Ni-2at%Ge alloy 2% deformed specimen illustrating the presence of microtwins and (b) SADP of the microtwins shown in (a).

Occasionally in some areas of thin foil samples of dilute alloys, thin plates, with long and straight fringes along their boundaries, were observed. These microplates, an example of which is shown in Fig.35, were very long but their width was very narrow; the latter averaging about 30 nm. The dislocation density in this region was found to be high. Using different operating diffraction vectors, these dislocations were found to belong to different slip systems. This suggests that several slip systems have been simultaneously activated in these regions. The SADP of the microplates, illustrated in Fig.36a, shows the existence of two sets of identical diffraction patterns. Each diffraction pattern was indexed to belong to the [110] zone axis of the matrix and these two sets of diffraction pattern were found to exhibit a twin relationship, as is illustrated in Fig.36b. The twin axis is parallel to the $[1\bar{1}1]$ direction and a simple rotation of 180 degrees about the $[1\bar{1}1]$ twin axis corresponds to a mirror image of the matrix diffraction pattern across the twin axis. For example, the mirror image of $(\bar{1}11)$ diffraction spots which is labeled as $(\bar{1}11)_t$ in the figure, can be obtained by rotating the spot 180 degrees around the twin axis. Using the diffraction spots of the matrix ($\mathbf{g}_m$) and twin ($\mathbf{g}_t$) as operating reflections, the contrast of the twins are observed to be exactly opposite each other, as seen in Fig.37. This is known to be the unique contrast characteristic of twins. Therefore, it is concluded that these plates are microtwins.

In some areas of these thin foils, when several long and narrow microtwins were present simultaneously, the diffraction spots corresponding to these areas were observed to be streaked along the <111> direction. This situation is illustrated in Fig.38. At high magnification it was further observed that in some localized regions of these microtwins the twin boundary fringes were not straight but were wavy and seem to have been interfered with by some unknown processes, as seen at A in Fig.39. When these foil samples were tilted around the axis parallel to the intersection of the twin boundary, the projected area of

the twin boundary became wider. Dislocations lying on the twin boundary were observed and the contrast of the boundary fringes were observed to be different in different areas. Some areas of the boundary appeared darker, whereas others appeared lighter, and in some areas the fringes were not present at all as shown in Fig.40. This type of contrast effect has been studied thoroughly by Gevers [81] and Humble [82]. They have pointed out that this effect is caused by the overlapping of closely spaced stacking faults present on those {111} planes which are near the twin plane.

It is known that two types of stacking faults occur in fcc crystals, intrinsic and extrinsic. In the extrinsic fault, as shown in Fig.41, there is an extra layer of atoms, e.g. A, inserted between planes B and C. The original stacking sequence, ABCABC along the <111> direction of the Ni lattice, will be therefore changed into an ABACABC stacking sequence. Thus, a small piece of twin involving 5 layers of atoms (BACAB) is induced. A stacking fault can also be formed by removing one plane of atoms. By this intrinsic manner, the original ABCABC stacking sequence along the <111> direction is changed into the one of ABABCABC, if plane C were to be removed. In this way, a small piece of hexagonal crystal with an ABAB stacking sequence forms within the fcc lattice. Therefore, whenever a stacking fault is present, regardless of whether it is an intrinsic or extrinsic type, a thin piece of crystal with an atomic stacking sequence different from that of the matrix is introduced in the matrix. According to the kinematical theory of electron diffraction, the intensity distribution of reciprocal lattice points is significantly influenced by the geometrical nature of the radiated crystal. The general rule is that the intensity is always extended along a direction parallel to the shortest dimension of the crystal. When small pieces of two dimensional crystals such as stacking faults are present, the shortest direction is normal to the fault plane. In a fcc crystal, this direction is <111>. When the thin foil sample is tilted to an orientation in which the incident beam is exactly parallel to the [110] direction of the radiated area (Fig.42), it is seen that the $[1\bar{1}1]$ direction is parallel to

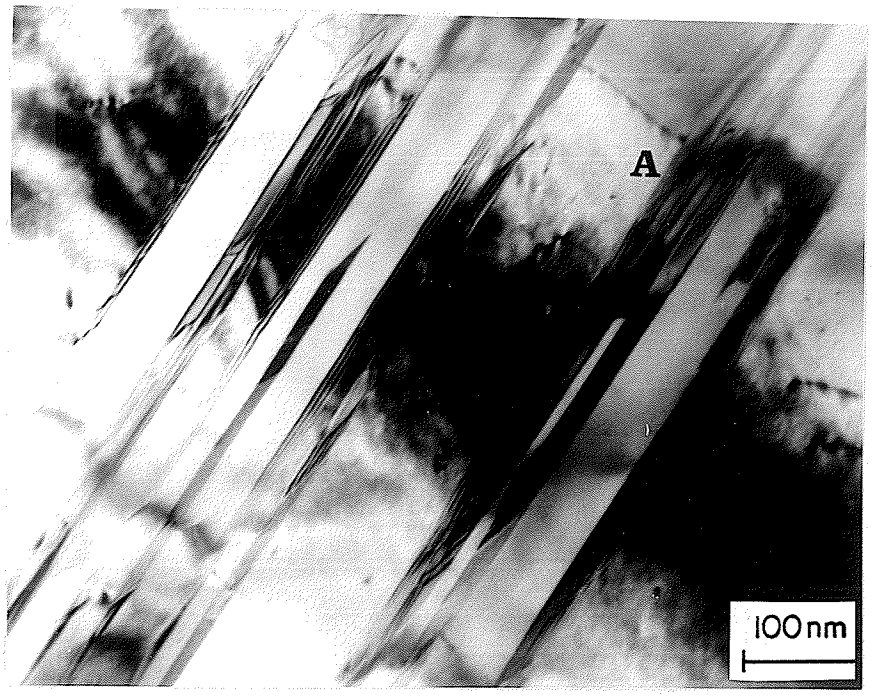

Fig.39 BF image of a 2% deformed Ni-2at% Ge alloy specimen illustrating the presence of wave fringes along twin boundaries.

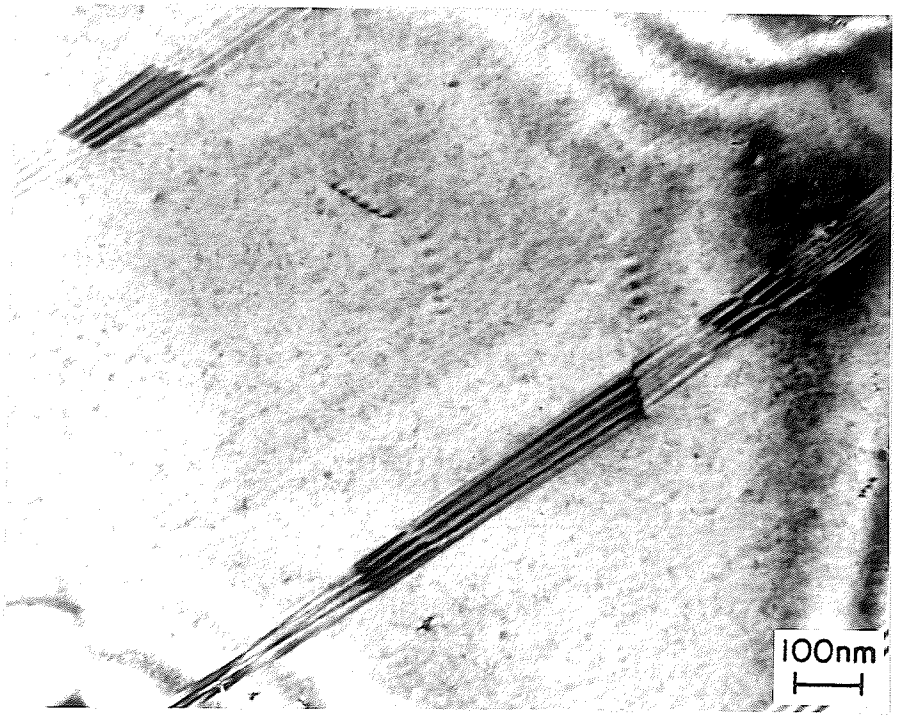

Fig.40 Contrast of stacking fault in a Ni-2at%Ge alloy 2% deformed.

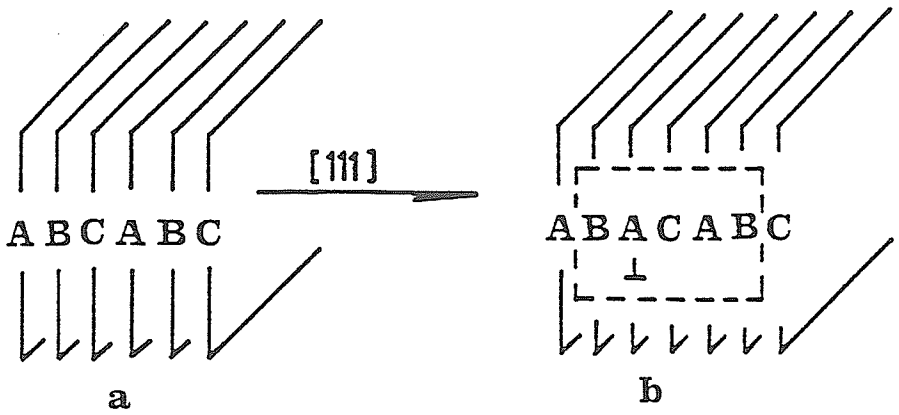

Fig.41 Schematic diagrams illustrating (a) normal stacking sequence and (b) the change in stacking sequence due to the introduction of an extrinsic stacking fault.

the (110) section of the reciprocal lattice. The intensity distribution along the $[1\bar{1}1]$ direction gives rise to traces passing through reciprocal lattice spots. Thereby streaks are formed. When the number of stacking faults is sufficient, the intensity of the streaks would be strong enough to be observed as shown in Fig.38. Correspondingly, the wavy twin boundary fringes seen in Fig.39 are caused by these two dimensional lattice defects.

The twinning in Ni-2at%Ge solid solution after 2% deformation is found to be in its initial stages. In some cases, some microtwins were observed to be composed of several smaller twins. An example is shown in Fig.43. Zig-zag interfaces between these small thin twins were observed as seen in Fig.44. The twinning process is known to require a/6<112> type partial dislocations to move on the twin planes. When a partial dislocation meets with some obstacles and stops moving, it becomes a boundary between a twinned and an untwinned regions. If several partial dislocations on a series of adjacent slip planes are blocked in the same area, zig-zag interfaces are formed. In the twinning region, dislocations of the secondary slip system were also frequently observed. These locally activated slip systems contribute to the formation of the lamellar structure of slip band in front of twin boundaries as observed at A in Fig.45.

In summary, the microstructural characteristics of the deformed dilute Ni-Ge solid solutions are as follows.

1. The dislocation configuration displays a three dimensional network which is quite similar to the one found in pure nickel, a typical wavy material.

2. Microtwins are frequently present in areas where more than one slip system has been activated and the density of dislocations is high.

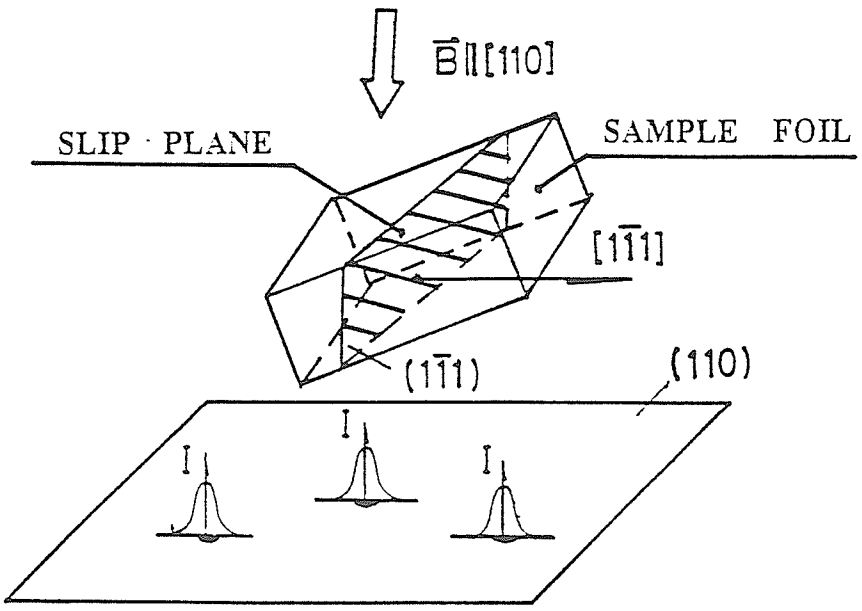

Fig.42 Schematic diagram illustrating sample orientation with respect to the incident beam and the formation of streaks along [111] direction.

Fig.43 Microtwins in a Ni-2at%Ge specimen 2% deformed.

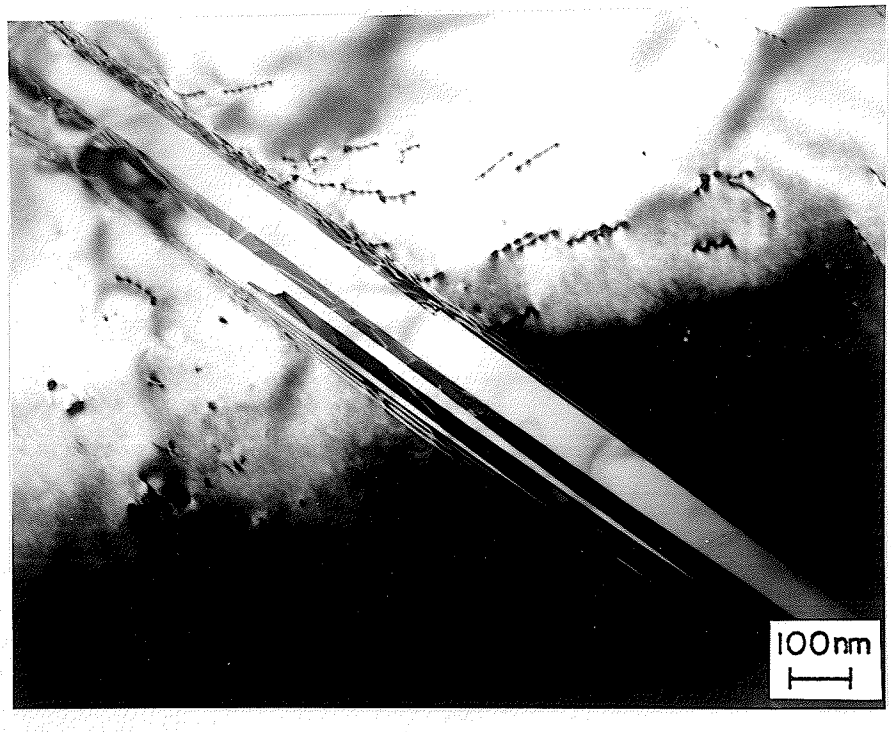

Fig.44 Microtwins in a Ni-2at%Ge specimen 2% deformed.

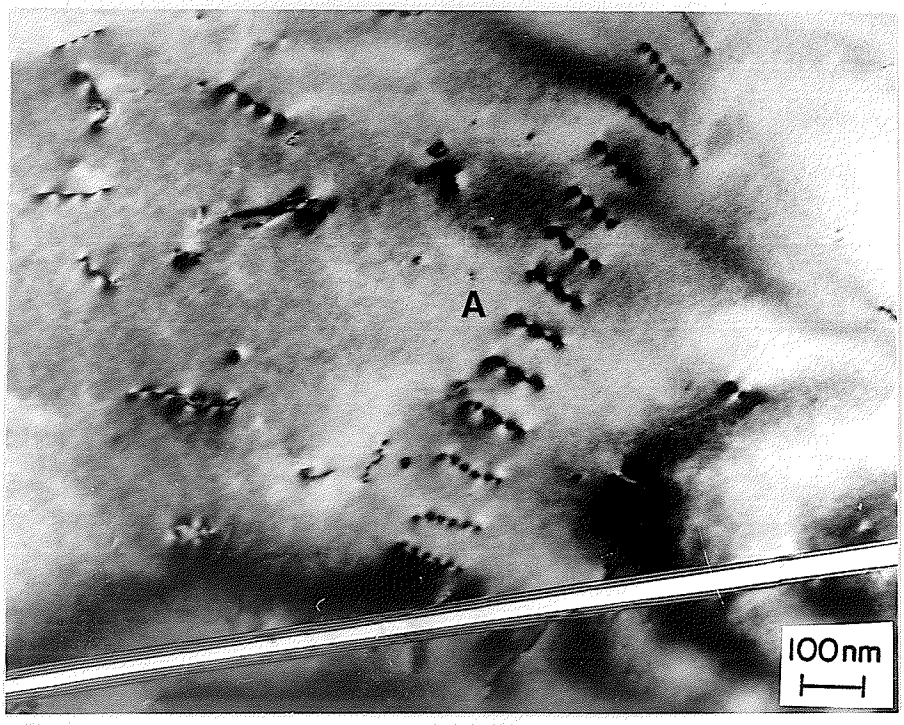

Fig.45 TEM micrograph illustrating the existence of secondary slip system (A) in front of a twin boundary.

3. After 2% deformation, the width of these twins is observed to be very small. A considerable number of two dimensional faults are observed on (111) planes which are adjacent to the twin planes. Therefore, twinning is still in its initial stage.

4.5.2. Microstructural Characteristics of Concentrated and Supersaturated Ni-Ge Solid Solution 2% Deformed

A. Microstructural Features of Ni-7.82at%Ge and Ni-9.75at%Ge Solid Solutions 2% Deformed

The dislocation substructure of concentrated Ni-Ge solid solutions (i.e. 4-10 at%Ge) after 2% deformation was observed to be totally different from the one observed in dilute solid solutions. The dislocation configuration in this case was a heterogeneous in nature. A large number of dislocations were observed to be concentrated in a limited area of active slip planes, and relatively few dislocations were observed outside the pile-ups. Fig.46 illustrates an example of typical dislocation structures observed in the concentrated Ni-Ge solid solutions. Usually, on a single slip plane several hundreds of dislocations were found to be accumulated and arranged in dense pile-ups. Fig.47 is another example of such a dislocation arrangement and the average distance between the two adjacent dislocations is about 10 nm. As this type of dislocation configuration is a kind of long range periodical arrangement, satellites in SADP due to the diffuse scattering effect were observed around main diffraction spots (Fig.48). The crystallographic direction linking the satellite (1) and main diffraction spot, (222), was normal to the pile-up direction of the dislocations, and the spacing between the satellite spot and the diffraction spot, Δg, had a

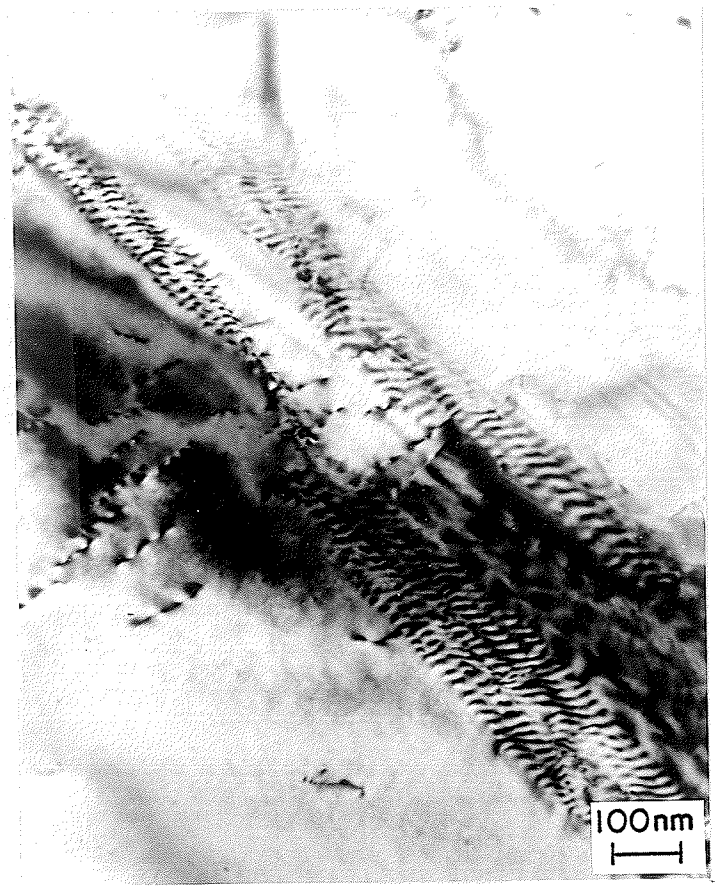

Fig.46 Planar slip type dislocation substructure in the specimen of the Ni-9.8at%Ge alloy.

Fig.47 TEM micrograph of a Ni-7.8at%Ge alloy specimen.

reciprocal relationship with the average distance between the dislocations d_D, i.e.,

$$\Delta g = 1 / d_D \tag{84}$$

Since the intensity of the satellite spot can be considered to be the result of diffraction by lattice planes with interplanar spacing equal to the average distance between the neighboring dislocations, the average inter-dislocation distance can be estimated from the diffraction pattern as well. The corresponding relationship can be expressed by,

$$d_D = L \lambda / R \tag{85}$$

where R is the spacing between the satellite and the main diffraction spot, L is the camera length of the TEM and λ is the wavelength of the incident electron beam. In Fig.48, the values of L = 1200 mm and λ = 0.0025 nm, and the value of R was about 0.3 mm. Therefore, the average spacing between the two adjacent dislocations was about 10 nm, which is identical to the value obtained by the direct measurement on the TEM micrograph shown in Fig.47.

In Fig.48, another extra satellite, spot 2, is believed to be related to the slip plane itself. Fig.49 is a schematic diagram showing the mechanism of formation of satellite spot "2". The diffraction condition in Fig.49 was the same as in Fig.48. Basically, this is a two beam condition, i.e. the intensities of both the transmitted and the (111) diffraction beams are the strongest. However, the (222) diffraction spot is not far from the Ewald sphere. Due to the existence of the slip plane which is actually a two dimensional lattice defect due to the presence of a large number of dislocations in it, the intensity of each diffraction spot will be distributed along a direction normal to the fault plane. The reason for this is the

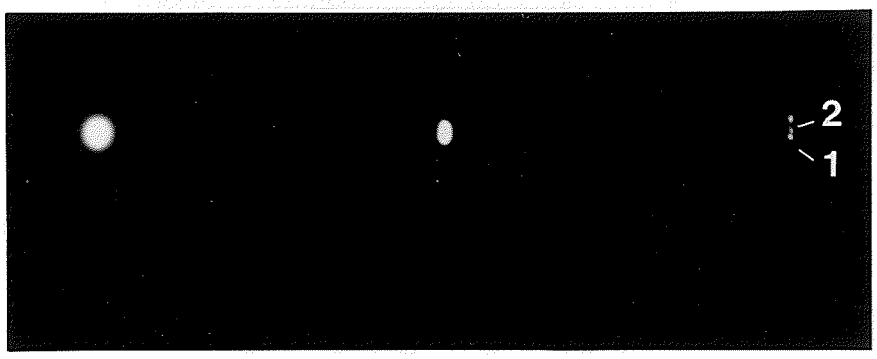

Fig.48 SADP of the area shown in Fig.47.

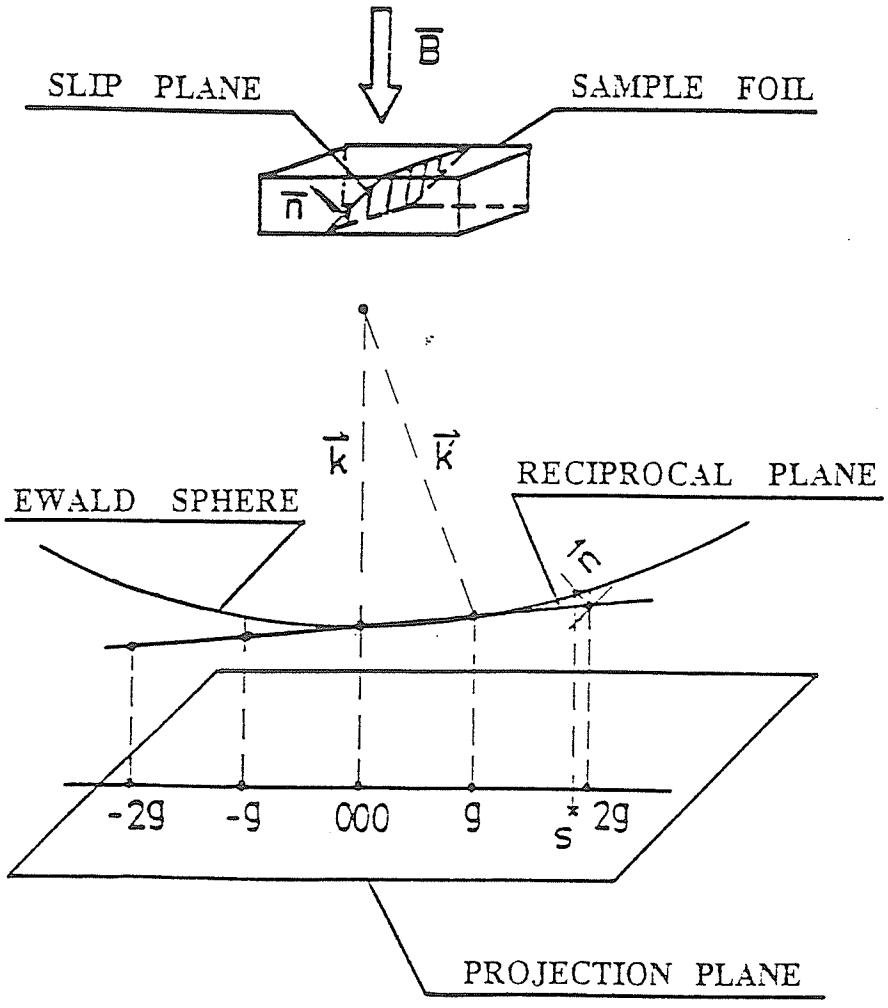

Fig.49 Schematic diagram illustrating the formation of extra satellite spot induced by a single slip plane.

same as that for the formation of streaks in the SADP due to the presence of stacking faults on the {111} twin plane. When the elongated reciprocal spike touches the Ewald sphere, the diffraction condition is satisfied and a satellite spot appears in the SADP. A similar effect has been reported by Amelinckx et al. In their case, the satellite effect was caused by a single stacking fault on a {111} plane [83].

B. Microstructural Features in Ni-4.87at%Ge alloy 2% Deformed

The microstructural features in the Ni-4.87at%Ge alloy 2% deformed were observed to have a morphology that seems to be a mixture of those observed in the Ni-2at%Ge and Ni-7.87at%Ge alloys. Very narrow microtwins with an average width of about 50 nm were observed (Fig.50a). The corresponding SADP of these microtwins is shown in Fig.50b. The frequency of their observation, however, was less than that found in the dilute solid solutions. In most areas that were examined, the dislocations were observed to have a "network" type of distribution (Fig.51a). However, in some areas, the dislocations were observed to be straight and arranged in a somewhat planar slip manner (Fig.51b)

C. Microstructural Features in Ni-11.87at%Ge and Ni-14.56at%Ge Alloys 2% deformed

The examination of selected area diffraction patterns from several thin foil samples of the as-quenched Ni-11.98at%Ge and Ni-14.56at%Ge alloys suggested them to be in a supersaturated state with a single phase fcc crystal structure. This is consistent with the results obtained by the x-ray diffraction investigations. Generally, the dislocation

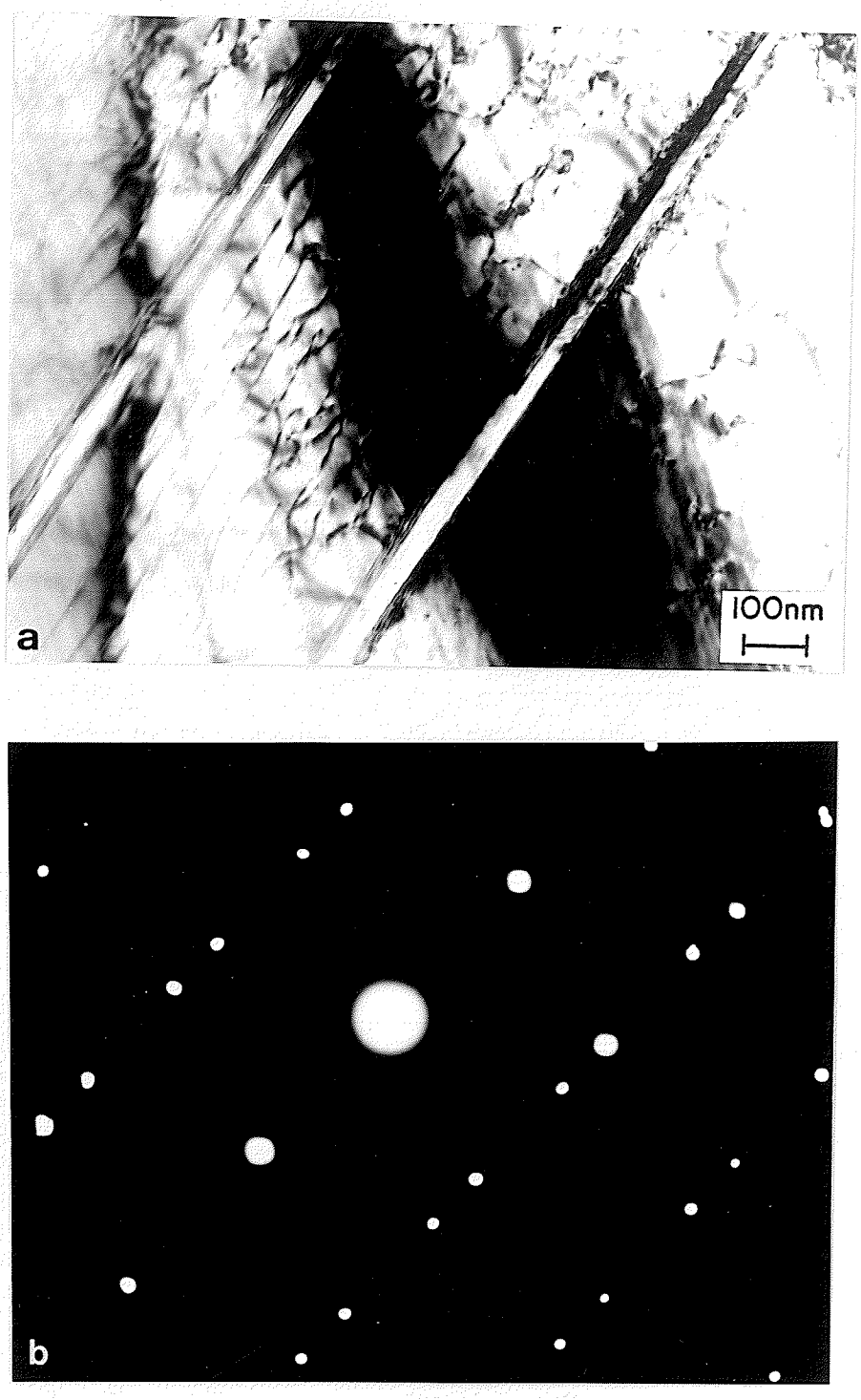

Fig.50 (a) TEM micrograph of microtwins in a Ni-4.87at%Ge alloy after2% deformation and (b) SADP of area (a).

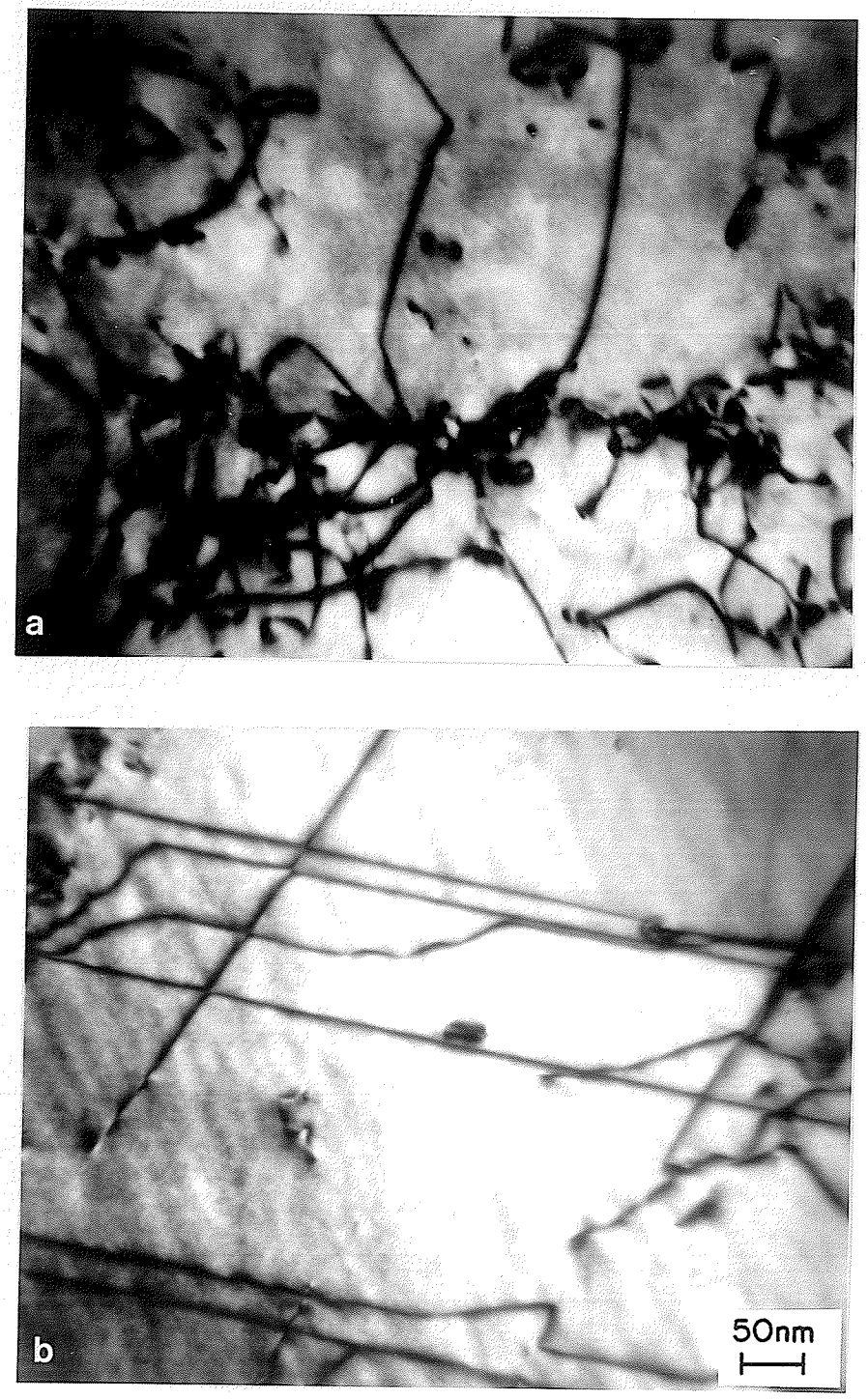

Fig.51 TEM micrograph of (a) three-dimensional and (b) planar-slip type dislocation substructures in a Ni-4.87at%Ge alloy after 2% deformation.

substructure of these two slightly deformed alloys was very similar to the one observed in the other two concentrated solid solutions, viz., Ni-7.82at%Ge and Ni-9.75at%Ge. A planar slip type dislocation configuration was the dominant feature. Fig.52 illustrates this kind of dislocation distribution observed in these two alloys after 2% deformation. In Ni-11.98at%Ge alloy, some dislocations arranged in pairs were also frequently observed. The spacing between the dislocations was usually about 25 nm. In order to find out whether they are dislocation pairs, which usually occur in deformed alloys with ordered precipitates in them and in ordered alloys, or dipoles, the variation in spacing between the dislocation pairs with the operation of a set of $\pm\mathbf{g}$ vector was investigated. The spacing between the dislocations changed significantly when the diffraction vector was reversed as illustrated by the dislocation pair marked "A" in Fig 53. Therefore, in accordance with the criteria proposed by Bell et al [84] and Forwood et al [85], these pairs are suggested to be dipoles. In some areas of the thin foil samples dislocations were observed to appear as multipoles. An example of this is shown in Fig.54. It is interesting to note that even the arrangement of these multipoles is also of a similar planar slip nature. In the thin foil samples of Ni-14.56atGe alloy, well developed multipoles were frequently observed, an example of which is illustrated in Fig.55.

From those experimental results, it is seen that the addition of Ge in Ni lattice significantly influences the microhardness as well as the microstructural characteristics of the material. These changes were found to be Ge concentration dependent. In the previous section, based on the analysis of variation in A.A.D. value of Ge atoms in Ni-Ge solid solutions, the concentrated solid solutions were suggested to possess some degree of short range ordering. Therefore, it seems possible that the occurrence of the localized short range ordering is responsible for the microhardness and microstructural changes observed in the concentrated solid solutions. However, additional experimental evidence is required to

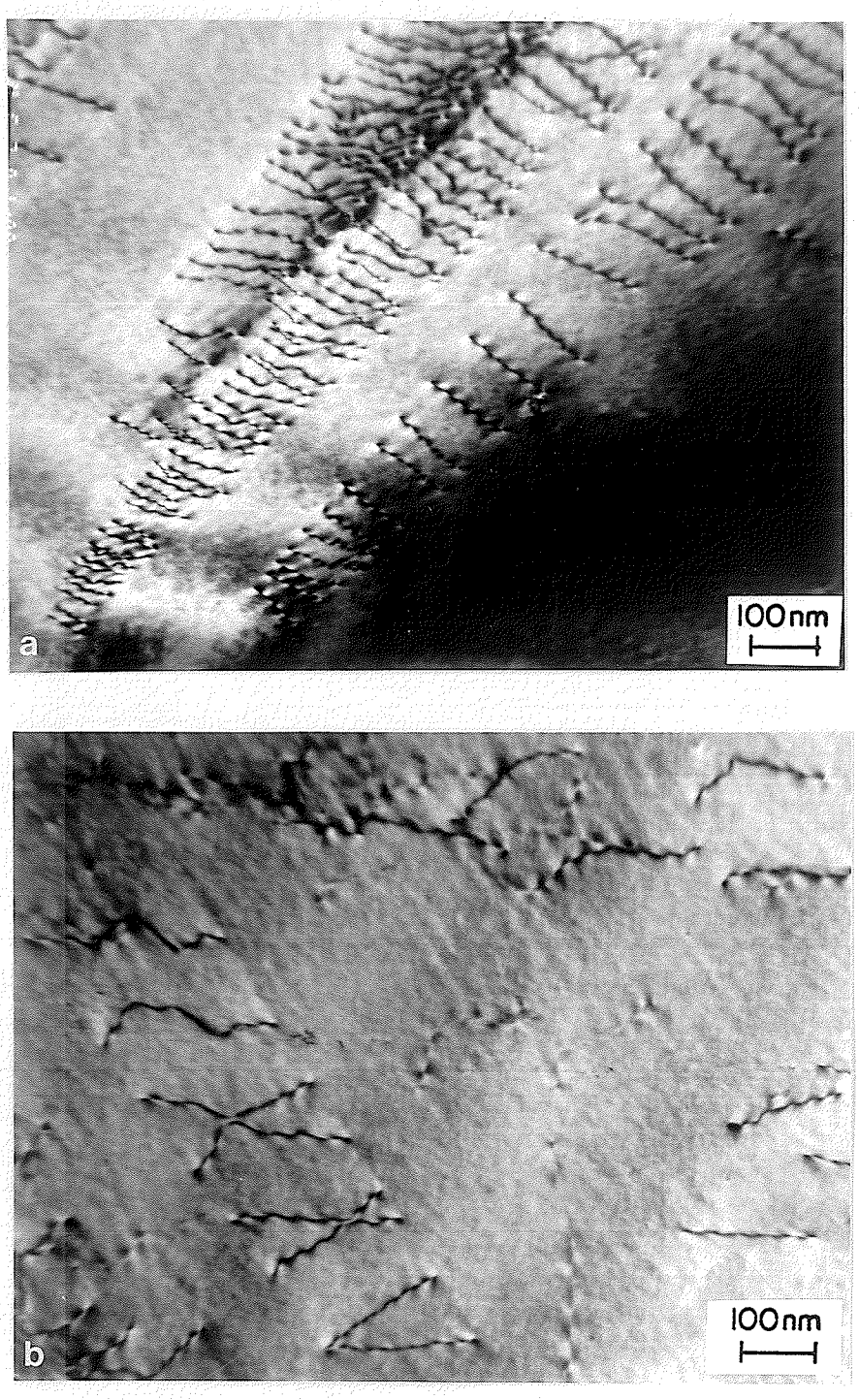

Fig.52 TEM micrograph of planar slip dislocation configuration in (a) Ni-11.98 at% Ge and (b) Ni-14.56 at% Ge specimens.

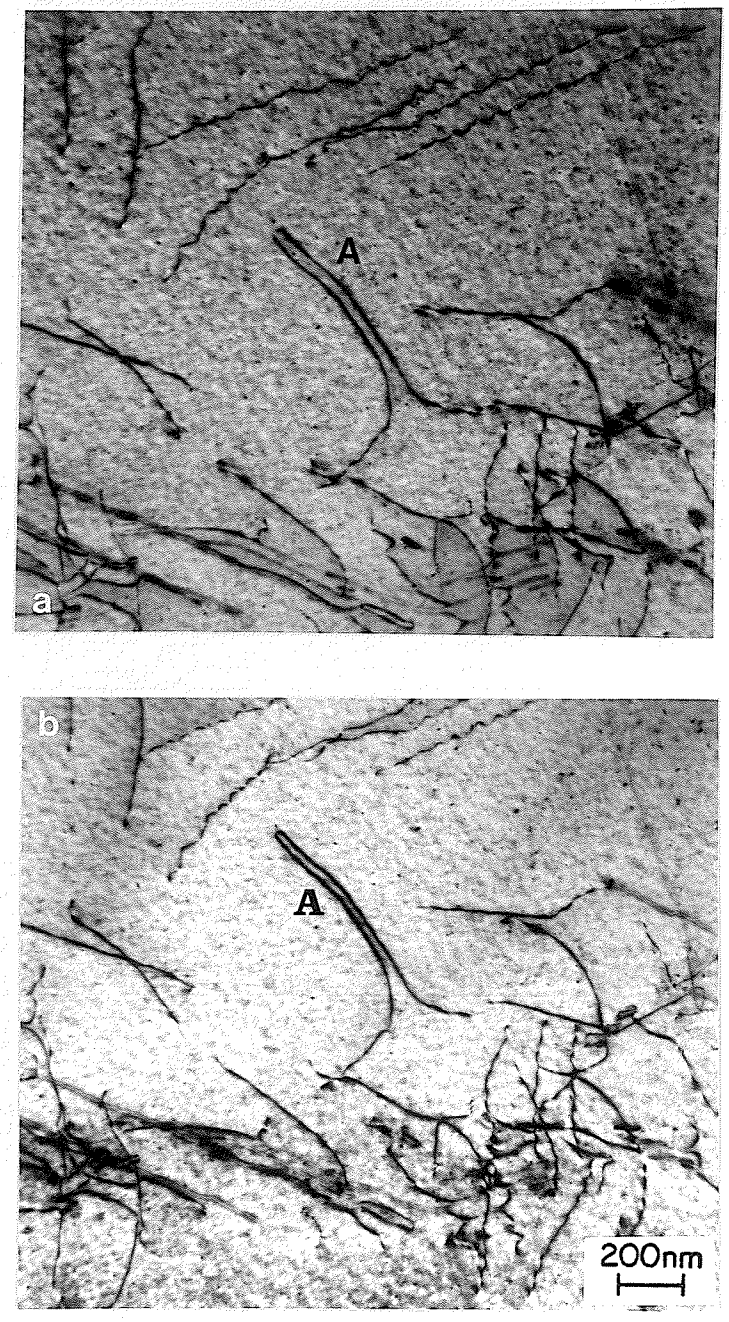

\

Fig.53 TEM micrograph of a Ni-11.98at%Ge alloy specimen after 2% deformation (a) **g**=200 and (b) **g**=$\bar{2}$00.

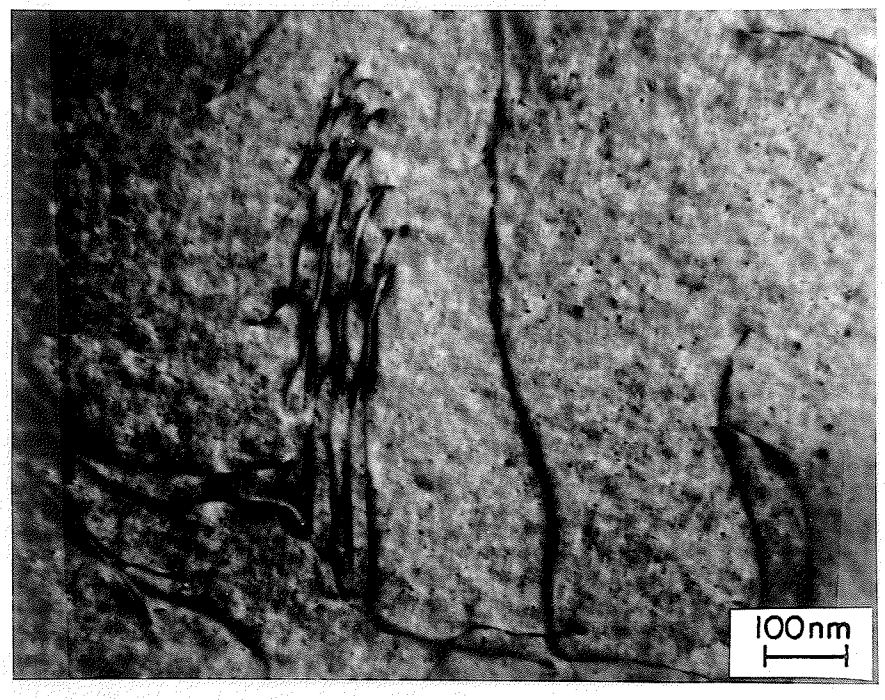

Fig.54 TEM micrograph of a Ni-11.98at%Ge alloy specimen after 2% deformation.

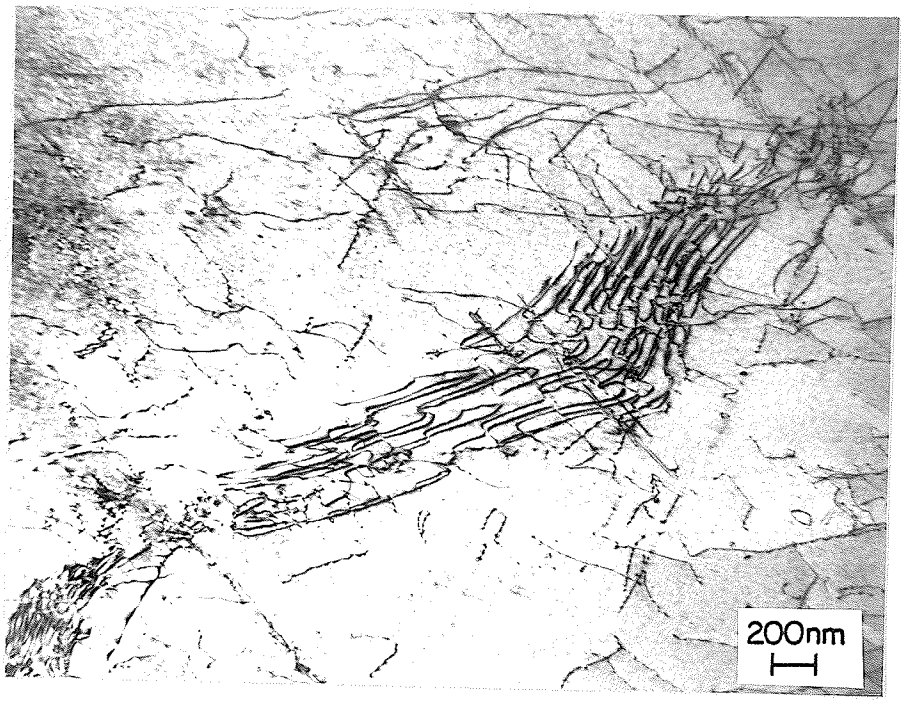

Fig.55 TEM micrograph of a Ni-14.56at%Ge alloy specimen after 2% deformation.

support this suggestion conclusively. Since the dimension of the short range ordered region is likely to be at a scale of ten to hundred nanometers, diffraction techniques using x-ray, electron or other beams seem to be best suited for this study. Based on the facilities at hand, x-ray diffraction investigation of bulk samples and TEM observations of thin foils were carried out for this study, and are presented next.

4.6 X-ray Diffraction Investigation of the Concentrated Solid Solutions

Large grained bulk samples were mounted on the x-ray diffractometer with its (200) planes parallel to the sample holder. A schematic diagram of the experimental arrangement is illustrated in Fig.56. In this configuration, strong and sharp (200) diffraction peaks from the samples containing 4.87at%Ge to 9.71at%Ge were recorded. The intensity profile of these peaks was observed to be asymmetrical in nature. An example of this is illustrated in Fig.57 which was obtained from a sample containing 9.75at%Ge. The intensity on the lower angle side of the (200) peak is seen to be stronger than that observed on the higher angle side. In order to confirm that the the asymmetry in intensity is only related to the composition of the material rather than a systemic error in the diffractometer itself, the intensity profile of (200) reflection of pure nickel was also recorded and carefully compared with that observed from the solid solutions. Sections of the intensity profiles of pure nickel and three other Ni-Ge alloys with different Ge contents are shown in Fig.58. Contrary to the intensity profile of the (200) reflection of pure nickel, the intensity on the lower angle side of the (200) reflections of the Ni-Ge alloys always appears to be stronger than that observed on the higher angle side. The degree of the asymmetry is observed to increase with Ge concentration. Therefore, this diffuse effect is confirmed to be dependent on the Ge concentration.

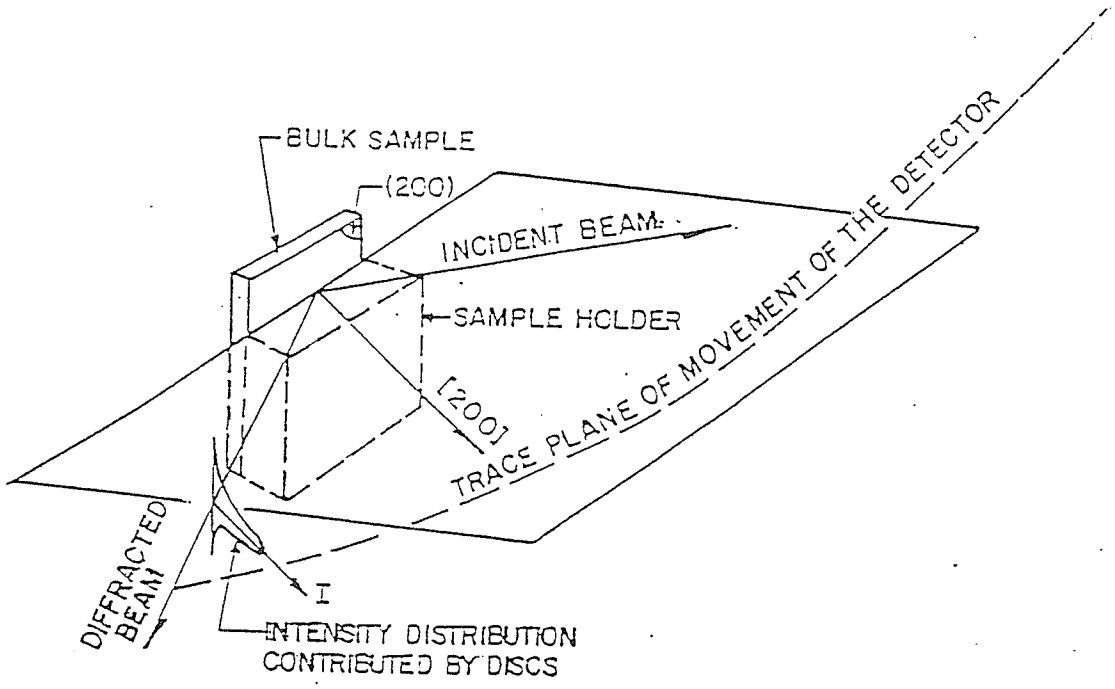

Fig.56. Schematic diagram illustrating the orientation of the specimen with respect to the diffraction plane.

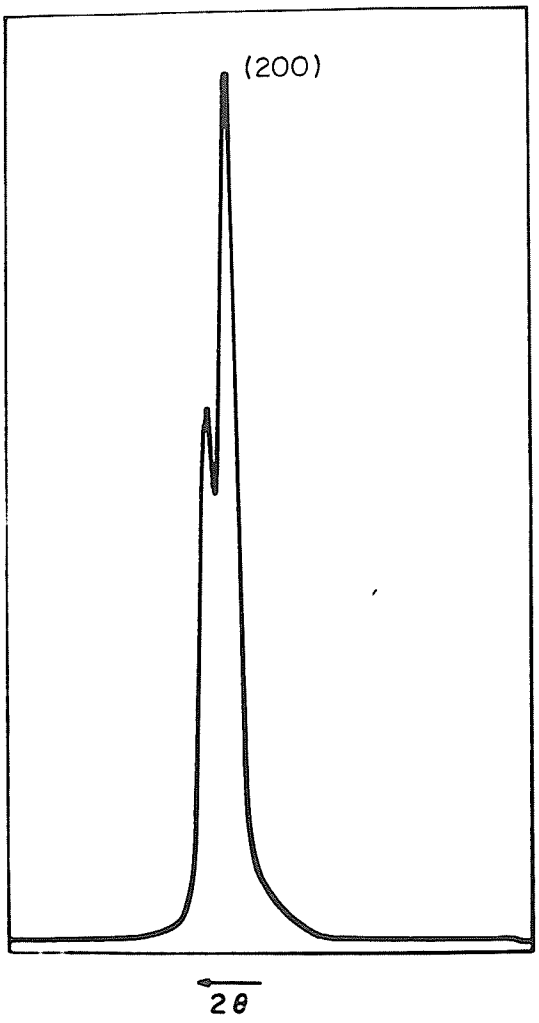

Fig.57 Intensity profile of (200) x-ray diffraction peak in a Ni-9.75at%Ge alloy.

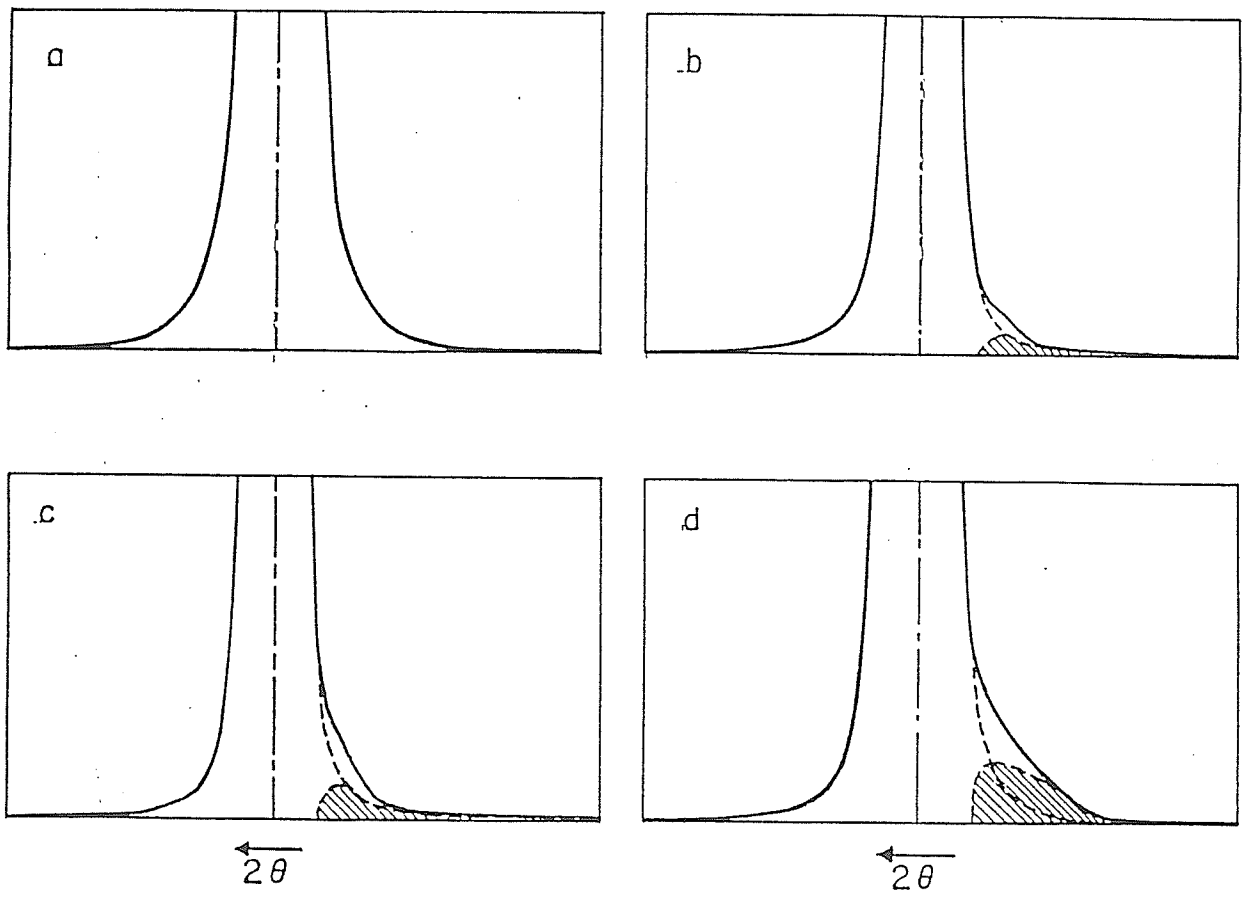

Fig.58 Intensity profile of (200) x-ray diffraction peak in (a) pure nickel and (b) Ni-4.87 at%Ge (c) Ni-7.82at%Ge (d) Ni-9.75at%Ge specimens.

The intensity of the lower angle side of (200) diffraction peak can be considered to be the sum of two contributions. One is due to the contribution of the random Ni-Ge solid solution. This part is expected to be symmetrical on both side of the peak and is represented by a dashed curve in Fig.58. The second could be from regions in the matrix where Ge atoms are non-randomly distributed. The intensity profile of this contribution can be determined by subtracting the intensity value expressed by the dashed curve from the total intensity value, i.e. the original intensity profile. The results are also displayed in Fig.58. Subpeaks on the lower angle side of the main diffraction peak can therefore be identified graphically. These subpeaks are suggested to be the contribution of some specific volume of material with a larger interplanar spacing distributed in the matrix. The interplanar spacing, d_L, corresponding to these volumes can be determined using the Bragg relationship and are listed in Table 11.

Since the x-ray diffractograms have shown the solid solutions to be single phase with a fcc crystal structure, these regions in the solid solution are suggested to have a fcc structures also. The interplanar spacing of (200) planes in these regions, d_L, and therefore the lattice parameter, a_L, can be determined. These calculated values and the corresponding lattice misfit between the region and the matrix are also listed in Table 11. Since the variation in the lattice parameter, a_M, of the solid solutions with Ge concentration has already been determined, the average composition of the regions with a non-random distribution of Ge, $c_{Ge\text{-}L}$ can be estimated. The results, also listed in Table 11, show that these regions are actually rich in germanium and the variation in germanium concentration in these regions increases with Ge content. However, the average concentration of Ge in these regions is seen to be much lower than that in Ni-saturated Ni_3Ge (22.5at%Ge).

The bulk samples were also scanned on the x-ray diffractometer with 2θ values ranging from 24° to 26° to determine the presence of the (100) superlattice peak of Ni_3Ge

TABLE 11. Interplanar spacing of (200) planes of Ni-Ge solid solutions with different germanium concentration

c_{Ge} (at%)	4.87	7.82	9.75
d_M (nm)	0.1767	0.1770	0.1771
d_L (nm)	0.1777	0.1778	0.1781
a_L (nm)	0.3554	0.3556	0.3562
a_M (nm)	0.3534	0.3540	0.3544
$c_{Ge\text{-}L}$ (at%)	13.8	14.4	14.5
δ (%)	0.6	0.5	0.6

phase. No superlattice peak could be observed. It is known that in a binary system, the intensity of the (100) superlattice peak is determined by the difference between the atomic scattering factors of the solute and the solvent elements, as well as by the volume fraction of the ordered phase. Since the values of the atomic scattering factor of Ni and Ge are very close and the number of Ge-rich regions is so small that even their (200) diffraction peak is very weak, the absence of the superlattice peak in the diffractogram may not necessarily indicate that the Ge-rich regions are completely disordered. However, since their Ge concentration is less than what is needed to produce a totally ordered structure (i.e. 22.5at%Ge), they cannot be considered to be totally ordered either. Since the diffuse scattering effect due to the presence of Ge-rich region has already been estimated by this x-ray investigation, a TEM study was initiated to find out if there are any contrast effects which can be attributed to the presence of Ge-rich regions.

4.7 TEM study of the Ge-Rich Zones in Concentrated Solid Solutions

Thin foil samples of solution treated and quenched Ni-Ge alloys with Ge concentration from 0.92 to 11.98at% were examined in the TEM. The results of the examination of selected area diffraction patterns from these specimens suggest that these alloys are all single phase with a fcc crystal structure. This is consistent with the results of the x-ray diffraction studies described in the previous sections. However, contrast effects started to be observed in the thin foil samples of Ni-7.87at%Ge alloy and became more clearly discernible in alloys with higher Ge concentration. These contrast effects can be attributed to the presence of Ge-rich regions.

In thin foil samples of Ni-7.87at%Ge alloy, black needle like contrast effects were observed in the areas close to the extinction contours. This feature is illustrated in Fig.59. The average length of the needles was found to be about 20 nm and they were observed to be distributed densely and somewhat regularly in the matrix. At higher magnifications and in a central dark-field image, using the $(1\bar{1}1)$ reflection, the contrast appeared sharper and contained fine fringes. An example of this is illustrated in Fig.60. The presence of this contrast effect suggests that the solid solution is heterogeneous on a nanometer scale. It seems to confirm the experimental results obtained by the x-ray diffraction studies which have suggested that coherent Ge-rich regions are present in the solid solutions when the Ge concentration exceeds 5.0at%Ge. Since the Ge concentration in Ge-rich regions is found to be about ten percent higher than that present in the matrix (Table 11), the structure factor and hence the extinction distance of these Ge-rich regions is expected to be different than that of the matrix. This difference is suggested to cause the observed contrast effects which are often observed in solid solutions within which solute rich GP zones or small ordered domains exist [86].

When the sample was tilted to a appropriate orientation and examined at higher magnification, the needle like regions were found to be rods, and two sets of dark and somewhat regularly aligned Ge-rich regions were observed. This feature is shown in Fig.61a where these two sets of dark regions are labeled as A and B respectively. The selected area electron diffraction pattern corresponding to Fig.61a is shown in Fig.61b. The indexing of this SADP suggests that the $[\bar{1}23]$ direction of the observed area is nearly parallel to the incident electron beam. Streaks were observed on $(1\bar{1}1)$ and $(\bar{1}1\bar{1})$ reciprocal spots. The direction of the streaks is indexed to be parallel to $[54\bar{1}]$, which is perpendicular to the $[\bar{1}1\bar{1}]$ direction. The longer side of each A region in Fig.61a, can be indexed to be parallel to the [210] direction. The average value of the length of the longer side is about 20

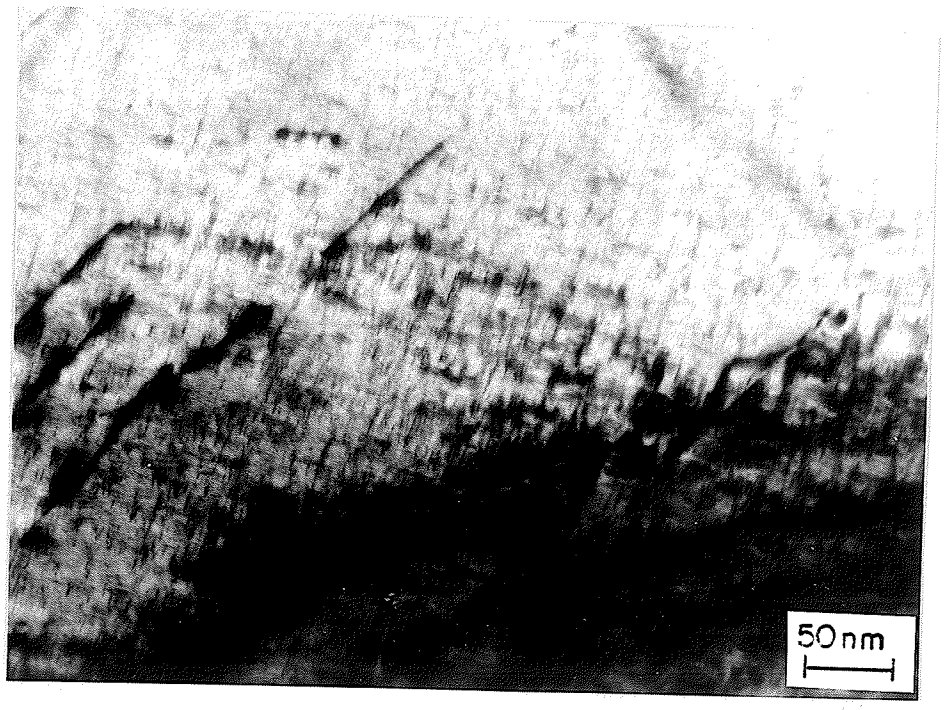

Fig.59 TEM micrograph of a Ni-7.8at%Ge specimen.

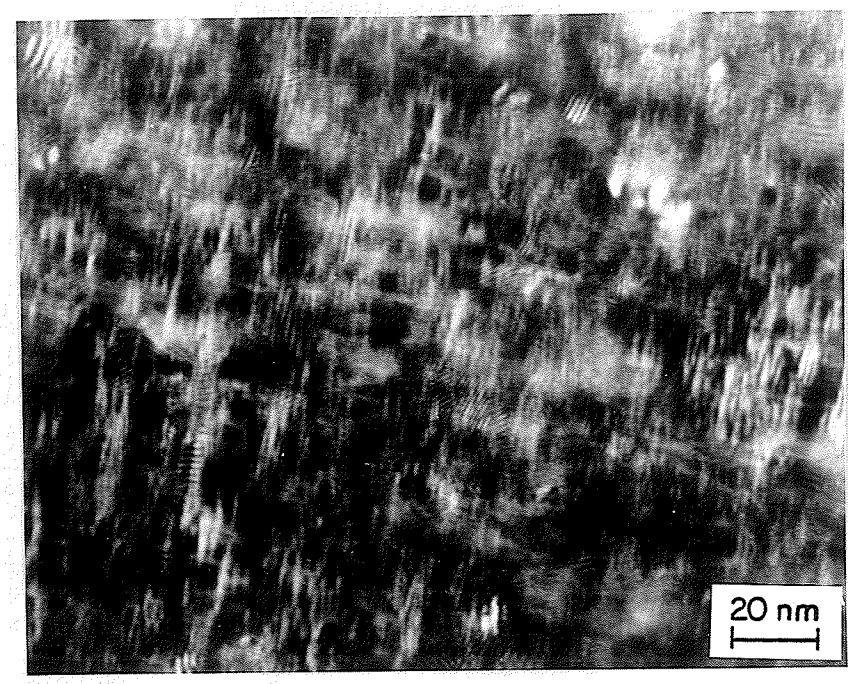

Fig.60 TEM micrograph of small discs in a Ni-7.87at%Ge alloy 2% deformed (CDF image).

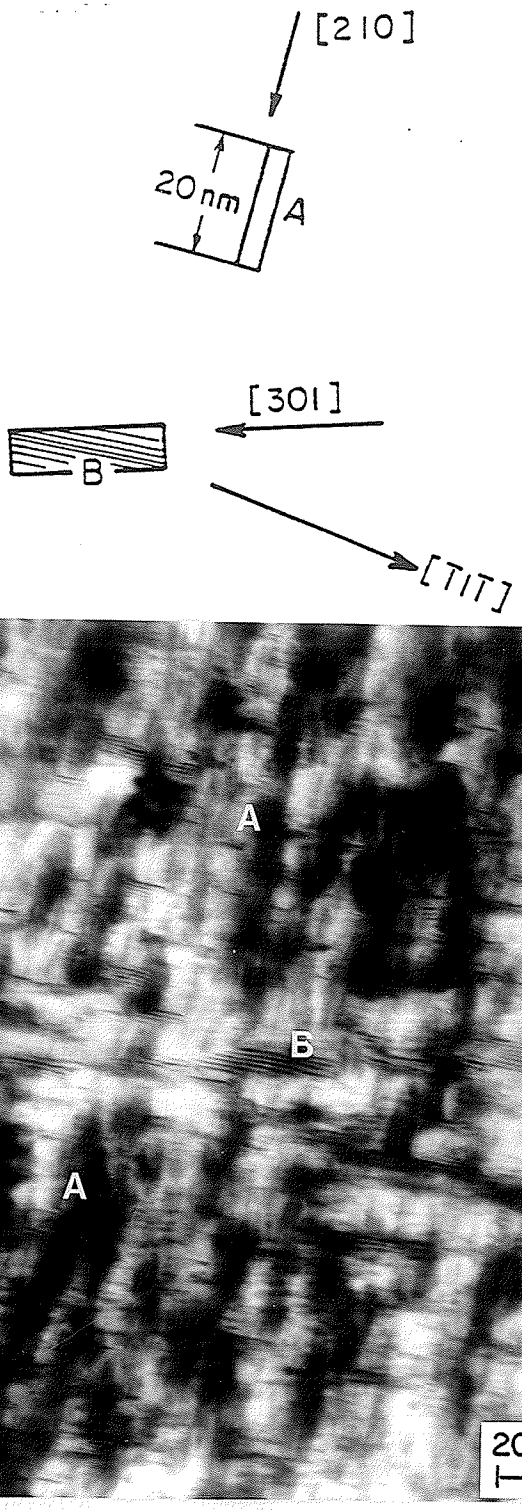

Fig.61a Contrast effect in a Ni-7.87at%Ge alloy specimen, $\bar{g}=1\bar{1}1$.

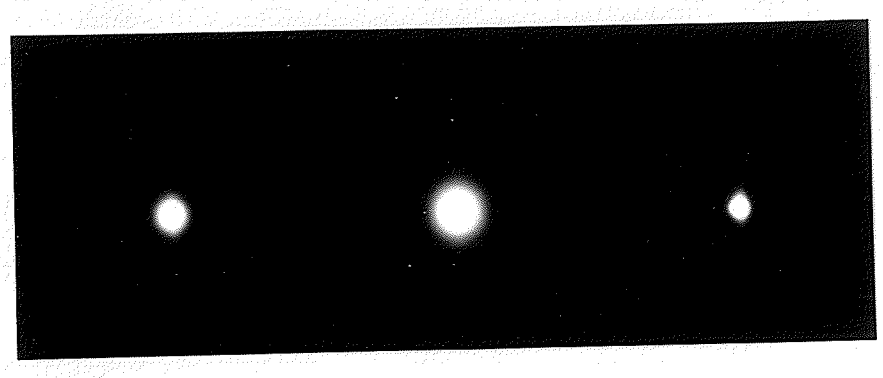

Fig.61b SADP of Fig.61a.

nm. By the same method, the longer side of each B region is indexed and is parallel to the [301] direction. Its average length is about 20 nm. In addition, fine fringes were observed only in B regions and these fine fringes were indexed as parallel to the $[\bar{1}1\bar{1}]$ direction.

It is recognized that nickel is an elastically anisotropic material whose anisotropic factor, A, is reported to be 2.54 [21] which is large. Since the <100> directions are the elastic softening direction of the Ni lattice it seems possible that the Ge-rich regions may choose to cluster on the {100} planes of the matrix. Therefore the strain energy, which is induced by lattice misfit between Ge-rich region and the matrix, may be effectively reduced. In order to determine the validity of the above suggestion and find out the reasons for the observed diffuse scattering effects, a trace analysis study was carried out. Fig.62 is a schematic diagram illustrating orientation of the traces of intersections of (100), (010) and (001) planes with $(\bar{1}23)$ section of reciprocal lattice of the Ni-Ge fcc matrix. It is seen in Fig.61a that the longer side of region A is along the [210] direction and that of region B is along [301] direction. Therefore, by comparing Fig.61a with 62 it can be concluded that the longer side of region A is parallel to the trace of intersection of (001) plane with the $(\bar{1}23)$ section of the reciprocal lattice of the matrix and the longer side of the B region is parallel to the trace of the intersection of (010) with the $(\bar{1}23)$ section of the reciprocal lattice. Therefore, the Ge-rich regions seem to be lying on the {001} plane of the matrix and their {001} plane seems to interface with the {001} plane of the matrix. Since the angle between [001] and $[\bar{1}23]$ directions is about 37°, the orientation of region A is suggested to be inclined 37° with respected to the $(\bar{1}23)$ section of the reciprocal lattice of the matrix. It seems that the shape of the Ge-rich region should look like a thin plate and the normal of the plate should be parallel to the [001] direction of the matrix as schematically shown in Fig.63. From this arrangement, the intersection of the plate with the $(\bar{1}23)$ section of the reciprocal lattice is parallel to the [210] direction and the projection image of the plate along

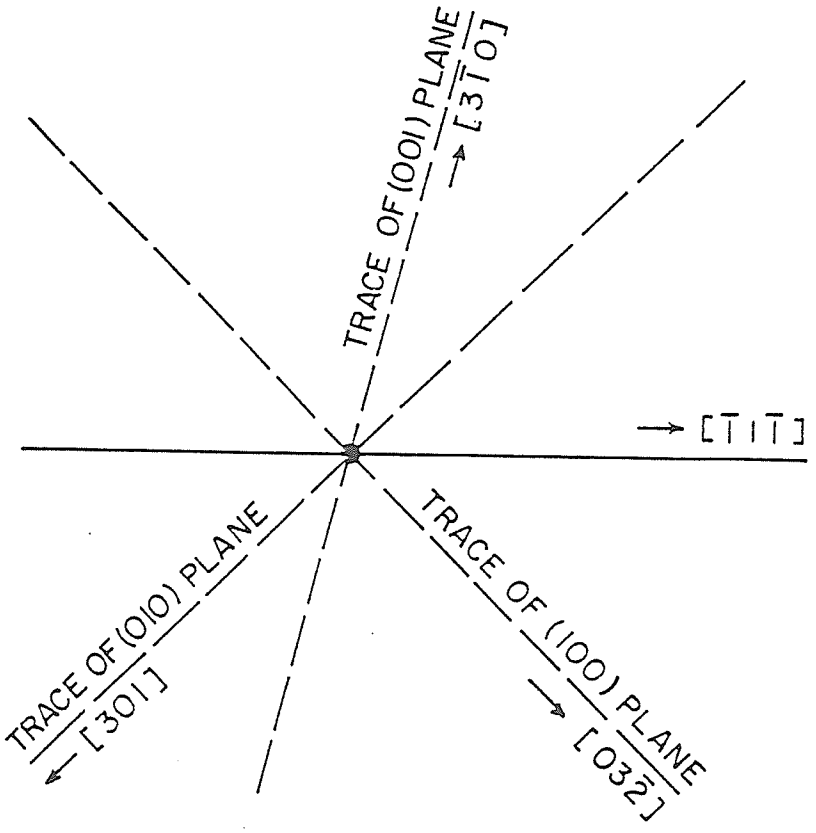

Fig.62 Orientation of (001), (100) and (010) plane trace on the ($\bar{1}23$) section of the reciprocal lattice.

the $[\bar{1}1\bar{1}]$ direction of the matrix appears shorter. Therefore, the projected image of the plate appears to be a rod with its longer side parallel to the [210] direction of the matrix. This analysis is also found to be true in the case of the plates whose projected image was labelled as B Since the longer side of B region is indexed as parallel to the [301] direction, which is the direction of the trace of the (010) plane, the normal to the thin plate is suggested to be parallel to the [010] direction.

The fine fringes observed in the B region are parallel to the $[\bar{1}1\bar{1}]$ direction which is the direction of the trace of the (110) plane on the $(\bar{1}23)$ section of the reciprocal lattice. Since the angle between the [110] direction, which is normal to the (110) plane of the Ge-rich region, and the $[\bar{1}23]$ direction is about 80°, the (110) planes of those Ge-rich regions whose projected image corresponds to the B region are suggested to be inclined at about 10° to the $(\bar{1}23)$ section of the reciprocal lattice. Because the lattice parameter of Ge-rich regions is larger than that of the matrix, the matrix planes are suggested to be displaced in the opposite direction on both sides of the Ge-rich plates. This causes an abrupt change in the phase of the incident and diffracted waves as they encounter these plates. This phase difference leads to the formation of displacement fringes which run parallel to the line of intersection of the projected image of the regions and the $(\bar{1}23)$ section of reciprocal lattice. In this case, fringes are parallel to $[\bar{1}1\bar{1}]$ which is the direction of intersection of the projected (110) and the $(\bar{1}23)$ section of reciprocal lattice. This situation is illustrated schematically in Fig.64. Since the (110) planes are inclined to the $(\bar{1}23)$ section of reciprocal lattice, the real length of b, which is one of the sides of region B, should be corrected by b'/cos(80°), where b' is the projection of B on the $(\bar{1}23)$ section of the reciprocal lattice. Consider B_1 in Fig.61a as an example of region B where the measured values of a and b' are 30 nm and 6 nm, respectively. After the correction, the value of b is about 34 nm. Therefore, by examining from the [110] direction, the real values of a and b

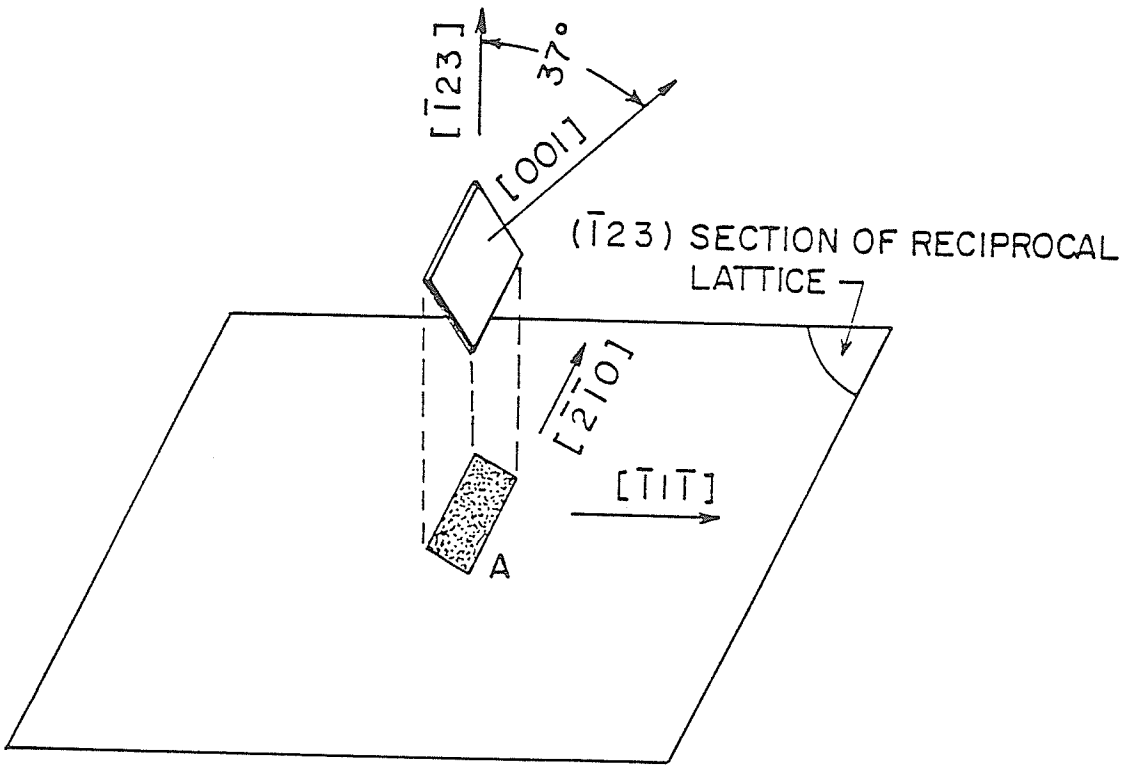

Fig.63. Schematic diagram illustrating the orientation of the Ge-rich region plate with respect to the ($\bar{1}$23) section of the reciprocal lattice.

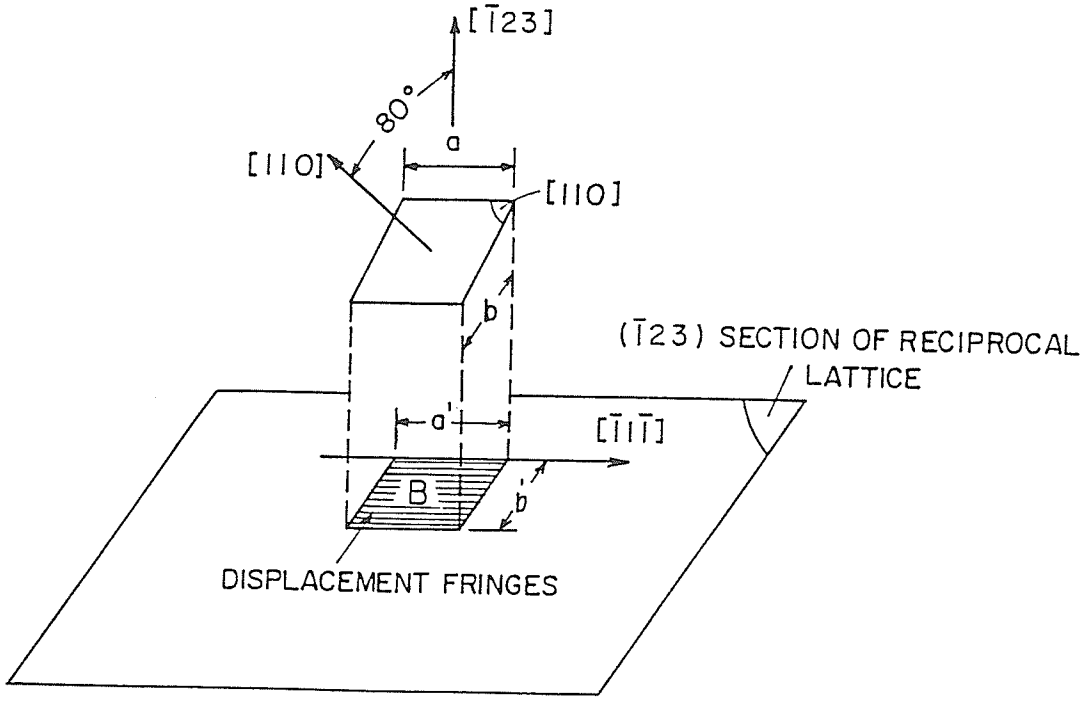

Fig.64. Schematic diagram illustrating the orientation of (110) planes of Ge-rich plate with respect to the ($\bar{1}$23) section of the reciprocal lattice.

of the Ge-rich regions, are of the same order of magnitude, i.e. tens of nanometers.

Since the plates corresponding to region B are thin along the [010] direction, the dimension along the [110] direction of the plates is also expected to be short when it is compared with the dimensions of the plates along the [100] and [001] directions. As predicted by the kinematical theory of electron diffraction [86], the diffraction intensity should extend along both of these two directions. As the [010] direction is inclined to the $(\bar{1}23)$ section of the reciprocal lattice at an angle of about 10°, part of the extended intensity that touches the $(\bar{1}23)$ section of the reciprocal lattice leaves a trace as a streak on the $(\bar{1}23)$ section of the reciprocal lattice along a direction parallel to $[54\bar{1}]$. This is the situation observed in Fig.61b. However, as the [010] direction is inclined to the $(\bar{1}23)$ section of the reciprocal lattice at an angle of about 33°, the length of the intensity distribution projected onto the $(\bar{1}23)$ section of the reciprocal lattice is short. Therefore, a streak could not be observed.

When the thin foil sample was tilted to an orientation such that the [001] direction of the selected area was parallel to the direction of the incident electron beam, two-dimensional and regularly aligned thin plates were observed. These plates, arranged like domains, were observed to align along two <100> directions of the matrix.This situation is shown in Fig.65. The average thickness of the plates measured directly from Fig.65 is about 2~3 nm and the average lengths of the plates along [100] and [010] directions are similar and about 20~30 nm.

Therefore, by examining from two different directions, the real shapes of the Ge-rich regions are suggested to be thin plates. The thickness of the plates is suggested to be about 2~3 nm and the length and the width are about 20~30 nm. The crystallographic

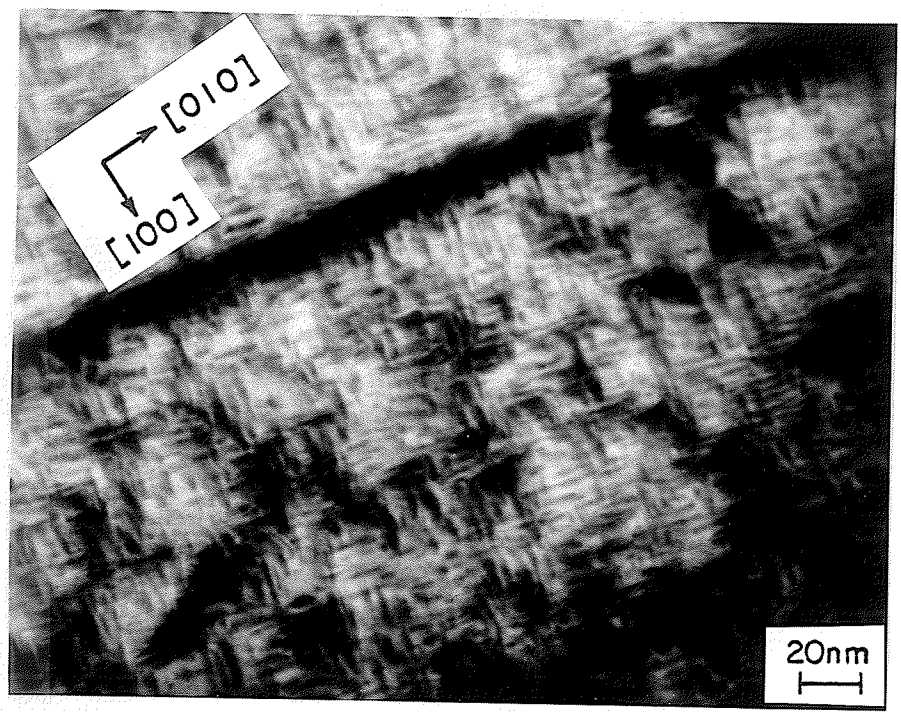

Fig.65 TEM micrograph of a Ni-7.87at%Ge alloy specimen, **B**=001.

orientation relationship between the matrix and the Ge-rich plates is suggested to be $(100)_M \parallel (100)_p$, $[010]_M \parallel [010]_p$, where M and P denote the matrix and the Ge-rich zones respectively.

As the Ge concentration of the alloy increased, the contrast of the Ge-rich regions became more identifiable. It was no longer restricted around the extinction contour but appeared everywhere. Fig.66 is an example exhibiting this kind of situation which was observed in thin foil samples of Ni-11.98at%Ge alloy. Streaks along both [100] and [010] directions are observed in the SADP. Since the amount of the Ge-rich regions in the alloy is appreciable the intensity of the streaks is also strong.

4.8. Isothermal Phase Transformation in Ni-14.56 at%Ge Supersaturated Solid Solution

4.8.1. Determination of Suitable Sample Thickness and Aging Temperature Range For the Study

As was summarized in Chapter 2, it seems possible that the early stage of Ni_3Ge precipitation might occur in supersaturated Ni-Ge solid solutions when these alloys are cooled during quenching from the solution treatment temperature; at which point high microhardness values occur. Therefore, an as-quenched sample of the Ni-14.56at%Ge alloys was studied. These studies suggested that the precipitation did not proceed to completion during quenching from the solution treatment temperature. Therefore, the precipitation process was studied further by examining the isothermally aged as-quenched specimens.

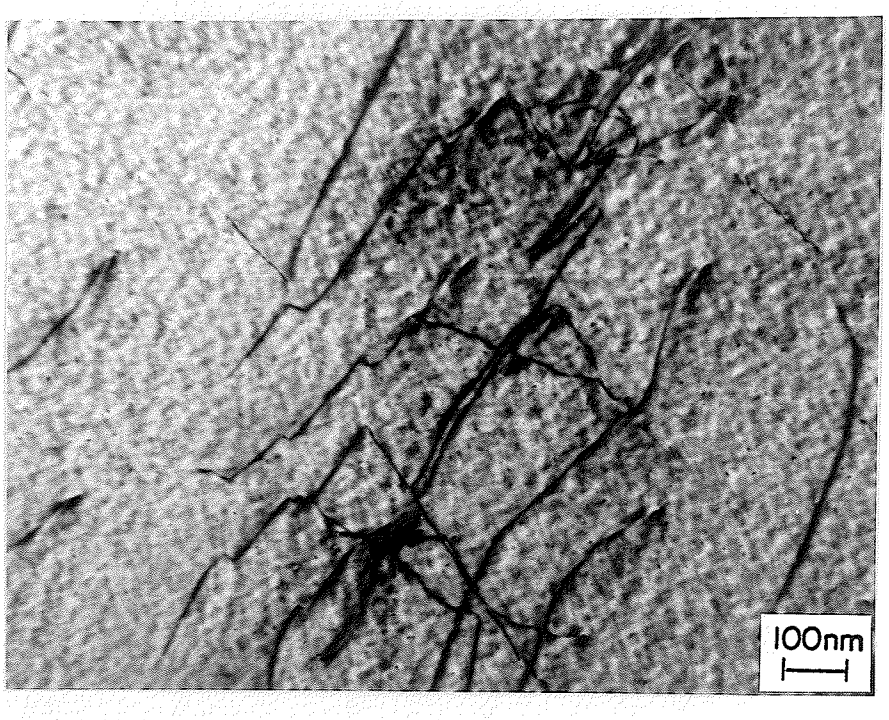

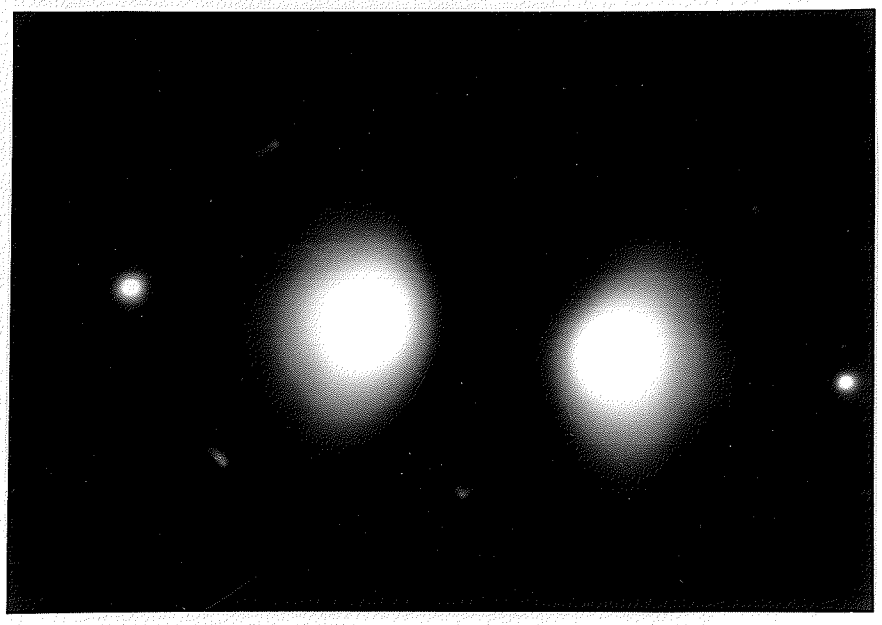

Fig.66 (a) TEM micrograph of a Ni-11.98at%Ge alloy specimen and (b) SADP of area in (a).

The first step of the study was designed to find out an appropriate sample thickness to obtain a sufficiently fast quenching rate at which the initial stages of Ni_3Ge precipitation could be effectively suppressed. Specimens with different thickness were encapsulated separately in argon filled vycor tubes. A vertical furnace was used for heating and quenching the specimens. The thickness of the specimen was found to be very crucial in controlling the quenching rate and consequently in suppressing the Ni_3Ge precipitation. When the specimens were thicker than 1 mm, distinguishable Ni_3Ge peaks would appear in the x-ray diffraction pattern of the as-quenched samples. Fig.67 shows the x-ray diffractogram of a specimen exhibiting the (100), (110) and (222) diffraction peaks due to the ordered Ni_3Ge precipitates. The microhardness values of these kind of samples were found to be over 400 VHN. Such a high hardness value is obviously due to the strengthening effect of the Ni_3Ge precipitates. Since the intensity of the (100) superlattice peak was found to be the strongest among these three visible peaks due to Ni_3Ge, the presence of this peak was used to identify the occurrence of Ni_3Ge precipitation in the as-quenched material at a later stage. It was found that, by decreasing the thickness of the sample to about 0.8 to 1.0 mm, the cooling rate was fast enough to suppress the precipitation effectively. In this case, the (100) superlattice peak disappeared (Fig.68) and the corresponding microhardness value of the as-quenched sample was 250 VHN. Thin foils were then prepared from these as-quenched samples and observed in a TEM. An example of the microstructure of the thin foil is shown in Fig.69. Two microstructural characteristics are evident. The first is that the contrast of the micrograph is somewhat mottled. In some areas very faint ripple like fringes seem to exist. However, the electron diffraction patterns observed in a series of predominant matrix zones did not exhibit any extra diffraction spots at this stage. This is consistent with the results of the x-ray diffraction investigation conducted on the bulk samples which suggested that the solid solution is in a supersaturated state with a fcc structure. Another microstructural feature is that the dislocation substructure exhibits a planar slip behaviour which is very similar to the

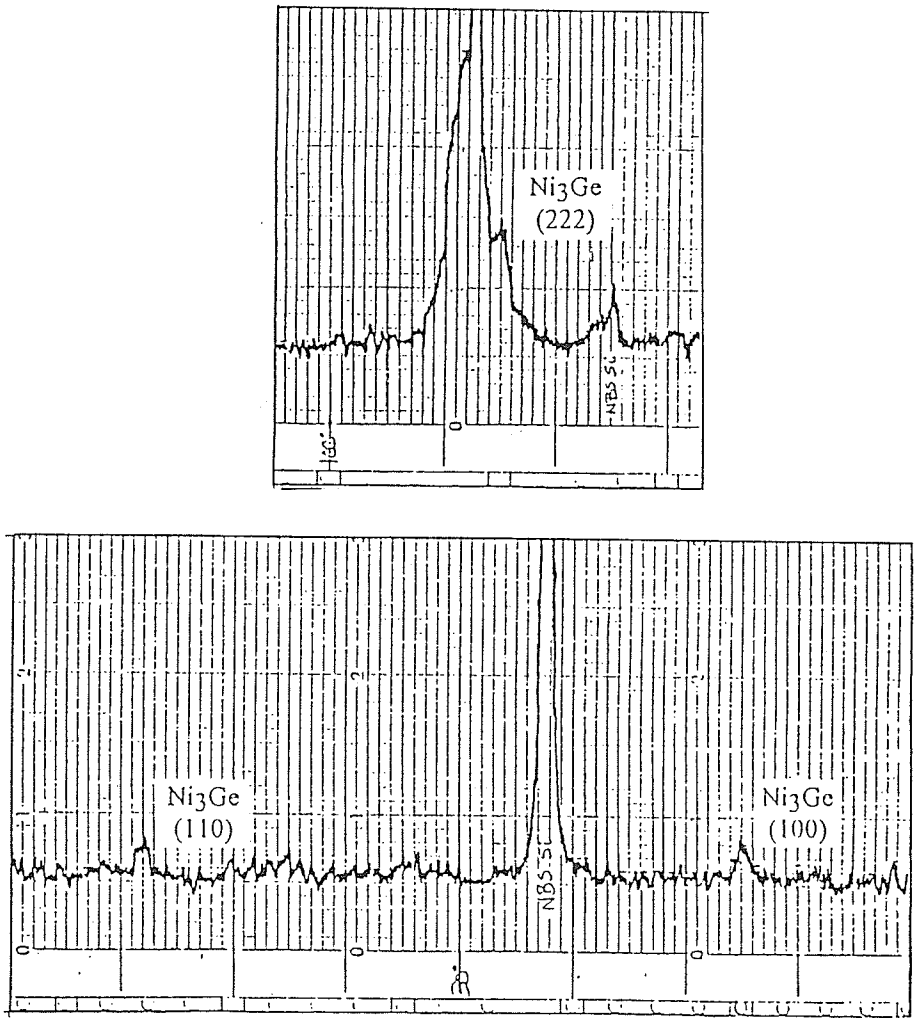

Fig.67 X-ray diffraction pattern from a 2 mm thick sample of Ni-14.56at%Ge alloy in the as-quenched condition.

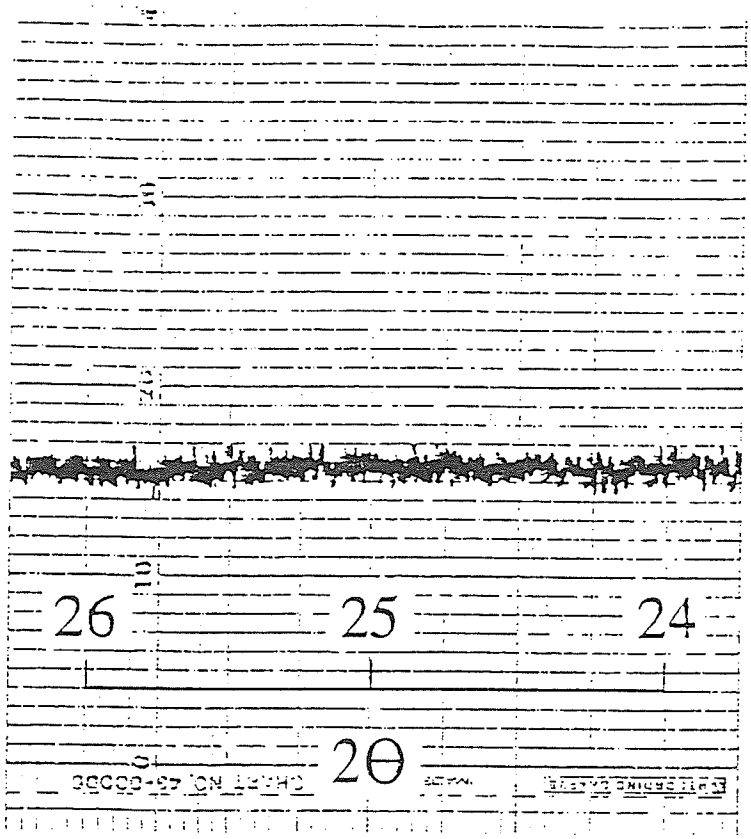

Fig.68 X-ray diffraction pattern from a 0.8 mm thick sample of Ni-14.56at%Ge alloy in the as-quenched condition.

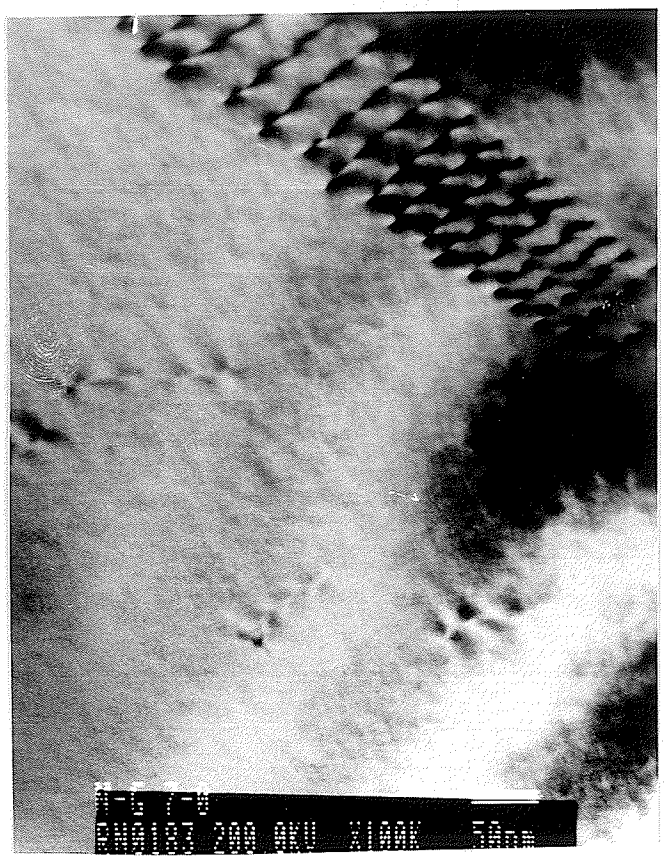

Fig.69 TEM micrograph of a Ni-14.56at%Ge specimen in the as-quenched condition.

one observed in the concentrated Ni-Ge solid solutions. Although the specimen was not deformed before the TEM observation, slight deformation was probably induced during the sample preparation and handling, and was probably responsible for the formation of the dislocation substructure.

After the appropriate sample thickness was determined, a survey of appropriate ageing temperature range was conducted. When the as-quenched samples were aged at 850 °C for 5 minutes, the TEM studies showed that they had a large number of cubic precipitate particles within the matrix. The strain field contrast due to the presence of the precipitate particles is visible near the extinction contours in Fig.70. The SADP of this area, as illustrated in Fig.71, exhibits the existence of weak superlattice spots. In CDF mode these particles appear bright. An example of this is given in Fig.72. After the diffraction pattern was indexed, the spots were found to be the (100), (110) superlattice reflections of the Ni_3Ge phase. From this diffraction pattern the lattice parameter of the Ni_3Ge is calculated to be 0.357 nm which is in good aggrement with the value reported by other researchers [100]. Therefore, these particles were believed to be equilibrium Ni_3Ge precipitates. The average size of the Ni_3Ge particles in Fig.72 was 100 nm. Within some of these Ni_3Ge particles, which are labelled A in Fig.72, fine fringes were observed. These fringes seem to be the antiphase boundaries between two adjacent ordered Ni_3Ge particles with different orientation. As shown in Fig.73, dislocations were found to be present around the interphase interface between the Ni_3Ge particles and the matrix. This implies that these particles are no longer totally coherent with the matrix. Instead, their relationship becomes semi-coherent and therefore interface dislocations are introduced to accommodate the lattice misfit between these two phases. These two microstructural features indicate that the alloy aged at 850 °C for 5 minutes is already at a coarsening stage and is no longer of any concern to the present study. Therefore, samples aged at lower temperatures for a different times were investigated. Thin foils of these aged samples were prepared and observed in

Fig.70 TEM micrograph of a Ni-14.56at%Ge specimen aged at 850°C for 5 minutes.

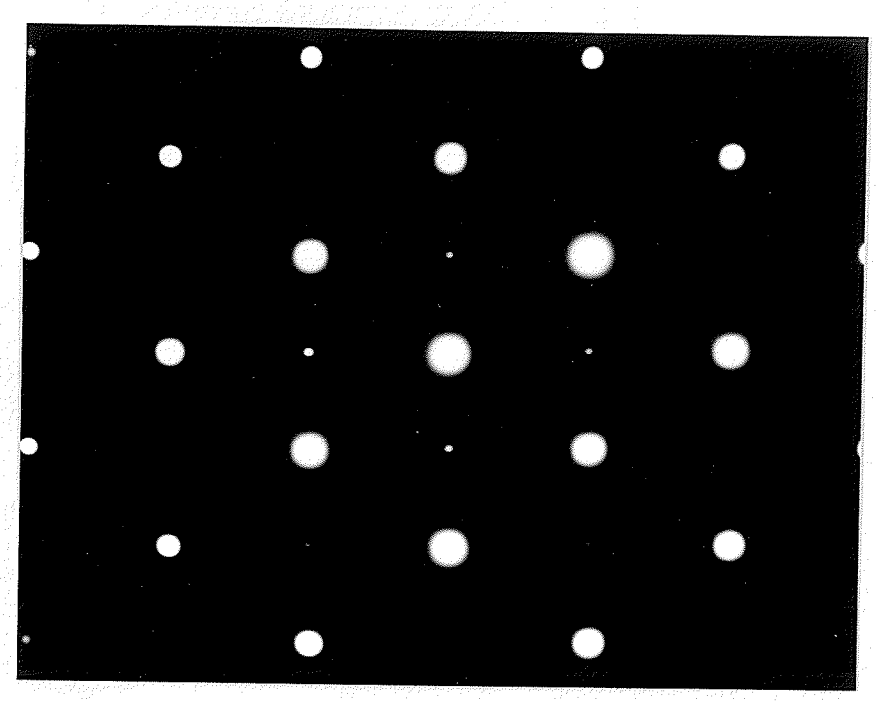

Fig.71 SADP of the area shown in Fig.70.

Fig.72 CDF of Ni_3Ge precipitates observed in a Ni-14.56at%Ge alloy specimen aged at 850°c for 5 minutes.

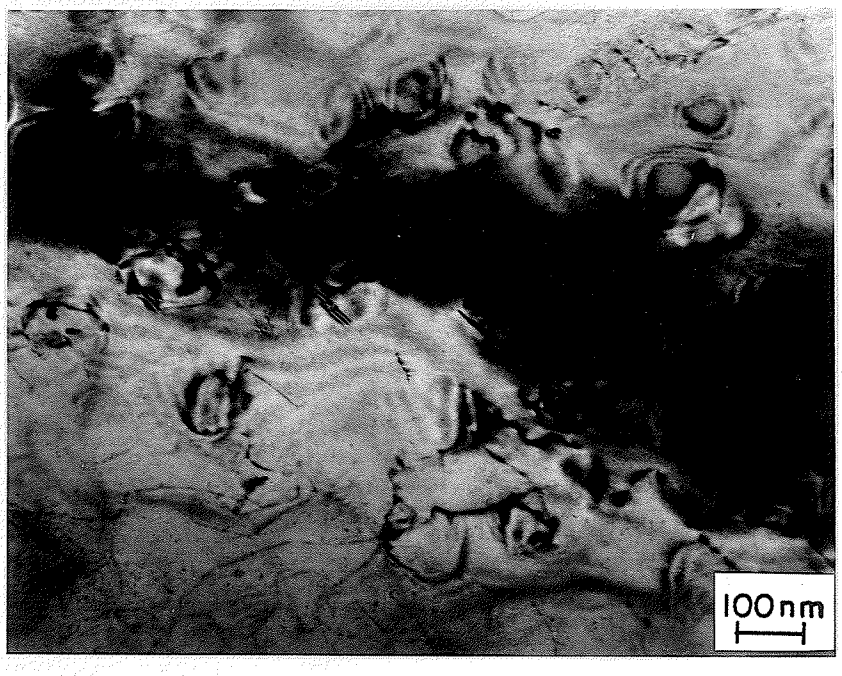

Fig.73 TEM micrograph of a Ni-14.56at%Ge specimen aged at 850° for 5 minutes.

the TEM.

Samples, which were aged at 600 °C for 15 minutes, exhibited a modulated microstructure which is illustrated in Fig.74. Dark and white wavy regions were found to be periodically arranged along the <100> direction of the matrix. The average separation between the two adjacent white and dark regions was about 15 nm. The modulated microstructure was homogeneously distributed throughout the matrix. The SADP of the area shown in Fig.74 is illustrated in Fig.75. From Fig.75 it is seen that the (200) and (400) diffraction spots look somewhat elongated along the <100> direction. To find out the reasons for the directional elongation of these diffraction spots the photographic film containing the SADP was further examined by using a transmission optical microscope. An enlarged view of the (400) reflection is shown in Fig.76. The presence of satellite spots on both sides of the main reflection along the [100] direction was revealed from the enlarged diffraction spot of the (400) reflection. These two satellites are labelled as s in Fig.76. In overexposured photographic plates of the diffraction, the presence of superlattice diffraction spots was revealed. An example is shown in Fig.77a where (001) and (110) superlattice spots are visible. These spots are attributed to the Ni_3Ge-γ' precipitates. An overexposured dark field micrograph taken with the (001)-γ' superlattice reflection is shown in Fig.77b. The presence of fine γ' particles, which appear as bright particles in the micrograph, is evident. These particles were not observed to nucleate preferentially at grain boundaries or dislocations, but were distributed homogeneously within the matrix and aligned themselves regularly along the [100] direction of the matrix.

The presence of the satellite or side-band effect in the electron diffraction pattern was studied further using x-ray diffraction with bulk samples aged at 600 °C for 15 minutes. A typical intensity profile of the (200) diffraction peak of these samples is shown

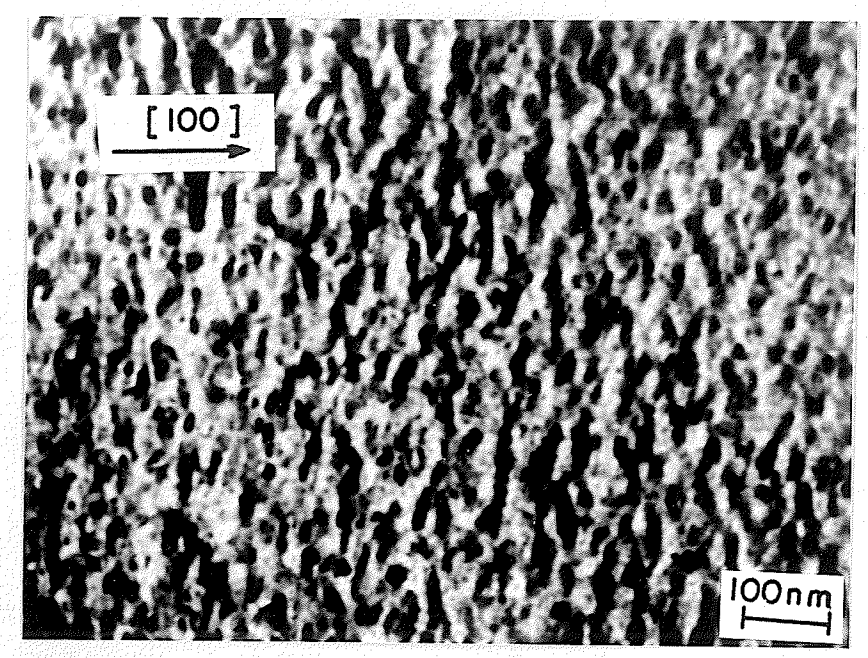

Fig.74 TEM micrograph of a Ni-14.56at%Ge specimen aged at 600°C for 15 minutes.

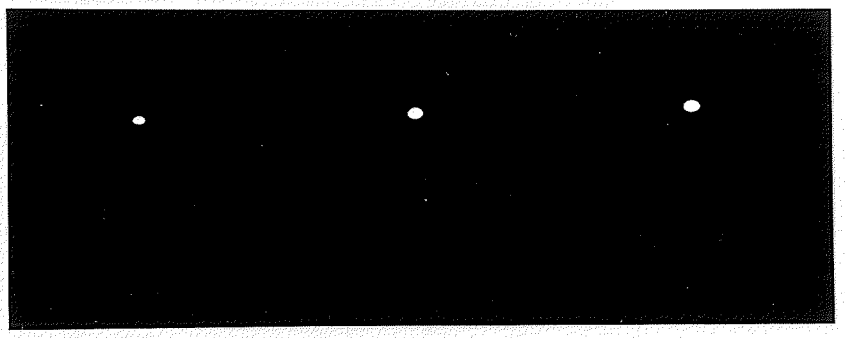

Fig.75 SADP of the area shown in Fig. 74

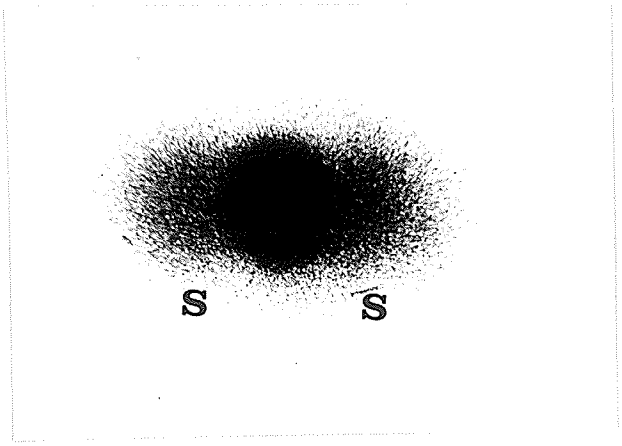

Fig.76 Transmission optical micrograph of (400) diffraction spot shown in Fig.75.

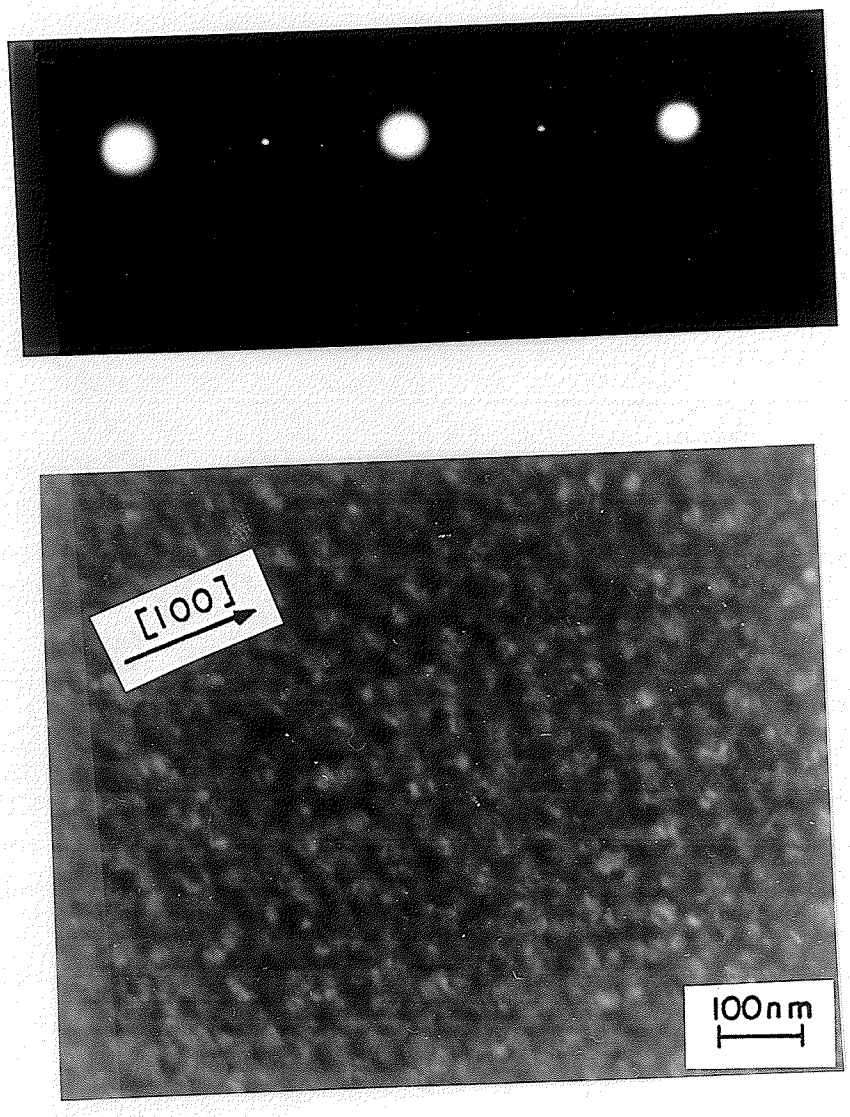

Fig.77 Overexposured SADP of the Ni-14.56at%Ge specimen aged at 600°C for 15 minutes and (b) central dark field micrograph of the specimen taken with the (100) superlattice reflection shown in (a).

in Fig.78. Side-bands appearing on both sides of (200) diffraction peak of the matrix were observed. The position of these two subpeaks was found to be symmetrical with respect to the (200) main reflection. The intensity of these subpeaks is very weak as compared to the intensity of the main (200) peak. It is known that the side-band effect and modulated microstructure are two typical TEM microstructural characteristics caused by spinodal decomposition which occurs during the period of decomposition of an unstable supersaturated solid solution. The build up of composition fluctuations caused by spinodal decomposition is the necessary condition which brings about these two diffraction effects. Since spinodal decomposition in an alloy system involves a continuous process during which the free energy of the system decreases simultaneously, the nucleation stage of the precipitation process is not necessary and the crystal defects, such as dislocations and grain boundaries, are not required as the nucleation sites for the precipitates to form. Therefore, the other important microstructural feature of an alloy which experiences spinodal decomposition is the homogeneous and regular distribution of fine precipitates. Therefore, according to the TEM microstructural features observed in a Ni-14.56at%Ge alloy aged at 600 °C for 15 minutes, it seems possible that spinodal decomposition occurs in the alloy. It is, however, recognized that a microstructure similar to the one produced by spinodal decomposition may sometimes be obtained by the coarsening of precipitates produced by nucleation and growth mechanism. For example, Ardell and Nicholson have reported that in aged Ni-Al alloy the aligned arrays of Ni_3Al-γ' particles, similar to that produced by spinodal decomposition, could be produced by stress-affected coarsening of an initially random distribution of γ' particles [23]. Therefore, transformation characteristics of a Ni-14.56at%Ge alloy as a function of ageing time and temperature have been investigated further using x-ray diffraction techniques. Special emphasis has been placed on the initial stages of the decomposition process, since it is crucial in the identification of the true decomposition mechanism.

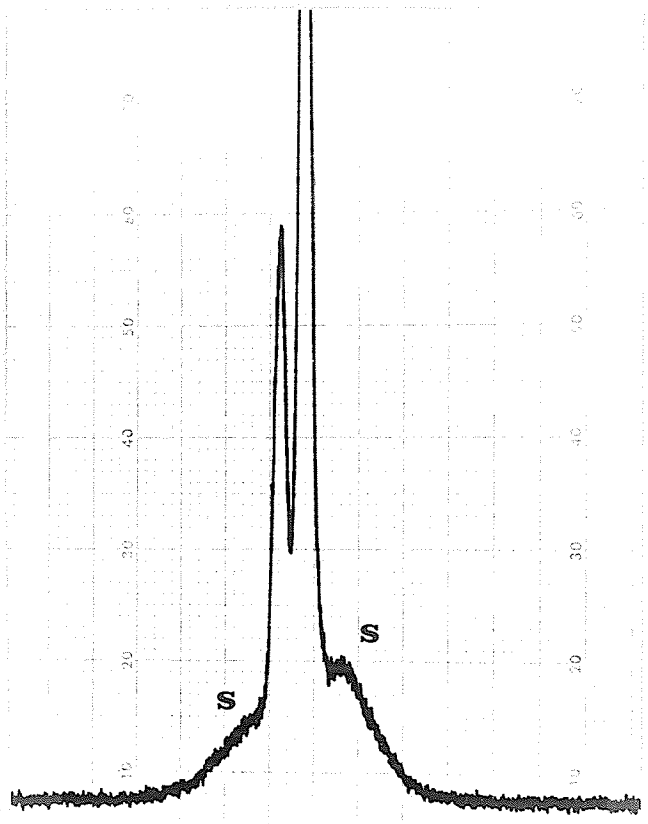

Fig.78 The intensity profile of the (200) x-ray diffraction peak of a Ni-14.56at%Ge bulk specimen aged at 600°C for 15 minutes.

The results of this preliminary study conducted by TEM and x-ray diffraction techniques are briefly summarized as follows:

a. A satisfactory quenching rate can be obtained so that the early stage of Ni_3Ge-γ' precipitation in Ni-14.56at%Ge alloy during quenching can essentially be suppressed.

b. Temperatures of 600 °C and lower are suitable aging temperatures to investigate the spinodal transformation mechanism.

c. The sideband effect as well as a modulated microstructure were observed by using both TEM and x-ray diffraction techniques.

d. The alloy aged at 600 °C appears to undergo spinodal decomposition

As mentioned in Chapter 2, the angular deviation of the side-band or the satellite peak from the main diffraction peak is a function of the wavelength of the composition fluctuation in a real crystal. If the angular deviation can be measured precisely, the wavelength and the relationship between the wavelength and the ageing time can be determined accurately. Since this kinetic behaviour reflects the information about the reaction path of the precipitation process it is believed to be an important criterion for distinguishing the mechanism of spinodal decomposition from that of conventional nucleation and growth. By comparing the experimental results obtained by electron diffraction with those obtained by x-ray diffraction, it is obvious that the angular resolution obtained by x-ray diffraction using the diffractometer technique is much better. In addition, since the diffraction intensity of the sidebands actually reflects information about the composition modulation, measurements of the intensity are necessary. When the x-ray

diffractometer is used, the diffraction intensity can be recorded and measured directly from the chart paper. Therefore, the x-ray diffraction technique has a distinct advantage and was selected for further study of the phase transformation in Ni--14.56at%Ge alloy.

4.8.2 X-ray Diffraction Study of Phase Transformation Behaviour of Isothermally aged Ni-14.56 at%Ge Alloy

A. Development of (200) reflection profile of the alloy aged at 600 °C.

As mentioned in Chapter 2, since the (200) diffraction peak of the matrix gives the best combination of sideband resolution and intensity, i.e. larger value of angular deviation ($\Delta\theta$) and higher intensity value. These variations in intensity profile of (200) reflections from the aged alloy with changes in ageing time was studied first .

The x-ray diffraction pattern of the solution treated and quenched specimen showed the presence of a very weak and diffuse profile of an intensity fluctuation on the lower angle side of the (200) diffraction peak (Fig.79a). However, such a profile could not be detected on the higher angle side. The presence of a side-band, although very weak and diffuse, suggests that composition fluctuations are present in the solution treated and quenched specimen. It is likely that the mottled contrast observed in the TEM foil of the as-quenched sample, and illustrated in Fig.69, is also due to the presence of a composition fluctuation. The fluctuation in composition induces a corresponding fluctuation in atomic scattering factor and lattice spacing in the material, and consequently leads to the contrast effect. When the sample was aged for 5 minutes, sidebands were observed on both sides of the (200) reflection, as shown in fig.79b. Although the sidebands were still very weak and diffuse, their intensity was stronger than that observed in the solution treated and quenched

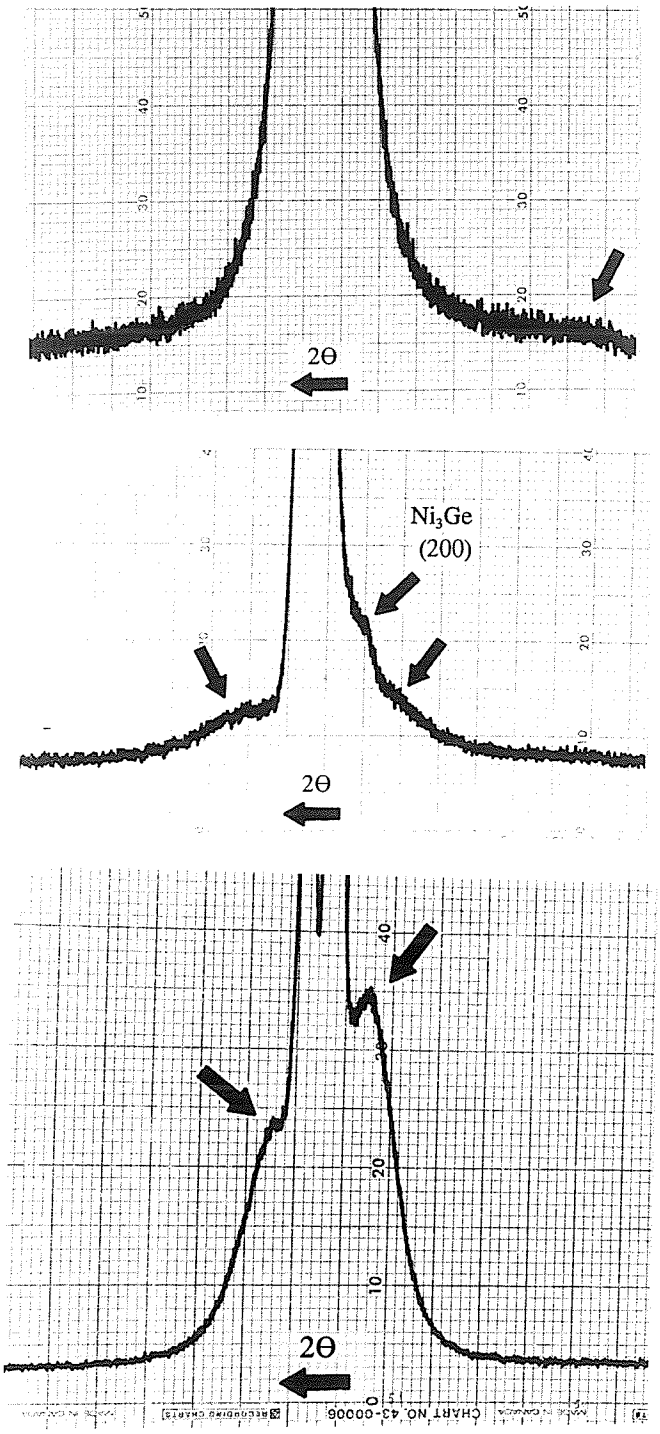

Fig.79 Different shapes of the intensity profiles of (200) x-ray diffraction peaks in a Ni-14.56at%Ge specimen after (a)water-quenched and then aged for (b) 5 minutes and (c) 40 minutes.

specimen and the peak position of the sidebands was closer to the main reflection. The (200) x-ray diffraction profile of the specimen aged for 40 minutes is shown in Fig.79c. As compared to Fig.79 a,b, it should be noted that , after longer time of ageing, the side-band peaks were much better defined, were of stronger intensity and their positions were closer to the main (200) reflection.

According to Daniel and Lipson [5], when (200) reflection of the matrix is selected the wavelength of the composition modulation, λ, can be determined by the following expression

$$\lambda = a_0 \tan(\Theta_B) / 2\,\Delta\Theta \qquad (86)$$

where, Θ_B is the Bragg angle of the main peak, a_0 is the average lattice parameter of the alloy, and $\Delta\Theta$ is the angular deviation of the sideband from the Bragg peak which can be measured directly from the diffraction pattern. The values of λ after various lengths of ageing time up to 40 minutes at 600 °C are given in Fig.80. The value of λ increases with ageing time. At first the rate of increase is very rapid but slows down at later stages of ageing. The log-log plot of the variation in the value of λ with ageing time is illustrated in Fig.81. This plot is a straight line with a slope of 1/3 which is the same as the value of the slope observed in Cu-Ni-Sn [87] and Cu-Ni-Fe [88] alloys that are believed to be typical spinodal alloys.

According to the Cahn's theory of spinodal decomposition [13], there should be a composition modulation of wavelength λ_m, which would have the maximum amplification factor and would be in the most favorable condition to grow as compared to the other waves. Cahn's theory also predicts that the value of wavelength λ_m, does not change over

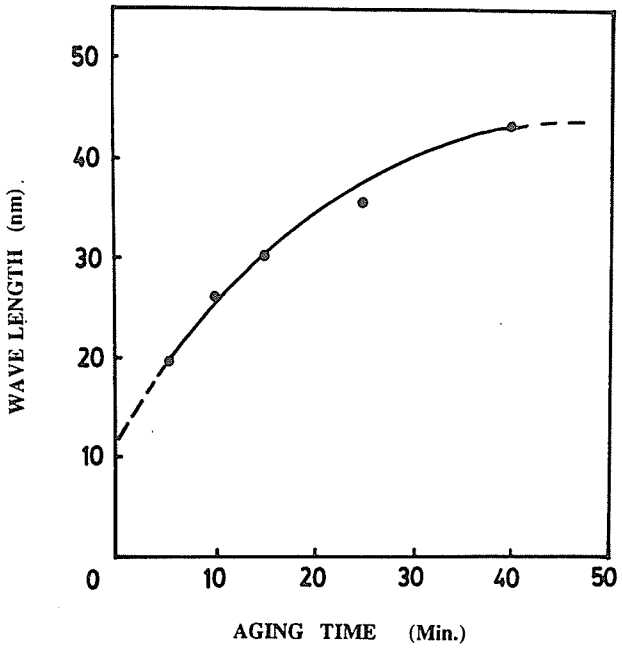

Fig.80 Variation in composition modulation wavelength in a Ni-14.56at%Ge alloy with ageing time at 600 °C.

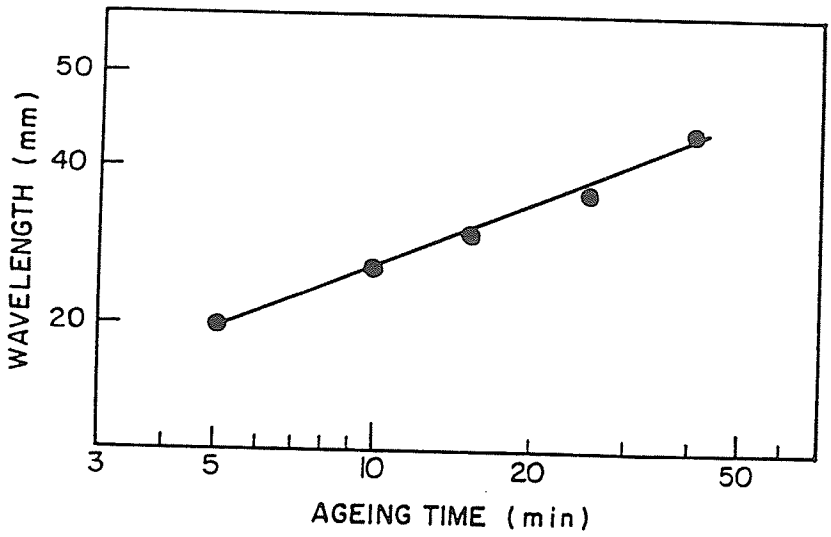

Fig.81 A log-log plot illustrating the variation in wavelength of composition modulation as a function of ageing time at 600°.

a short ageing period. The presence of such a constant wavelength has been observed in a number of alloy systems that undergo spinodal decomposition [89-91] and is considered to be one of the most important kinetic characteristics of spinodal decomposition. When the Ni-14.56at%Ge alloy was aged at 600 °C , the value of the wavelength of the composition modulation was observed to vary continuously during the ageing period of 5 to 40 minutes. Since the process is actually diffusion controlled and occurs rapidly at higher temperatures, it is likely that the duration over which the value of λ remains constant is too short to be detected at this particular ageing temperature. Therefore, an ageing temperature of 550 °C was selected for further study.

B. Development of (200) reflection profile of the alloy aged at 550 °C

After the sample was aged for 5 minutes, profile of the (200) reflection, illustrated in fig.82a, shows asymmetry in intensity and the intensity on the lower angle side of the peak seems to be stronger. This situation is very similar to the one when the alloy was aged at 600 °C. Therefore, the intensity asymmetry is suggested to be due to the contribution of the sidebands one of which appears first on the lower angle side of the main peak. Dashed lines are used to illustrate the intensity profile of the (200) main diffraction peak which is due to the matrix itself and is symmetrical on both sides of the peak. The profile of the sideband due to the composition modulation can then be determined by subtracting the intensity value of the dashed curve from that of the original curve. Thereby, the shape and the position of the side-bands are illustrated above the original intensity profile. Using a similar treatment the variation in shape, position as well as the intensity of the sidebands with ageing time is shown in Fig.82. After 10 minutes of ageing, sidebands on both sides of the (200) diffraction peak become visible. By measuring the value of $\Delta\theta$, which is used

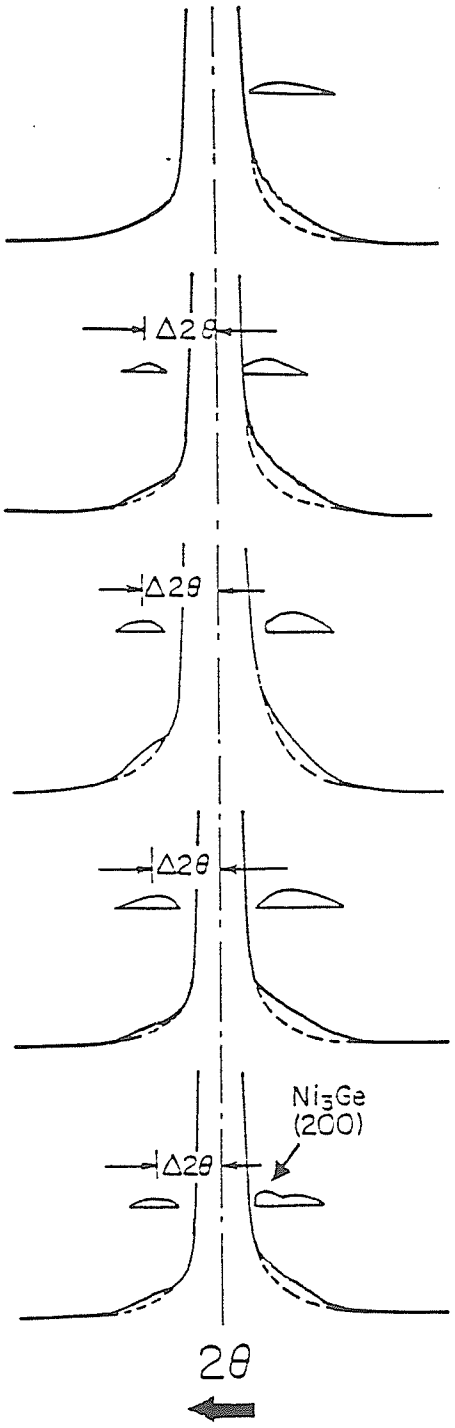

Fig.82 Variation in intensity profile of (200) reflection of the Ni-14.56at%Ge alloy with ageing time aged at 550°C for (a) 5 minutes (b) 10 minutes (c) 15 minutes (d) 20 minutes and (e) 25 minutes.

to express the angular deviation of the sideband, from the main peak, the value of wavelength is calculated to be 24.5 nm. The value of $\Delta\theta$ is observed to remain constant for up to 15 minutes of ageing. However, the intensity of the sidebands, which is the area under the intensity profile of the side-bands, continues to increase with ageing time. This implies that the amplitude of the composition modulation increases with the ageing time. After 25 minutes of ageing, the (200) reflection of Ni_3Ge can be detected. This situation is shown in Fig.82e. The value of $\Delta\theta$ starts to decrease and the wavelength of the composition modulation is calculated to be 25.1 nm. This value shows a small increase compared to the original value. This indicates that the period during which the wavelength keeps a constant value is over.

C. Development of (100) reflection of the alloy aged at 600 °C.

In the solution treated and quenched condition, the (100) superlattice peak of Ni_3Ge-γ' is not observed in the x-ray diffractogram which is shown in Fig.83a. After 5 minutes of ageing, a very weak and diffuse (100) superlattice reflection of Ni_3Ge-γ' appears (Fig.83b). As ageing progresses, the (100) peak becomes stronger and sharper due to an increase in the volume fraction of the Ni_3Ge-γ' precipitates. This situation is illustrated in Fig.83c and d. The integrated intensity of the (100) peaks can be used to estimate the fraction of the equilibrium volume fraction of γ' precipitated after various ageing time in the following manner.

The integrated intensity of the (100) peak of Ni_3Ge-γ' phase, I_{γ}, can be expressed by [92]:

$$I_{\gamma'} = K C_{\gamma'} / \mu_s \qquad (87)$$

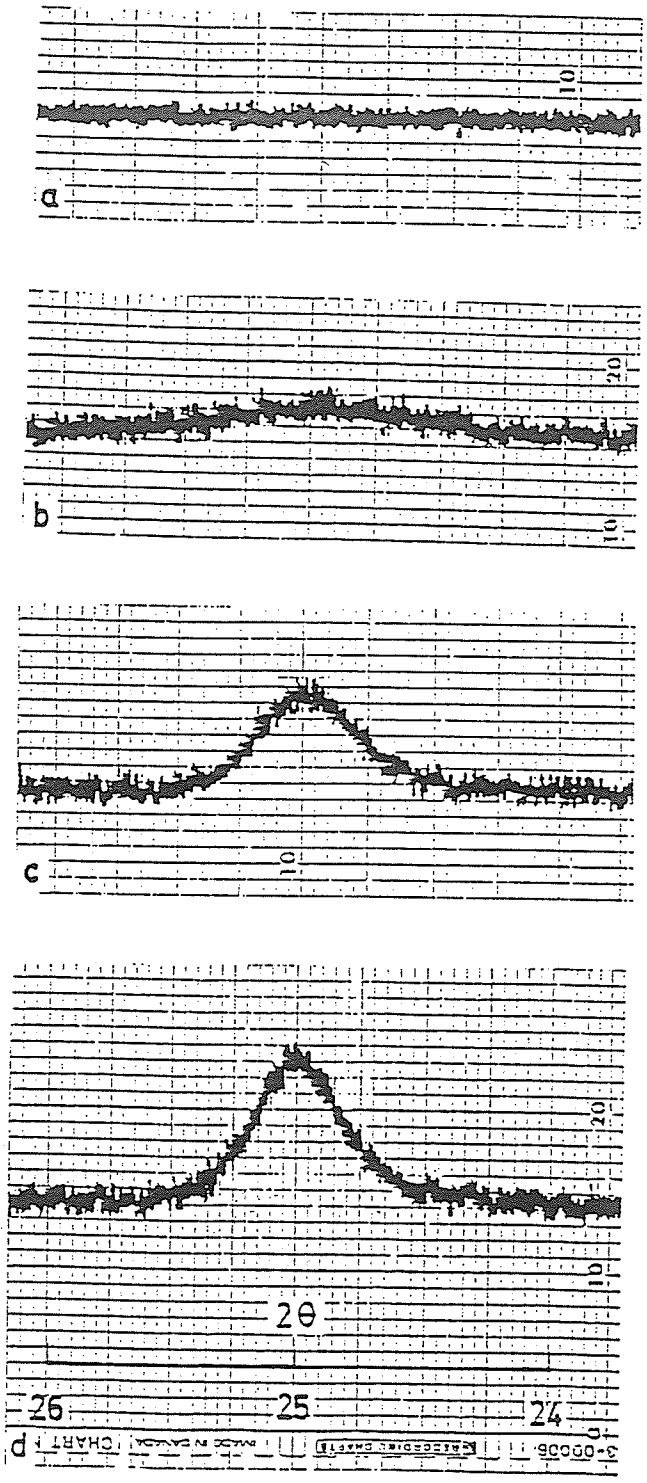

Fig.83. Intensity profiles of (100) super lattice reflection in the Ni-14.56at%Ge alloy in the (a) as-quenched condition and aged for (b) 5 minutes (c) 25 minutes and (d) 40 minutes.

where $C_{\gamma'}$ is the volume fraction of γ' in the γ matrix, μ_s is the linear absorption coefficient of the specimen consisting of (γ+γ') and K is a constant. The linear absorption coefficient of the specimen, μ_s is given by the following expression [92],

$$\mu_s = C_{\gamma'}(\mu_{\gamma'}-\mu_\gamma)+\mu_\gamma \tag{88}$$

where, $\mu_{\gamma'}$ is the linear absorption coefficient of the Ni_3Ge-γ' phase and μ_γ is the linear absorption of the matrix containing γ' precipitates. The linear absorption coefficient μ_s of a specimen consisting of constituent 1,2... to n can be calculated from the following expression:

$$(\mu_s/\rho_s) = [\,\omega_1(\mu/\rho)_1 + \omega_2(\mu/\rho)_2 + ... + \omega_n(\mu/\rho)_n] \tag{89}$$

where, ω, μ and ρ are the weight fraction, linear absorption coefficient and density of various constituents in the specimen, respectively, and ρ_s is the density of the specimen. According to the Ni-Ge phase diagram, at 600 °C the equilibrium concentration of Ge in Ni_3Ge-γ' phase and the γ matrix is 26.4wt% and 14.4wt% respectively [55]. The values of the mass absorption coefficient and densities of Ni and Ge are known [92] and the densities of the Ni_3Ge-γ' and the Ni-17wt%Ge (i.e. Ni-14.56at%Ge) alloy used in this study can be calculated. Therefore, the values of the linear absorption coefficient of Ni_3Ge-γ', $\mu_{\gamma'}$ and the matrix containing 14.4wt%Ge and 17.0wt%Ge, μ_γ, can be calculated from Eq.89. The values obtained were 435 cm^{-1}, 438 cm^{-1} and 437 cm^{-1} respectively. That is to say that, the linear absorption coefficient of the three species is nearly the same and according to Eq.88 the linear absorption coefficient of the specimen does not change upon ageing.

According to Eq.87 the integrated intensity of the (100) Ni_3Ge peak in a specimen

with an equilibrium amount of Ni_3Ge in it, $I_{\gamma'e}$, can be expressed by

$$I_{\gamma'e} = KC_{\gamma'e}/\mu_{se} \tag{90}$$

where, $C_{\gamma'e}$ is the equilibrium volume fraction of γ' and μ_{se} is the linear absorption coefficient of the specimen containing equilibrium volume fraction of γ' in it. Similarly, the integrated intensity of the (100)-γ'peak in a specimen after ageing time t can be expressed as follows

$$I_{\gamma't} = K\, C_{\gamma't}/\mu_{st} \tag{91}$$

where, $C_{\gamma't}$ is the volume fraction of the γ' phase after ageing time t and the μ_{st} is the linear absorption coefficient of the specimen containing $C_{\gamma't}$ in it. From Eqs 90 and 91

$$C_{\gamma't}/C_{\gamma e} = (I_{\gamma't}/I_{\gamma'e})\ (\mu_{se}/\mu_{st}) \tag{92}$$

As concluded earlier, the values of μ of the specimen do not change due to ageing, i.e. $\mu_{se}=\mu_{st}$, therefore,

$$C_{\gamma't}/C_{\gamma e} = (I_{\gamma't}/I_{\gamma'e}) \tag{93}$$

From this expression the fraction of the equilibrium volume fraction of Ni_3Ge phase precipitated after various ageing times can be determined by comparing the integrated intensity of the (100)-γ' peak in the aged specimen with that observed in a specimen containing the equilibrium volume fraction of γ'. Therefore, a specimen was solution treated at 1100 °C and then furnace cooled to produce the equilibrium volume fraction of γ'

phase in it. The corresponding (100) Ni_3Ge peak is shown in Fig.84. The integrated intensities of the (100) peak in the specimen aged at 600 °C for various lengths of time were determined by measuring the areas under the peaks and the ratios of the $C_{\gamma' t}/C_{\gamma e}$ were determined by Eq.93. The values of $C_{\gamma' t}/C_{\gamma e}$ against ageing time are plotted in Fig.85. The formation of Ni_3Ge occurs very rapidly during the early stages of ageing followed by a slower rate of precipitation. This plot also shows that nearly 55% of γ' had formed within the first 10 minutes of ageing, about 80% during the next 20 minutes and 95% of γ' has formed during the first 40 minutes of ageing.

4.8.3 Ageing Hardening Effect of the Alloy Aged at 600 °C and 550 °C

In the as-quenched condition, the hardness of the alloy was measured to be 250 VHN. This high value can not be attributed solely to the solid solution strengthening of the Ge solute in the matrix. Probably, the phase separation, which was found to occur in the alloy during quenching from the solution heat treatment temperature, is also contributing to the high hardness value.

The variation in microhardness with ageing time at 600 °C is shown in Fig.86. It is seen that after 5 minutes of ageing, the hardness has increased by nearly 45%. Since at this stage only about 8% of Ni_3Ge precipitates is present, which can be deduced from Fig.85, the observed increase in hardness may be mainly attributed to the composition modulation due to the spinodal decomposition. On further ageing the hardness increases continuously and reaches a peak value of about 500 VHN after 25 minutes of ageing, which is 90% greater than the hardness of the solution treated and quenched material. As seen in Fig.85, a significant amount of Ni_3Ge-γ' precipitates forms between 5 and 25 minutes of ageing, therefore, as the ageing time is increased beyond 5 minutes Ni_3Ge-γ'

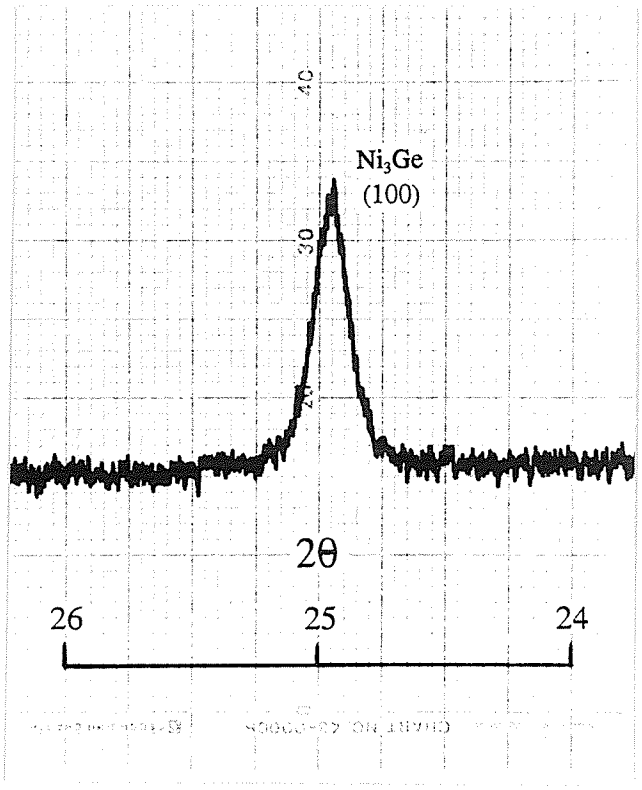

Fig.84 The (100) superlattice peak of equilibrium Ni_3Ge precipitates in the Ni-14.56at%Ge alloy after solution treating and furnace cooling .

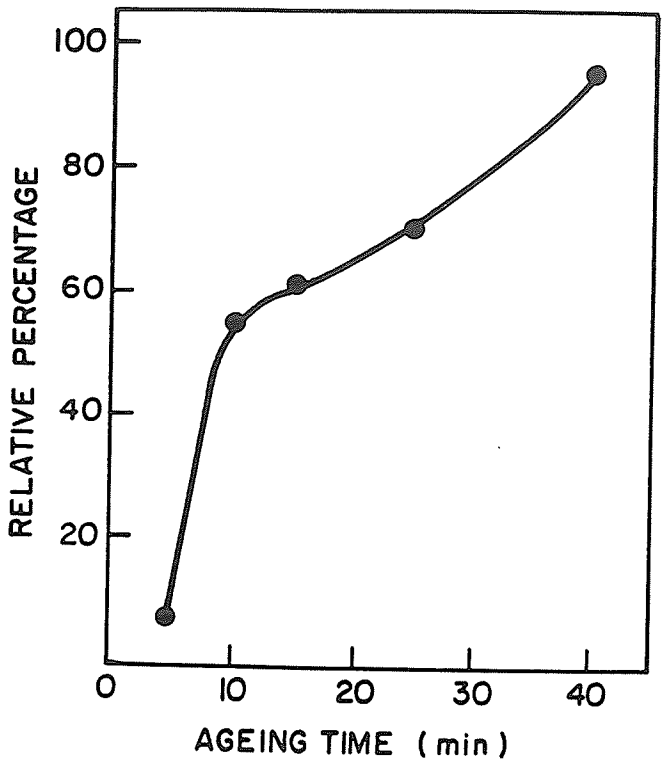

Fig.85 Variation in relation percentage of Ni_3Ge precipitated with ageing time at 600°C.

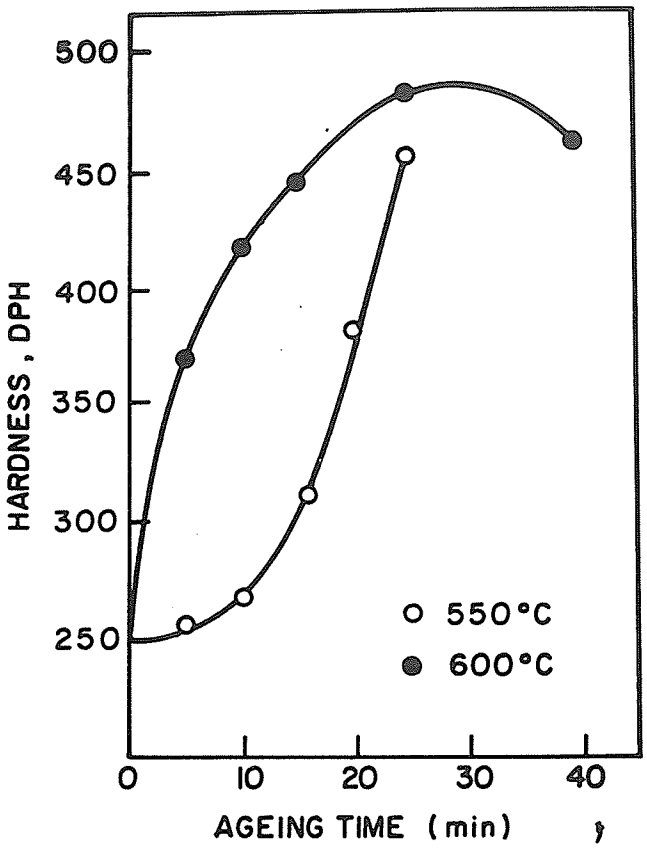

Fig.86 Variations in microhardness of Ni-14.56at%Ge alloy with ageing time at 600°C and 550°C respectively.

precipitates start to influence the hardness of the material. In the peak-aged condition, it is suggested that most of the hardening effect is due to the contribution of Ni_3Ge-γ' particles. After ageing for 40 minutes the hardness decreases slightly but still maintains a high value.

For comparison, the variation in hardness of the alloy with ageing time at 550 °C is also given in Fig.86. It is seen that due to the lower ageing temperature, the plot of the hardness vs ageing time is shifted towards longer times/lower hardness at 600 °C. The precipitation process seems to be delayed. Up to 10 minutes of ageing time, the hardness increases by a very small amount. By Comparing with Fig.82, it is recognized that this ageing period corresponds to the stage at which the wavelength of the composition fluctuation keeps a constant value and only the amplitude of the composition fluctuation wave increases with the ageing time. At this stage the Ni_3Ge-γ' has not yet precipitated. Therefore, it is suggested that, during this period, the increases in hardness is related to the increase in the amplitude of the composition fluctuation and the strengthening effect at this stage is not significant. When the alloy was aged at 600 °C, the period of constant composition wavelength could not be found. It was suggested that at that ageing temperature this period is probably too short to be identified. The results of this hardness tests seem to support the above suggestion. As seen in Fig.86, the microhardness value of the alloy, which was aged at 600 °C for 5 minutes, has already reached 370 VHN. Accordingly, it will take about 20 minutes of ageing for the alloy to reach this high value if it is aged at 550 °C. However, after such a long time of ageing, the wavelength of composition wave has been observed to start growing. Therefore, the high hardness value of the alloy, aged at 600 °C indicates that after 5 minutes of ageing the period of constant composition wavelength is over. When the alloy is aged at 600 °C, this period probably occurs within 1~2 minutes of initial ageing or even less. Experimentally, the investigation of this process is difficult. After 10 minutes of ageing, the increase in hardness is very

appreciable. By comparing with results shown in Fig.82, it is seen that this period corresponds to the increase in wavelength and in the amount of Ni_3Ge-γ' precipitation. This situation is very similar to that in which the alloy is aged at 600 °C, and the hardness increases very rapidly.

In Fig.86, it is seen that the hardness of the alloy increases continuously with ageing time at both 550 °C and 600 °C. This indicates that an incubation period which always occurs during a precipitation process controlled by a nucleation and growth mechanism does not exist in the present case. The increase in hardness at the very initial ageing stage is directly related to the increase in the wavelength of composition fluctuation.

CHAPTER 5

Discussion

In this chapter, the experimental results concerning the existence of localized ordering in concentrated Ni-Ge solutions are first discussed and compared with studies carried out on other alloy systems, and the presence of Ge-rich zones in the concentrated solutions is confirmed. By means of a thermodynamical analysis the behaviour of Ge solute atoms in the Ge-rich zones is suggested to be similar to the one observed in the totally ordered Ni_3Ge intermetallic compound. That is, the Ge-rich zones are suggested to be somewhat locally ordered. By examining the variation in e/a ratio with Ge addition and considering its influence on the phase stability, the fcc crystal structure of the Ni-Ge solid solutions appears to become unstable with respect to the $L1_2$ crystal structure due to the Ge addition. It is also suggested that a series of transition states between the totally disordered fcc crystal structure and the totally ordered $L1_2$ crystal structure exist between these two states. After that, the relationship between the locally ordered Ge-rich zones and the characteristics of the dislocation substructure of the deformed material is discussed. Finally, an explanation of the negative deviation in the lattice parameter vs Ge concentration curve is proposed. In the second section of this chapter, characteristics of the continuous phase transformation of supersaturated Ni-14.56at%Ge alloy involving precipitation of Ni_3Ge phase are discussed. A possible reaction path for the phase transformation is

proposed by using a graphic thermodynamic analysis.

5.1 Localized Ordering in Concentrated Ni-Ge Solid Solutions

In the following sections, the experimental results obtained by the x-ray diffraction studies are first compared with the those obtained by TEM investigations. This comparison indicates that the diffuse scattering effect which has been detected by x-ray diffraction and the contrast effect which has been revealed by TEM studies are found to be mutually related, and the presence of the Ge-rich zones is suggested to be responsible for these two phenomena. Then by using a thermodynamic analysis, the state of the Ge-rich zones is suggested to be partially ordered. Based on the consideration of the variation in e/a ratio with Ge concentration within a Ni-Ge unit cell with Ge concentration, the addition of Ge is suggested to destabilize the fcc crystal structure and promote the formation of Ni_3Ge. After the relationship between the occurrence of SRO in the material and the dislocation distribution has been discussed, a possible reason for the planar slip dislocation configuration in the concentrated Ni-Ge solid solution is suggested. Finally, an explanation regarding the negative deviation of the lattice parameter vs Ge concentration curve of the Ni-Ge solid solutions is proposed.

5.1.1 Comparison of the Results Obtained by X-ray Diffraction and TEM Studies

The results of the x-ray diffraction studies have shown that there exists an asymmetry in the intensity profile of the (200) diffraction peaks of Ni-Ge solid solutions with Ge concentration ranging from two to twelve atomic percent. The presence of Ge-rich regions in the solid solutions is suggested to be responsible for the diffuse scattering effects which leads to the asymmetry in intensity profiles of the (200) reflections. The results of the TEM observations conducted on the solid solutions support the above suggestion. The images of Ge-rich zones suggest that they are thin plates of about 25×25 nm^2. Based on a study of the contrast effects induced by these zones in TEM images it is suggested that the orientation relationship between the matrix and the zones is $(100)_M \| (100)_P$, $[010]_M \| [010]_P$, where the M and P donate the matrix and the Ge-rich zones, respectively. Therefore, by a combined use of TEM and x-ray diffraction techniques the variation in composition, size and distribution of Ge-rich zones with Ge concentration in the concentrated solutions, as well as the crystallographic relationship between these zones and the matrix has been determined.

The results of TEM studies can also be used to explain the nature of the intensity profile of the (200) reflections from the specimens that were mounted on the x-ray diffractometer with their (200) planes parallel to the sample holder. According to the kinematical theory of x-ray diffraction, the intensity distribution of a diffraction peak is influenced by the shape of the material causing the diffraction of the x-ray beam. Since the shape of the Ge-rich regions is found to be a thin plate, the corresponding diffraction distribution should be a spike which is normal to the plane of the plate. This is schematically illustrated in Fig.87. The plane in which this spike lies will be the same as the one which contains the incident and diffracted x-ray beams. Therefore, the detector of the

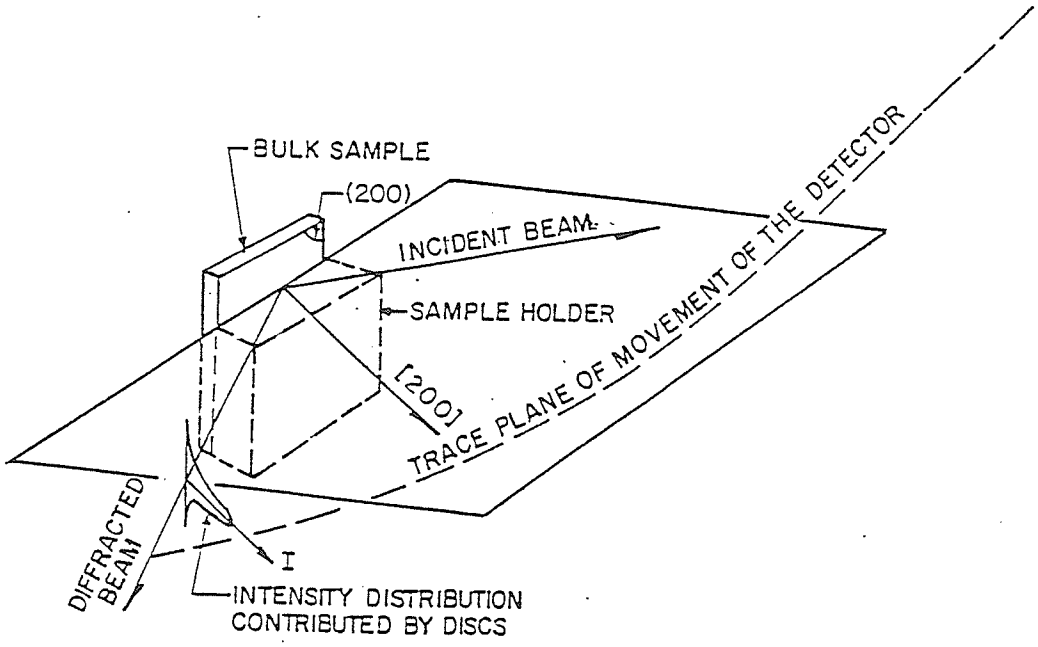

Fig.87 A schematic diagram illustrating the orientation of an x-ray diffraction specimen with respect to the diffraction plane.

x-ray diffractometer may be able to pick up the weak diffraction peak which is produced by the Ge-rich plates. On the other hand, due to the lattice misfit between the matrix and the Ge-rich zones, the position of the peak is very close to that of the main peak. In order to identify the weak peak corresponding to the Ge-rich regions, the optimum sample condition was found to be a large grained bulk sample. This produces a sharp diffraction peak of the matrix by confining the diffraction to occur only in one grain instead of many, which causes a diffused intensity profile. The sharp main peak reduces its overlap with the subpeak of (200) reflection of Ni_3Ge phase. In addition, the intensity of the subpeak is also increased, thereby making it easier to detect the subpeak. It seems that the x-ray diffraction technique is more sensitive in detecting the Ge-rich zones than the TEM technique, since the asymmetry in intensity profile of the (200) reflection could be identified even in Ni-4.87at%Ge alloy. However, the contrast effects and the corresponding diffuse scattering effects could only be distinguished in the TEM when the Ge concentration was greater than 7.87at%Ge.

The results of the x-ray diffraction studies have also suggested that the type of Ge distribution changes with increase in Ge concentration. In dilute Ni-Ge solid solutions the existence of a linear relationship between lattice parameter and Ge concentration suggests that they are ideal solid solutions. Therefore, the Ge distribution in the nickel lattice is suggested to be random. However, in the concentrated solutions some of the Ge solute atoms appear to cluster and form partially ordered Ge-rich zones. When the Ge concentration reaches 14.56at%Ge, compositional fluctuations due to the early stages of spinodal decomposition have been suggested to occur even in the sample which is water quenched from the solution treatment temperature. The results of the study of dislocation distribution in Ni-Ge solid solutions after 2% deformation have demonstrated that the dislocation distribution is also strongly influenced by the amount of Ge addition, and seems

to bear a close relationship with the type of Ge distribution. In dilute Ni-Ge solutions, the dislocation distribution is very similar to that observed in pure nickel. It seems that it is the nickel lattice itself which determines the characteristics of the dislocation distribution, and the Ge solute atoms only impede the dislocation motion in the alloy. In the Ni-4.87at%Ge alloy, where the Ge-rich zones are first detected by the x-ray diffraction, the dislocation distribution was observed to start to change from a three dimensional network into a planar slip configuration. Later on, the number of Ge-rich zones was found to increase with Ge concentration and the planar slip dislocation distribution was observed to become the dominant microstructural feature of the alloy. In supersaturated solid solutions, i.e. in Ni-11.98at%Ge and Ni-14.56at%Ge alloys, some dislocations were observed to be in a multipole configuration, which also exhibited a planar slip character and became increasingly well-developed with an increase in Ge concentration. Therefore, the formation of partially ordered Ge-rich zones seems to be responsible for promoting the formation of a planar dislocation distribution. This suggests that the prediction of Kanthaler et al [72,80] is also valid for Ni-Ge alloys.

5.1.2 Nature of Ge Distribution in the Ge-rich Zones

To investigate the nature of the distribution of Ge in the Ge-rich regions, the value of partial molar volume of Ge in concentrated Ni-Ge solutions was studied. The partial molar volume, $\overline{V_{Ge}}$, of Ge in the solid solutions can be expressed by

$$\overline{V_{Ge}} = V_{X_{Ge}} + (1-X_{Ge}) \left(\frac{\partial V_{X_{Ge}}}{\partial X_{Ge}}\right) \tag{94}$$

where, $V_{X_{Ge}}$ is the molar volume of the solution whose Ge mole fraction is X_{Ge}. The unit of the molar volume is cm^3/mol and the $V_{X_{Ge}}$ can be expressed by,

$$V_{X_{Ge}} = (a_{X_{Ge}})^3 \times \frac{6.02\times10^2}{4} \quad (95)$$

Where $a_{X_{Ge}}$ is the lattice parameter of the alloy with a Ge concentration of X_{Ge}. Since the variation in lattice parameter with composition is already known, the relationship between $V_{X_{Ge}}$ and the composition can be determined. The partial molar volume of Ge at each concentration, X_{Ge}, can be determined by drawing a tangent to the curve at the concentration point and finding the intercept of the tangent at the axis of X_{Ge}=1. The results are illustrated in Fig.88.The partial molar volume of germanium in dilute solutions, $\overline{V^{\circ}_{Ge}}$ is measured to be 8.1 cm^3/mol as illustrated in Fig.88. The values of the partial molar volume of germanium in the concentrated solutions show a significant negative deviation from that observed in the dilute solutions. For example, at point A, the value of partial molar volume of germanium, $V_{Ge\text{-}A}$, is measured to be 7.59 cm^3/mol which is 6.3% smaller than that of the $\overline{V^{\circ}_{Ge}}$ value. However, the value of partial molar volume of Ni in the concentrated solution is very close to that in the dilute solutions, $\overline{V^{\circ}_{Ni}}$. For example, at point A, the partial molar volume of nickel, $V_{Ni\text{-}A}$, almost coincides with $\overline{V^{\circ}_{Ni}}$. Therefore, in the concentrated solutions, it is only the partial molar volume of germanium that exhibits a significant deviation from the value of the dilute solutions. Moreover, using the same method, the partial molar volume of Ni and Ge in Ni_3Ge can be expressed by

$$V_{Ni_3Ge} = X_{Ge}\times\overline{V_{Ge}} + X_{Ni}\times\overline{V_{Ni}} \quad (96)$$

Since the amount of Ni in Ni_3Ge is relatively large, it is reasonable to assume that the value of partial molar volume of Ni in Ni_3Ge is still equal to that in the dilute solutions, i.e. $\overline{V_{Ni}} = \overline{V^{\circ}_{Ni}}$ = 6.59 cm^3/mol. Therefore, the value of $\overline{V_{Ge}}$ in Ni_3Ge can be expressed by,

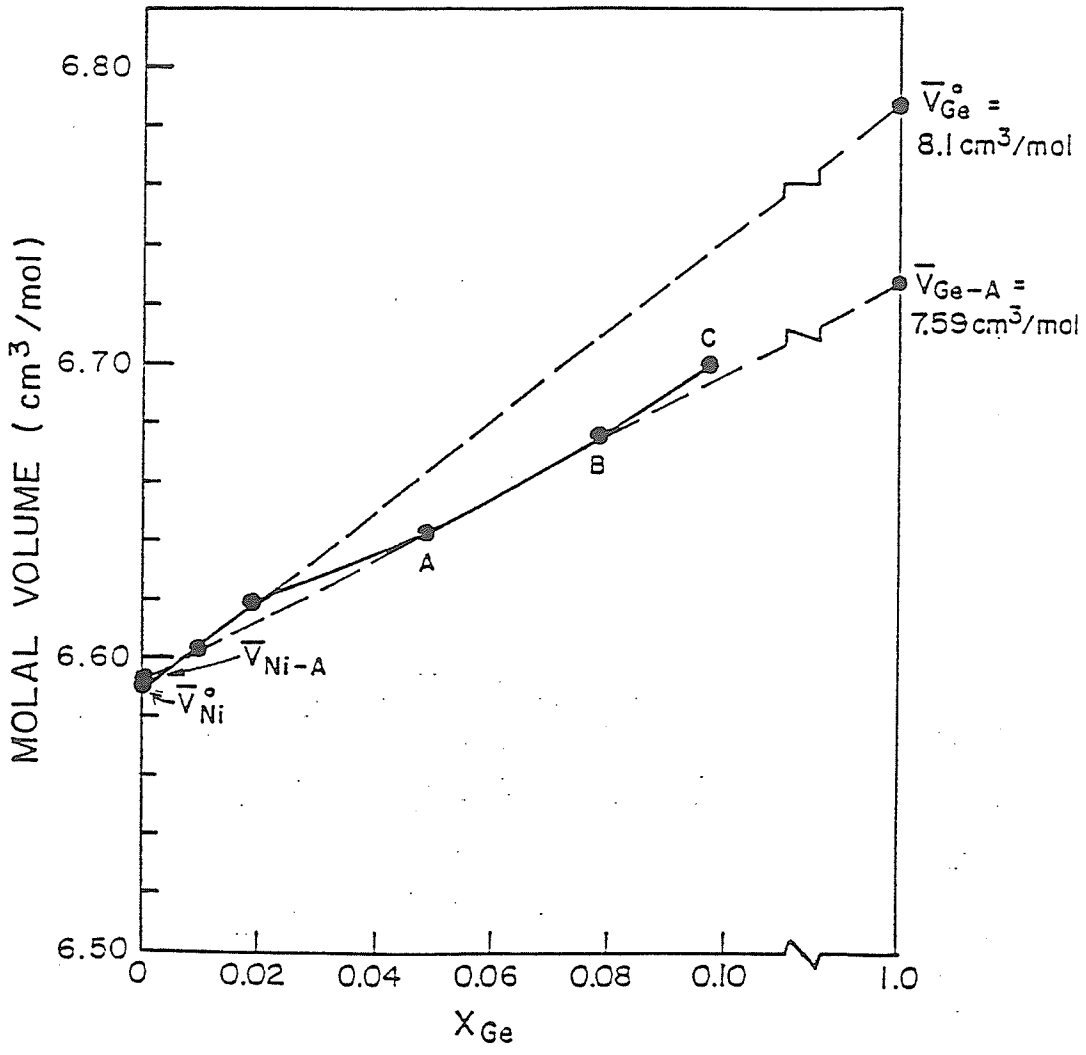

Fig.88 Variation in partial molal volume of Ge in dilute and concentrated Ni-Ge solid solutions, and in Ni_3Ge intermetallic compound.

$$\overline{V_{Ge}} = \frac{V_{Ni_3Ge} - X_{Ni}\,\overline{V^{\circ}_{Ni}}}{X_{Ge}} \qquad (97)$$

The molar fraction of nickel, X_{Ge}, in Ni-saturated Ni_3Ge is reported to be 0.225 [65], its lattice parameter is 0.3570 nm and hence its molar volume, V_{Ni_3Ge} , is calculated to be 6.85 cm^3/mol. By substituting these values in Eq.97, the value of partial molar volume of Ge in Ni_3Ge is calculated to be 7.75 cm^3/mol.. This value is very close to that of the partial molar volume of Ge in the concentrated solutions. This implies that the partial molar quantity of Ge in concentrated solutions is more similar to that in Ni_3Ge intermetallic compound than that in dilute solutions. The change in the thermodynamic property of Ge may be attributed to the stronger Ni-Ge interaction in the concentrated solutions.

The (200) interplanar spacing misfit, δ, between the lattice spacing of the matrix d_m and Ge-rich region d_L, is evaluated and shown in Table 11. The values of the interplanar misfit are found to be about 0.5% to 0.6% which are very small. Since the A.A.D. value of Ge in the dilute solutions is larger than the atomic diameter of Ni, where Ge solute atoms are randomly distributed in the Ni lattice, the expansion effect of a Ge addition is appreciable. If Ge solute atoms are still randomly distributed in the Ge-rich regions the misfit value could no longer be so small. Therefore, the Ge-rich regions should be somewhat locally ordered which implies a stronger interaction between nickel and germanium atoms, and leads to a reduction in specific volume of the alloy.

5.1.3 Consideration of Electron Theory

The formation of locally ordered Ge-rich regions can also be explained by the electron theory of phase stability. Ni is a transition metal with an e/a ratio of 10. Ge is an

element in the B subgroup of the Periodic Table and its e/a ratio is 4. A survey of A_3B type intermetallic compounds suggests that the stability of these compounds is mainly controlled by the ratio of total electrons outside the inert shell to the number of atoms in the unit cell [93]. Since the e/a ratio of Ni_3Ge is 8.5, the presence of germanium with a lower value of e/a ratio in the Ge-rich regions will reduce their e/a ratio, which will cause the Ni lattice to become unstable, and will promote the formation of Ni_3Ge. Since the composition in the Ge-rich regions has not yet reached the critical value which enables Ni_3Ge to precipitate, long range order in these regions is not likely to occur. Instead, a partial ordering may take place in these regions. The degree of localized ordering is suggested to be function of germanium concentration in the Ge-rich regions that causes the size of the unit cell to decrease continuously. This explains why the misfit between the Ge-rich zones and the matrix remains constant in the concentrated solutions.

5.1.4 Relationship Between the Localized Ordering and Planar Type Dislocation Distribution

It is known that Ni, Cu and their dilute solid solutions exhibit wavy slip at low and medium amount of deformation and the dislocation configuration in these materials exhibits a three dimensional character [94-97]. It is generally believed that an extensive cross-slip of screw dislocations enables them to tangle with each other [72,98-101] and hence give rise to a wavy dislocation distribution. It has been also recognized that the formation of short range ordering in Ni-Fe [102,103], Ni-Cr [93,104], Cu-Mn [105-107] and Cu-Al [108,109] alloys changes the dislocation distribution from an initially three dimensional configuration into a planar slip type configuration. Therefore, it is interesting to note that a similar close relationship exists between the formation of partially ordered

Ge-rich zones and the occurrence of the planar slip type dislocation configuration in the Ni-Ge alloy system. The presence of partially ordered Ge-rich zones seems to prevent extensive cross-slip of screw dislocations and restricts the dislocations to move on the limited slip planes. A possible mechanism leading to the formation of these dislocation configurations and their relationship to the Ge-rich zones revealed by the TEM studies is proposed next.

It is known that a completely ordered region is an effective obstacle to dislocation motion, and a pair of dislocations glide together when they cut through these ordered regions. Passage of the first dislocation of the dislocation pair destroys ordering in the region whereas the second dislocation restores it. The Ge-rich plates in Ni-Ge solid solutions were observed to be about 2~3 nm thick along the <100> direction. Therefore, when leading dislocations cut through the Ge-rich plates on (111) planes that lie along the thin direction, they destroy the ordering relationship between the upper and lower layer of the Ge-rich plate which is adjacent to the slip plane. The following dislocations then experience much lower resistance to their motion on the same slip plane and therefore, find an easier path to glide, and accordingly, the cross-slip motion of these dislocations becomes unnecessary. When the first leading dislocation meets with another thin Ge-rich plate, it becomes immobile and all the dislocations which follow are piled up against it. This pile-up exerts a force pushing against the leading dislocation that enables it to overcome the obstacle in front of it. Therefore, these partially ordered Ge-rich zones are suggested to be effective in providing resistance to only the first several leading dislocations. After these zones are cut through and become completely disordered, they are no longer effective obstacles to the dislocation motion. These cut Ge-rich areas are suggested to be soft and the material deforms heterogeneously.

5.1.5 Explanation for the Unusual Behaviour of the Variation in Lattice Parameter with Ge Concentration

The unusual variations in lattice parameter of Ni-rich Ni-Ge solid solutions with Ge concentration can be explained as follows. In dilute solid solutions, if the Goldschmidt's correction factor is considered, the Vegard Law is satisfied. In these solid solutions the variation of lattice parameter,a, with Ge concentration, X_{Ge}, is linear and can be expressed by $a = \sqrt{2} \cdot (X_{Ge}. A.A.D._{Ge} + X_{Ni}d_{Ni})$. The solid solutions can be treated as ideal solid solutions and Ge solute atoms are considered to be randomly distributed in the nickel lattice. The expansion effect of Ge is mainly due to its size effect. Since nickel atoms can effectively prevent contact between Ge atoms, the contribution of individual Ge solute atoms in expanding the nickel lattice is additive and the variation in lattice parameter with composition is linear. However, in solutions containing more than 2at% Ge, the distribution of Ge may be of two types. (1) A part of the solute atoms may distribute themselves randomly in the nickel lattice. This portion of the solute atoms contribute most to expand the lattice and the lattice parameter increases with Ge concentration. (2) another portion of the solute atoms seems to cluster in certain regions forming partially ordered Ge-rich regions. Since the specific volume of Ge-rich regions is smaller due to a stronger interaction between nickel and germanium atoms, their contribution to expand the lattice is less than that of the randomly distributed solute atoms. As a result, the net lattice parameter of the solid solution is smaller than that predicted by the Vegard law. As the number and the Ge content of the Ge-rich regions increases with Ge concentration, the effective amount of the Ge solute atoms randomly distributed in the matrix does not significantly increase with the composition, and the overall lattice parameter is observed to increase with Ge concentration at a decreasing rate.

5.2 Continuous Phase Transformation in Ni-14.56 at%Ge Alloy

During the x-ray diffraction study of the early stages of decomposition in Ni-14.56at%Ge alloy, the intensity of the sidebands was observed to be asymmetrical, i.e. the intensity of the sideband on the lower angle side of the (200) reflection was detected to be stronger than the one on the higher angle side. In the following sections, this asymmetry in intensity of sidebands is first discussed. Subsequently, the behaviour of Ni_3Ge precipitation in the alloy aged at 550°C and 600°C is discussed and a possible reaction path for the phase transformation is proposed.

5.2.1 Study of Asymmetry in Intensity Profile of the Sidebands Around the (200) Diffraction Peaks

As noted in section 4, the occurrance of sidebands reflects the fact that there exists a periodic modulation in composition in the alloy. Daniel and Lipson [13,14] assumed that the fluctuation in composition varies sinusoidally with a wavelength of λ. If the atomic sizes of solvent atom A and solute atom B are considerably different, the fluctuation in composition will induce a corresponding fluctuation in interplanar spacings. Similarly, if the atomic scattering factors of A and B atoms show a significant difference, the compositional fluctuation will also bring about a periodic variation in the atomic scattering factor. The intensity of an x-ray diffraction beam is a function of both the position of every individual atoms in the lattice as well as their atomic scattering abilities. Therefore, a periodic fluctuation in these two parameters will introduce a second order diffraction effect, i.e. the side band phenomenon. In the original approach of Daniel and Lipson (the D-L

model), the contribution of these two parameters to the intensity profile of sidebands was calculated separately. Therefore, theoretically, the intensity profiles of sidebands were suggested to be symmetrical. However, in the present study,when the Ni-14.56 at % Ge alloy was aged the intensity of the sidebands at each stage of ageing was observed to be stronger on the lower angle side of the (200) x-ray diffraction peak. In other words, there exists an asymmetry in the intensity profile of the sidebands around the main diffraction peak.

In Ni-Ge solid solutions, the apparent atomic size of Ge atoms is larger than that of Ni atoms. Also the wavelength of Cu-K_α radiation (0.15418 nm) is very close to the K absorption edge (λ_K) of nickel ($\lambda / \lambda_K = 1.04$). Therefore,when Cu-K_α radiation is used for the x-ray diffraction studies the value of the atomic scattering factor of Ni drops significantly. However, in the case of Ge atoms, the use of Cu-K_α radiation has little influence on their scattering ability. Thus, the atomic scattering factor difference between Ni (24.55 after correction) and (Ge, 30.23, after correction) is not negligible. Since both of these two parameters are significantly different for Ni and Ge atoms, it seems appropriate to consider them conjunctively when the intensity of the diffraction peak is determined. Therefore, the D-L model is reconsidered as follows.

According to the D-L model, the periodic fluctuation in Ge concentration, X_{Ge} , within the Ni-Ge solid solutions, can be expressed as follows

$$X_{Ge} = X_{Ge,av} + k \cos (2\pi\, qd / Qa) \qquad (98)$$

where $X_{Ge,av}$ is the average composition of the alloy, k and Q are the amplitude

and wavelength of the composition fluctuation wave respectively, and q denotes the qth reflection plane from the origin, d is the average interplanar spacing of the lattice along the direction x. As treated in the D-L model, the position of the qth plane from the origin will be given by

$$X(q) = qa + (AQ/2\pi)\sin(2\pi q/Q) \tag{99}$$

where, A is a parameter reflecting the amplitude of displacement of each reflecting plane. Similarly, the variation in atomic scattering factor is given by

$$f(q) = f_0 + D\cos(2\pi q/Q) \tag{100}$$

where f_0 is the average atomic scattering factor and D is the amplitude of the variation in atomic scattering factor. Then, the relative amplitude of the **g** order diffraction is given by

$$F=\sum_{q=0}^{Q-1} [f_0 + D\cos(2\pi\, q/D)] \exp\{2\pi\, ig[qd+(AQ/2)\sin(2\pi\, q/Q)]/d\} \tag{101}$$

Since the assumption and calculation procedures are similar to those of D-L treatment, only the results are given here:

$$F = \sum_{q=0}^{Q-1} f_0 \exp(2\pi\, igq) + 1/2 \sum_{q=0}^{Q-1} [D+ (gAQf_0)/d] \exp[2\pi\, iq\,(g+1/Q)] + \\ + 1/2 \sum_{q=0}^{Q-1} [D - (gAQf_{0)}/d] \exp[2\pi\, iq\,(g-1/Q)] \tag{102}$$

Obviously, values of the relative amplitudes of the diffraction beams (F) are large only when g = h, h+1/Q, h - 1/Q, where h is an integer. The first term in Eq.102 is the

relative diffraction amplitude of the average lattice and contributes to the intensity of the main diffraction peak. The second and third terms are the relative amplitudes of the lower and higher angle side bands, respectively. If the intensity of the diffracted beam from the average lattice is denoted as I(h) and is assumed to be unity, the relative intensity of the lower angle side band will be given by,

$$I\,(h\text{-}1/Q) = 1/4\,[D + gAQf_0 / a]^2 = 1/4\,[D^2 + (qAQf_0 / a)^2 + 2DgAQf_0 / a\,] \qquad (103)$$

and the intensity of the higher angle side band will be given by,

$$I\,(h\text{+}1/Q) = 1/4\,[D - gAQf_0 / a]^2 = 1/4\,[D^2 + (gAQf_0 / a)^2 - 2DgAQf_0 / a\,] \qquad (104)$$

A comparison of Eqs.103 and 104 shows that the intensity of the lower angle side band, i.e. I(h-1/Q) has a higher value. The difference in the intensity of the two side bands is given by,

$$I\,(h - 1/Q) - I\,(h + 1/q) = DgAQf_0 / a \qquad (105)$$

which is proportional to the product of the amplitude of the variation of interplanar spacing (A) and the variation in the atomic scattering factor (D). Therefore, the results suggest that a significant asymmetry in intensity of the side band will be observed only in those alloys in which both interplanar spacing and atomic scattering factor show an appreciable difference.

The above argument is supported by further experimental results. Upon aging for 15 and 40 minutes (Fig.70a,b), the intensity of the side band on the lower angle side of the diffraction peak is always observed to be stronger than the one on the higher angle side.

The following general picture of fluctuation in composition in Ni-Ge solid solutions is now becomes clearer. The initial stage of transformation actually involves a phase separation, in other words, clustering of solute atoms. This phase separation is established via a periodic fluctuation in composition which progressively forms Ge-rich and Ge-depleted regions. The Ge-rich regions have a larger interplanar spacing, and diffraction from those regions occurs at lower values of 2θ in accordance with the Bragg diffraction law. Therefore, diffraction from these regions contributes more to the intensity of the lower angle side band. At the same time, the average atomic scattering factor of the Ge-rich regions is higher, the diffraction effect is stronger, and the intensity of the lower angle side band should be higher, as has been observed. This phase separation leads to the ordering reaction and the transformation of equlibrium Ni_3Ge phase in those Ge-rich regions in which the Ge concentration reaches a critical level. As the Ge concentration in Ni_3Ge is about 23.5 at%, which is higher than the average concentration of germanium in the matrix, the (200) reflection of Ni_3Ge is also on the lower angle side of the (200) matrix peak.

If the profile of the (200) peak in the as-quenched specimen is studied further, it is observed that the intensity on the lower angle side of the (200) diffraction peak is diffuse. This implies that the fluctuation in composition has somehow started during quenching from the solid solution treatment temperature. Since the amplitude of composition fluctuation is small during the very early stages of decomposition, the intensity of side band is very weak and can hardly be detected. As intensity of the side band on the higher angle side of the (200) peak is even lower it can not be distinguished from the background.

In addition, from Eqs.103 and 104 the amplitude of fluctuation in atomic scattering factor, D, can be determined by the following expression

$$D = I_L^{1/2} + I_H^{1/2} \tag{106}$$

In the Ge-rich region,

$$D = f_{max} - f_0 \tag{107}$$

where, f_{max} is the maximum value of atomic scattering factor.

Assuming that f is a linear function of composition, i.e. $f = X_{Ge}\, f_{Ge} + (1-X_{Ge})\, f_{Ni}$, and substituting it into Eq.106, D can be expressed by,

$$\begin{aligned} D = I_L^{1/2} + I_H^{1/2} &= f_{max} - f_0 \\ &= X_{Ge,0}\,(X_{Ge,max} - X_{Ge\,0})\,(f_{Ge} - f_{Ni}) \end{aligned} \tag{108}$$

where, $X_{Ge,0}$ is the average composition of the Ge-enriched region of the solid solution and $X_{Ge,max}$ is the composition corresponding to the highest Ge concentration in the region. Then, $X_{Ge,max}$ can be expressed by,

$$X_{Ge,max} = X_{Ge,0} + (I_L^{1/2} + I_H^{1/2}) / (f_{Ge} - f_{Ni}) \tag{109}$$

Due to the cosine nature of the composition wave, the average composition in the Ge-rich region is 0.64 $X_{Ge,max}$. For a similar reason, the lowest concentration $X_{Ge,min}$ in the Ge-depleted region can be expressed by

$$X_{Ge,min} = X_{Ge\,0} - (I_L^{1/2} + I_H^{1/2}) / (f_{Ge} - f_{Ni}) \tag{110}$$

The average composition in the Ge-depleted region can therefore be obtained from $0.36\ X_{Ge,0} + X_{Ge,min}$.

The relative peak intensities of the two sidebands around the (200) diffraction peak in Ni-14.56at%Ge alloy, shown in Fig. 69b, are 0.19 and 0.05, respectively. Accordingly, the average concentration of Ge in Ge-rich region is estimated to be about 22at% and in the Ge-depleted region about 7 at%Ge. However, the maximum concentration of Ge in the Ge-enriched region, is found to be 26at%. This implies that the Ge concentration has reached a level at which Ni_3Ge can precipitate. The presence of a small (200) peak of Ni_3Ge, which is barely visible in Fig.69b, seems to be consistent with this analysis. The Ge content of new precipitate is found to be a little bit higher than the equilibrium concentration of Ge in Ni_3Ge.

5.2.2. Continuous Phase Transformation of Ni_3Ge-γ' in NI-14.56 at%Ge Alloy During Isothermal Ageing at 550 and 600 °C

According to the Ni-Ge phase diagram, which is illustrated in Fig.18, when the Ni-14.56 at%Ge alloy is solution heat treated at 1100°C, fast quenched to room temperature and aged at 550°C and 600°C, the microstructure of the alloy shoul be composed of two equilibrium phases, viz disordered Ni-α solid solution and ordered Ni_3Ge-γ' intermetallic compound. In the quench-aged specimen, the Ge concentration in Ni-saturated Ni_3Ge should be about 23 at% and the equilibrium volume fraction of Ni_3Ge-γ' phase should be about 30%. The formation of Ni_3Ge-γ' phase from an originally disordered Ni-α supersaturated solid solution during the ageing treatment should involve two basic

processes. First, Ge solute atoms should cluster somewhere within the alloy in order to satisfy the composition requirement for the formation of Ni_3Ge-γ' precipitates. Secondly, Ni and Ge atoms should arrange themselves in the Ge-clustered regions to form an ordered $L1_2$ crystal structure. The results of this investigation suggest that when Ni-14.56at%Ge alloy is isothermally aged at 550°C and 600°C, both of these two processes occur in a continuous manner. In the following section, this behaviour is discussed first, followed by a proposed possible reaction path involving the interplay of these two processes.

A. Spinodal decomposition during early stages of the transformation

According to the experimental results, the microstructural development of the alloy during isothermal ageing can be subdivided into the sequences presented below.

In the as-quenched condition, fluctuation in composition within the material has already occurred. The mottled contrast observed in the TEM micrograph of the as-quenched samples, as well as the intensity fluctuation on the lower angle side of the (200) x-ray diffraction peak are all evidence for the existence of this composition fluctuation. However, at this stage, since the contrast and the diffuse scattering effects are not very pronounced, the amplitude of the composition fluctuation within the as-quenched material is relatively small. As mentioned in the literature review in chapter 2, the amplitude of the initial composition fluctuation is probably due to (1) thermal fluctuation which may already exist within the material when it is solution heat treated at high temperature [21], and/or (2) a certain degree of decomposition within the material during quenching from the solution treatment temperature.

On ageing at 550 and 600 °C., the sidebands become better defined and appear on

both sides of the (200) reflection. Since the intensity of the sidebands depends on the amplitude of the composition fluctuation, a continuous increase in intensity of the sidebands with ageing time indicates that the growth of the amplitude of the composition fluctuation is time dependent. Furthermore, since the position of the sidebands was observed to move towards the main diffraction peak progressively with ageing time, the wavelength of the composition fluctuation, which is inversely proportional to the angular deviation of the sideband from the main peak, is also time dependent. The microstructural features of the aged material also exhibit a progressive change. With increase in ageing time, a better defined modulated microstructure arranged along the <100> matrix direction also appeared. The wavelength of the modulated structure was observed to increase continuously with ageing time. Therefore, during the early stages of the phase transformation, both the amplitude and the wavelength of the composition modulation demonstrate a continuous and progressive increase. In addition, it appears that the composition fluctuation occurs in advance of the formation of Ni_3Ge-γ' precipitates. Evidence of this can be obtained by comparing the intensity profile of (200) and (100) peaks in the alloy aged at 600°C. In Figs.79a and 83a it is seen that in the as-quenched condition the intensity fluctuation contributed by the composition fluctuation has already occurred. However, no (100) superlattice peak of Ni_3Ge-γ'phase has been detected. This indicates that Ni_3Ge-γ' has not yet precipitated at this stage. After 5 minutes of ageing, the (200) reflection of Ni_3Ge-γ' is barely visible on the shoulder of the low angle sideband. (Fig.79b). Correspondingly, a relatively weak and diffuse (100) superlattice peak starts to appear. The same conclusion can be drawn by examining the curve illustrated in Fig.85 which demonstrates the relative volume fraction of Ni_3Ge-γ' precipitates after a given length of time with respect to the total equilibrium volume of Ni_3Ge-γ' phase, when alloy is aged at 600°C. By extrapolating the curve to the horizontal axis, the start of the precipitation of Ni_3Ge-γ' is estimated to be at about 5 minutes of ageing. This is consistent

with the conclusion based on the x-ray diffraction study (Fig.79). This will become even more evident when evolution of the intensity profile of (200) peak in the alloy aged at 550°C is examined. Since the diffusion rate is lower at this lower ageing temperature, it takes a longer time for the composition fluctuation to be sufficiently well developed to promote the Ni_3Ge-γ' precipitation. Therefore, at this ageing temperature it takes about 25 minutes of ageing for a relatively small (200) peak of Ni_3Ge-γ' to become visible. However, before that, the amplitude of the composition fluctuation wave exhibits a continuous increase. Therefore, it is concluded that when the alloy is aged at 550°C and 600°C, a composition fluctuation occurs first to give rise to the Ge-rich and Ge-depleted regions. When the Ge concentration in the Ge-rich regions reaches a critical point, the Ni_3Ge-γ' precipitates start to form. In other words, the composition requirement for the Ni_3Ge-γ' precipitation is accomplished via a continuous composition fluctuation process.

It was observed that when the material was aged at 550°C, the wavelength of composition fluctuation was time independent during the very early stages. In addition, at the ageing temperature of 600°C the growth of the composition fluctuation wavelength follows the Lifschitz-Slyozov and Wagner theory of diffusion controlled growth. These two kinetic characteristics of the aged alloy are similar to those of the most common spinodal alloys and are considered to be the two most important criteria for distinguishing spinodal decomposition from the conventional nucleation and growth transformation. Moreover, in Fig.77b which is the central dark field micrograph of a specimen aged at 600°C for 15 minutes, it is seen that the Ni_3Ge-γ' precipitates are periodically distributed within the matrix.This periodic distribution is caused by the composition fluctuation which creates the periodic alignment of the Ge-rich and Ge-depleted regions and promotes the formation of Ni_3Ge-γ' precipitates in these Ge-rich regions. Since no preferential nucleation sites for Ni_3Ge-γ' precipitates like grain boundaries or dislocations could be

observed, the precipitation behaviour is suggested to exhibit a homogeneous character. This behaviour is also believed to be an important microstructural characteristics of spinodal decomposition.

The microhardness of the aged alloy increased significantly during the very early stages of the phase transformation. Since at this stage, Ni_3Ge-γ' can not precipitate due to the unavailability of suitable Ge-enriched sites, the increase in hardness can only be attributed to the composition fluctuation. This situation is more clearly demonstrated in Fig.86, which illustrates the variation in hardness with ageing time when the alloy was aged at 550°C. Although there exists a well defined period before Ni_3Ge-γ' starts to precipitate, which has been confirmed by the x-ray study, the hardness of the material exhibits a progressive increase from the very beginning of the ageing process. This indicates that incubation period for the increase in hardness does not exist. However, in a precipitation process via conventional nucleation and growth mechanism, the change in the most microstructural sensitive parameters of the material, like hardness, magnetism etc, should exhibit an incubation period. Therefore, based on the observation of changes in microhardness with aging time, the material seems to undergo a spinodal decomposition during the early stages of phase transformation.

Based on the experimental evidence which includes the kinetic behaviour of the decomposition process, the occurrence of modulated microstructure and satellite effects in the diffraction pattern as well as the variation of microhardness with ageing time, it is concluded that during the early stages of transformation, spinodal decomposition occurs in the Ni-14.56at%Ge alloy. The fluctuation in composition results in the establishment of periodically aligned Ge-rich and Ge-depleted regions. When the composition in the Ge-rich regions reach the appropriate value, equilibrium Ni_3Ge-γ' phase starts to precipitate from

these regions.

B. Interplay of clustering and ordering during the phase transformation

According to the variation in the lattice parameter with composition, it is seen that in the two phase field the rate of increase in lattice parameter with Ge concentration is appreciable. Therefore, the fluctuation in composition, which gives rise to the formation of Ge-rich regions, might induce considerable strain and hence a corresponding strain energy in the lattice. This extra amount of energy with a positive value might decrease the driving force for spinodal decomposition and have a tendency to stabilize the solid solution. However, if an ordering process occurs simultaneously, Ni and Ge atoms might be adjusted locally to some appropriate lattice sites, and the internal energy as well as the strain energy may be effectively reduced. This situation is expected to be more energetically favorable for further phase separation. In the literature review, the cooperation of clustering and ordering has been suggested to be theoretically possible. On the basis of the electron theory of phase stability also, this type of cooperation seems to be a reasonable suggestion. As analyzed previously, since the e/a ratio of Ni is 10 and that of Ge is 4, when 3 Ni atoms and 1 Ge atom bond together to form a Ni_3Ge unit cell its e/a ratio is 8.5. A continuous addition of Ge to the Ni-Ge solution could cause the Ni lattice to become unstable and promote the Ni_3Ge phase to precipitate. Therefore, an increase in Ge concentration is likely to increase the concentration of Ge in Ge-enriched regions which would promote a certain degree of short range ordering progressively in Ge-rich regions. This would relax the internal energy as well as the strain energy in the lattice and may compensate for the increase in energy caused by the fluctuation in composition. In this manner, the clustering and ordering become a mutually cooperative processes.

In accordance with the technique proposed by Laughlin and Soffa [2] a mechanism of phase transformation involving cooperation of clustering and ordering can be justified by using the free energy vs composition diagram which is shown in Fig.89. The average composition of the alloy is c_0 and the free energy curve of the disordered solid solution shows two inflections s_1 and s_2. Since the free energy of the system is a function of composition and the state of ordering in a solid solution, a series of free energy curves ranging from short range ordering (SRO) to imperfect long range ordering (ILO) between the disordered and the lowest ordered curves can be developed. Since the disordered solid solution with composition C_0 is energetically unstable with respect to the formation of Ge-enriched and Ge-depleted regions, spinodal decomposition occurs. On the other hand, since the SRO state is energetically more favorable with respect to the totally disordered state, the original disordered region with higher Ge concentration (i.e. expressed as $C_{r'}$) becomes somewhat ordered ($C_{r''}$). In this way, continuous phase separation and ordering proceed simultaneously and cooperatively and finally produce a mixture of equilibrium Ni-α phase with composition c_1 and an ordered Ni_3Ge phase. Therefore, the real reaction path in the Ge-rich regions, which is described by using the change in the free energy of the system, is likely to exhibit a "staircase profile" as shown in Fig.89.

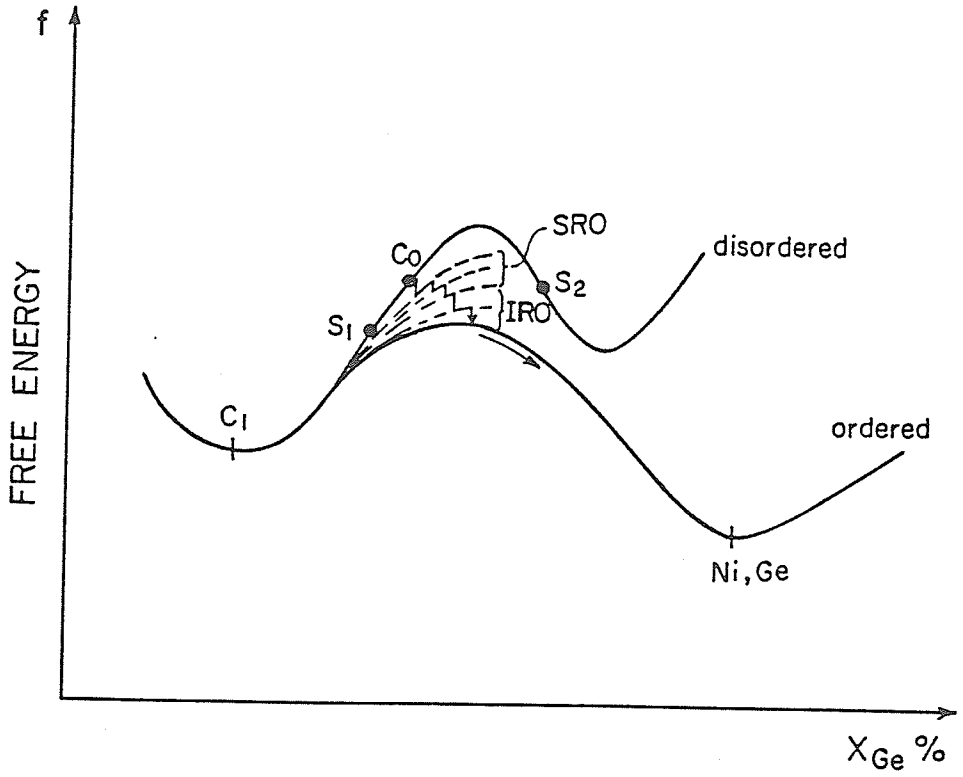

Fig.89 Schematic free energy vs composition curve illustrating the possible reaction path with a "staircase profile" in Ni-14.56at%Ge alloy aged at 550°C and 600°C .

Chapter 6

Conclusions

1. The results of the precise lattice parameter measurement of Ni-Ge solid solutions with Ge concentrations up to 15at% are in excellent agreement with those obtained by Brahman, Jena and Chaturvedi [60]. According to the nature of the lattice parameter vs. composition curve, the curve can be divided into three regions. In the first composition region with a Ge concentration from zero to about 2at%, the relationship between the lattice parameter and Ge concentration is observed to be linear. In the second region with Ge concentration from 2 at% to about 10 at%, the curve exhibits a significantly negative deviation from the linear plot extrapolated from the first region. The degree of negative deviation increases with an increase in the Ge concentration of the solid solutions. In the third region, the solid solutions are supersaturated and the lattice parameter increases with an increase in Ge concentration and the curve moves towards the linear plot again.

2. In the first region, i.e. a dilute solid solution region, the apparent atomic diameter of Ge solute is 0.272 nm which is 11% larger than the atomic diameter of Ge in its diamond crystal structure. This increased value is found to be consistent with that obtained by using Goldschmidt's correction factor which is based on the coordination number. Thermodynamically, the dilute solid solutions are suggested to be ideal and the distribution of Ge atoms in Ni lattice is random. Therefore, the lattice parameter of the solid solutions

exhibits a linear relationship with Ge concentration.

3. In the second region, i.e. in a concentrated solid solution region, small plate-like Ge-rich zones are found to be present by using both x-ray and TEM techniques. The number as well as the Ge concentration in these plate-like zones increases with Ge concentration. The crystallographic relationship between Ge-rich zones (G) and the matrix (M) is suggested to be $(100)_G \parallel (100)_M$ and $[010]_G \parallel [010]_M$. Based on the comparison of partial molar volumes of Ge in Ni-Ge solid solutions with different Ge concentration and in Ni_3Ge intermetallic compound, as well as on the basis of the influence of e/a ratio on stability of fcc crystal structure, the Ge-rich zones are suggested to be partially ordered and possess a lower specific volume. The presence of Ge-rich zones with a lower specific volume is suggested to cause the negative deviation in the lattice parameter vs. composition curve from the extrapolated linear plot.

4. The addition of Ge in the Ni lattice significantly influences the dislocation configuration in the material 2% deformed. In dilute solid solutions, like in pure nickel, the dislocation substructure has in a three-dimensional morphology. This kind of dislocation configuration implies that the dislocations can climb easily and hence tangle with each other. In the concentrated solutions, the dislocation configuration is planar. The presence of partially ordered Ge-rich zones is suggested to be responsible for the formation of this kind of dislocation substructure.

5. Based on the microstructural characteristics, results of the kinetic study of the phase transformation, and the nature of the variation in microhardness with ageing time, it is concluded that Ni-14.56at%Ge alloy in the as-quenched condition, and during the isothermal ageing that follows at 550°C and 600°C undergoes a spinodal type phase

separation in advance of Ni_3Ge precipitation. The continuous composition modulation due to spinodal decomposition gives rise to a periodic alignment of Ge-rich and Ge-depleted regions. When the Ge concentration in the Ge-rich regions reaches a critical value, Ni_3Ge-γ' phase starts to precipitate. The strengthening effect due to this kind of continuous phase transformation to produce Ni_3Ge is very appreciable.

6. Based on the modern continuous phase transformation theory and consideration of the influence of e/a ratio on the stability of fcc crystal structure by the Ge additions, a "staircase profile" reaction path involving the cooperation of clustering and ordering reactions has been suggested and expressed by using a graphical thermodynamic approach.

REFERENCES

[1] J.W. Christian, in "The Theory of Transformations in Metals and Alloys", Pergamon Press, Oxford, 1973.

[2] W.A. Soffa and D.E. Laughlin, In "Proc. Int. Conf. on Solid → Solid Phase Transformations, edited by H.I. Aaronson et al, Warrendale, Pa, 1982, p.159.

[3] A.J. Bradley, Proc. Phys. Soc. Lond. 52, 1940, p.80.

[4] A.J. Bradley, W.F. Cox and H.J. Goldschmidt, J. Inst. Met. 67, 1941, p.189.

[5] V. Daniel and H. Lipson, Proc. Roy. Soc. London, A181, 1943, p.368.

[6] V. Daniel and H. Lipson, ibid, A182, 1944, p.378.

[7] M.J. Saarivirta and H.S. Cannon, Met. Prog. 76, 1959, p.81.

[8] M. Hillert, D. Sc. Thesis, Massachusetts Institute of Technology, 1956.

[9] M. Hillert, Acta Met. 9, 1961, p.525.

[10] J.W. Cahn, ibid, 9, 1961, p.795.

[11] J.W. Cahn, ibid, 10, 1962, p.179.

[12] J.T. Plewe, Met. Trans. A6A, 1975, p.537.

[13] J.W. Cahn, Trans. AIME 242, 1968, p.166.

[14] J.E. Hilliard, in Phase Transformations ASM, 1968, p.497.

[15] J.E. Morral and J.W. Cahn, Acta Metall. 19, (1971) 1037.

[16] J.E. Morral, ibid, 20, 1972, p.p.1061-1069.

[17] D. de Fontaine, J.Phys. Chem. Solids 33, (1972) 297.

[18] D. de Fontaine, Acta Met. 23, 1975, p.553.

[19] L.E. Tanner and D.E. Laughlin, Scr. Met. 9, 1975, p.373.

[20] W.A. Soffa and D.E. Laughlin, Acta Met. Vol.37, No.11, 1989, p.3091.

[21] J.W. Edington, in Practical Electron Microscopy in Materials Science, The Macmillan Press Ltd, London, Vol.3, Appendix 3, 1975.

[22] E.L. Huston, J.W. Cahn and J.E. Hilliard, Acta Met. 14, 1966, p.1053.

[23] A.J. Ardell and R.B. Nicholson, Acta Met. 14, 1966, p.1295.

[24] R. Wagner, Czech J. Phys. B81, 1980, p.198.

[25] D.E. Laughlin and J.W. Cahn, Acta Met. 23, 1975, p.329.

[26] R.J. Livak and G. Thomas, ibid, 19, 1971, p.497.

[27]. T. Miyazaki, S. Takagishi, H. Mori and T. Kozakari, ibid, 28, 1980.

[28] H. Kreye and P. Pech, Z. Metallk., 64, 1973, p.765.

[29] C.K. Wu and G. Thomas, Met. Trans. 8A, 1977, p.1911.

[30] A. Chou, A. Datta, G. H. Thomas and W.A. Soffa, J. Met. Sci. 13, 1978, p.541.

[31] C.K. Wu, R. Sinclair and G. Thomas, Met. Trans. 9A, 1978, p.381.

[32] R. Sinclair, R. Gronsky and G. Thomas, Acta Met. 24, 1976, p.789.

[33] A.G. Khachaturyan, T.F. Lindsey and J.W. Morris, Met. Trans. 19A, 1988, p.249.

[34] H.E. Cook and D. de Fontaine, J.E. Hilliard, Acta Metall. 17, 1969, p.765.

[35] H.E. Cook and D. de Fontaine, ibid, 17, 1969, p.915 and 19, 1971, p.607.

[36] L. Chen and A.G. Khachaturyan, ibid, 39, No.11, 1991, p.2533.

[37] S. Allen and J.W. Cahn, ibid Vol.24, 1976, p.425.

[38] M.J. Wahll, D.J. Maykuth and H.J. Hucek, in "Handbook of Superalloys", Battelle Press. Columbus, 1979.

[39] R.W. Fawley, in "The Superalloys", edited by C.T. Sims and W.C. Hagel, Wiley, New York, 1972, p.3.

[40] A.K. Jena and M.C. Chaturvedi, J. Mater. Sci. 19, 1984, p.3125.

[41] C.Wagner, Z. Electrochem., 65, 1961, p.581.

[42] R.E. Smallman, in "Modern Physical Metallurgy", 4th edn. Butterworths, & Co Ltd, 1985, p.391.

[43] A. Nash and P. Nash, in " Binary Alloy Phase Diagrams", edited by T.B. Massalski et al, American Society for Metals, Metal Park, Ohio, Vol.2, 1986, p.1230.

[44] W.O. Gentry and M.E. Fine, Acta Met. 20, 1972, p.181.

[45] C.L. Corey, B.Z. Rosenblum and G.M. Green, Acta Met. 21, 1973, p.837.

[46] S.A. Hill and B. Ralph, ibid, 30, 1982, p.2219.

[47] D.H. Ben Israel and M.E. Fine, ibid, 11, 1963, p.1051.

[48] D.E. Laughlin, ibid, 24, 1976, p.53.

[49] K. Saito and R. Watanabe, Japan J. Phys. 8, 1969, p.14.

[50] H. Yoshida, M. Arita, A. Cemi and G. Kastorr, Acta Met. 34, 1986, p.1401.

[51] G. Kostorz, in "Danymics of Ordering Process in Condensed Materials", New York.

[52] R. Sinclair, J.A. Leake and R. Ralph, Phys Stat. Sol. 264, 1974, p.285.

[53] A. Dayer and P. Feschotte, J. Less Common Metals, 72, 1980, p.51.

[54] I.R. Brahman, A.K. Jena and M.C. Chaturvedi, Scr. Met. 23, 1989, p.1281.

[55]. A. Nash and P. Nash, in " Binary Alloy Phase Diagrams", edited by T.B. Massalski et al, American Society for Metals, Metal Park, Ohio, Vol.2, 1986, p.1231.

[56] D.W. Wee, O. Noguchi, Y.Oya and T. Suzuki, Trans. Jpn. Inst. Met. 21, 1980, p.237.

[57] H.W. King, in "Physical Metallurgy", edited by R.W.Cahn, North-Holland Pub. Co., 1965, p.60.

[58] W. Hume-Rothery, in "Elements of Structure Metallurgy", Institute of Metals, London, 1961, Monograph and Report Seris, No.26.

[59] H.W. King, D.F. Gibbons, in " Physical Metallurgy', edited by R.W. Cahn,

North-Holland Pub. Co. 1965, pp.33-69.

[60] A.K. Jena and M.C. Chaturvedi, Scr. Met. 23, 1989, p.1281.

[61] N.J. Grant and R.M.N. Pelloux, Trans. Met. Soc. AIME, 218, 1960, p.232.

[62] W.B. Pearson and L.T. Thomson, Can. J. Phys. 35, 1957, p.349.

[63] P. Lecocq, Ann Chem., (paris) 8, 1963, p.1397.

[64] W. Klement, Can. J. Phys. 40, 1962, p.1397.

[65] A.K. Jena and M.C. Chaturvedi, J. Mater. Res., 4, No.6, 1989, p.1417.

[66] S. Allen and J.W. Cahn, Acta Met. 24, 1976, p.425.

[67] A. Datta and W.A. Soffa, ibid, 24, 1976, p.987.

[68] D.E. Laughlin, ibid, 24, 1976, p.53.

[69] H. Ino, ibid, 26, 1978, p.827.

[70] T.B. Massalski, in "Physical Metallurgy", edited by R.W. Cahn, North-Holland Pub. Co., 1965, p.172.

[71] Th. Steffens, Ch. Schwink, A. Korner and H.P. Karnthaler, Phil. Mag. A 56,

1987, p.161.

[72] V. Gerold and H.P. Karnthaler, Acta Met. 37, 1989, p.2177.

[73] W.B Pearson and L.T. Thomson, Can. J. Phys. 35, 1957, p.1281.

[74] JCPD 4-850, 1990.

[75] W. Klement Jr. Can. J. Phys. 40, 1962, p.1397.

[76] H.J. Axon and w. Hume-Rothery, Proc. Roy. Soc. A193, 1948, p.1.

[77] V.W. Goldschmidt, Z Phys. Chem. 133, 1928, p.397.

[78] W.B. Pearson, in A Handbook of Lattice Spacing and Structures of Metals and Alloys, Pergamon Press, London and New York, Vol.1, 1958.

[79] P. Hassen, in" Physical Metallurgy" Cambridge Univ. Press, Cambridge, 1986, p.334.

[80] H.P. Karnthaler and L. Fisher, Z. Metallk. 66, 1975, p.631.

[81] R. Gevers, A.Art and S. Amelinckx, in Proc. 3rd. European Conf. on Electron Microscopy, Prague, Vol.A, Czechoslovak Academy of Science, 1964, p.205.

[82] P. Humble, Phys. Stat Sol., 30, 1967, p.183.

[83] J. Van Landuyt, R. Gevers and S. Amelincks, Phys. Stat. Sol, 18, 1966, p.167.

[84] W. Bell, W.R. Roser and G. Thomas, Acta Metall. 12, 1964, p.1247.

[85] C.T. Forwood and P. Humble, Aust, J. Phys. 23, 1970, p.697.

[86] P. Hirsch et at. in "Electron Microscopy of Thin Crystals", Robert E. Krieger Pub. Co., New York, 1965, p.229.

[87] B. Ditchek, L.H. Schwartz, Acta Metall. 28, 1980, p.807.

[88] E.P. Bulter, G. Thomas, ibid, 18, 1970, p.347.

[89] D.E. Laughlin and J.W. Cahn, ibid, 23, 1975, p.329.

[90] T. Miyzaki, S. Takagishi, H. Mori and T. Kozakari, ibid, 28, 1980, p.1143.

[91] R.J. Livak and G. Thomas, ibid, 19, 1971, p.497.

[92] B.D. Cullity, Element of X-Ray Diffraction, Addison-Wesley, Reading, MA. USA 1959.

[93] W. Hume-Rothery, Progr. Mater. Sci., 13(5), 1967, p.229.

[94] H.P. Karnthaler and L. Fisher, Z. Metallk. 66, 1975, p.631.

[95] H. Muahrabi, Phil. Mag. 23, 1971, p.897.

[96] S. Mader, A Seeger and H.M. Thieringer, J. Appl. Phys. 34, 1963, p.3367.

[97] M.F. Collins and D.A. Wheeler, Proc. Phys. Soc. 82, 1963, p.633.

[98] S.I. Hong and Liard, Acta Metall., 38, 1990, p.1581.

[99] A. Howie, in Direction Observation of Imperfection in Crystals, edited by J.H. Newkirk and J.H. Wernick, Interscience, New York, 1960, p.283.

[100] S. Mader, in Electron Microscopy and Strength of Crystals, edited by G. Thomas and J. Washburn, Interscience, New York, 1963, p.183.

[101] P.R. Seann, ibid, p.131.

[102] H.P. Karnthaler and B. Schugerl, in Strength of Metals and Alloys, Pergamom Press, Oxford, 1979, p.205.

[103] A Heilmann and W. Zinn, Z. Metallk., 58, 1967, p.113.

[104] N. Clement, D. Caillard and J.L. Martin, Acta Metall., 32, 1984, p.961.

[105] Th. Steffens, Ch. Schwink, A. Korner and H.P. Karnthaler, Phil. Mag. A 56, 1987, p.161.

[106] J.R. Davis, S.K. Bueke and B.D. Rainford, J. Magn. Magn. Mater. 15, 1980, p.151.

[107] T.M. Harders, T.J. Hicks and J.H. Smith, J. Phys. F., 13, 1983, p.1263.

[108] J.E. Epperson, P.Furnrohr and C. Ortiz, Acta Crystallogr., A.34, 1978, p.667.

[109] H.P. Karnthaler, F. Pring and G. Haslinger, Acta Metall., 23, 1975, p.155.